

Universidade de Brasília – UnB
Instituto de Física - IF

Marco Antonio Rodriguez Martinez

**SYNTHESIS AND CHARACTERIZATION OF THE
STRUCTURAL, MICROSCOPIC AND MAGNETIC PROPERTIES
OF FeNi NANOPARTICLES SYNTHESIZED VIA THE SOL-GEL
METHOD**

Brasília

2019

Marco Antonio Rodriguez Martinez

**SYNTHESIS AND CHARACTERIZATION OF THE
STRUCTURAL, MICROSCOPIC AND MAGNETIC PROPERTIES
OF FeNi NANOPARTICLES SYNTHESIZED VIA THE SOL-GEL
METHOD.**

Tese apresentada ao Programa de Pós-Graduação do Instituto de Física
da Universidade de Brasília, como parte dos requisitos para obtenção
do grau de Doutor em Física Experimental

Orientador:

Dr. José Antonio H. Coaquira

Brasília

2019

Ficha catalográfica elaborada automaticamente,
com os dados fornecidos pelo(a) autor(a)

Rs RODRIGUEZ MARTINEZ, MARCO ANTONIO
Synthesis and characterization of the structural,
microscopic and magnetic properties of FeNi nanoparticles
synthesized via the sol-gel method / MARCO ANTONIO
RODRIGUEZ MARTINEZ; orientador Jose Antonio Huamani
Coaquira. -- Brasília, 2019.
105 p.

Tese (Doutorado - Doutorado em Física) -- Universidade de
Brasília, 2019.

1. Magnetos Permanentes. 2. Fase de FeNi ordenado. 3.
Pico de reflexão de superestrutura. I. Huamani Coaquira,
Jose Antonio, orient. II. Título.

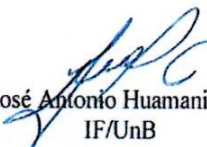
“Synthesis and characterization of the structural,
microscopic and magnetic properties of FeNi
nanoparticles synthesized via the sol-gel method.”


Por

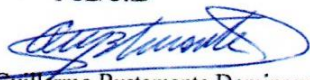
Marco Antonio Rodriguez Martinez.

Tese submetida ao Instituto de Física da Universidade de Brasília como parte dos
requisitos para a obtenção do grau de Doutor em Física.

Aprovada por:


Prof. José Antonio Huamani Coaquira
IF/UnB


Prof. Marcelo Henrique Sousa
FCE/UnB


Prof. Angel Guillermo Bustamante Dominguez
UNMSM


Prof. José André Filho
UDF

Prof. Dr. Geraldo Magela e Silva
Coordenador de Pós-Graduação
Instituto de Física

*Este trabalho foi feito pelos sacrifícios de
meu pai Leoncio, da minha mãe Carmela e
de meu super irmão e melhor amigo Leo.*

Agradecimentos

Agradeço a minha família pelo total apoio dado durante todos esses anos de estudo e pesquisa.

Para meu orientador, o Dr. José Coaquira, por tantas e muitas horas de dedicação e paciência para comigo durante todos esses anos, anos nos quais eu aprendi muito. Tenha meu sincero agradecimento.

Meus agradecimentos para a Dra. Lizbet L. Felix, por sua importante contribuição científica para o desenvolvimento deste trabalho.

Aos meus bons amigos: Dr. José André Filho, Dr. Fermin H. Aragon, Dr. John Mantilla e Dr. Mohan Chandra Mathpal por todos esses longos anos de convivência e de muitos aprendizados, pelo qual agradeço.

Agradeço à Universidade de Brasília, professores do IF e a todo seu pessoal por todo o que eu recebi e aprendi em todos esses anos.

Meus agradecimentos para as agências CNPq e CAPES pelas bolsas concedidas sem as quais nada teria sido possível.

E por ultimo, agradeço de coração ao Brasil, por ter me acolhido como mais um filho nesta terra abençoada.

RESUMO

O objetivo desta tese é a síntese e caracterização estrutural, morfológica, química e magnética de nanopartículas de FeNi. Uma fase especial de FeNi (fase ordenada $L1_0$ -FeNi), tecnologicamente procurada por suas propriedades magnéticas e estruturais muito interessantes é sintetizada. Essas propriedades estão relacionadas ao parâmetro de ordem química (S). Essa fase naturalmente formada (tetrataenita) é encontrada apenas em meteoritos formados ao longo de bilhões de anos. Para este propósito, a síntese da liga FeNi foi realizada adaptando o método sol-gel. O produto foi recozido em forno tubular sob atmosfera redutora a diferentes temperaturas de 400°C a 1150°C. A fim de identificar a quantidade em peso dos elementos de Fe e Ni em todas as amostras, suas composições elementares foram investigadas por fluorescência de raios X (FRX) e mapeamento elementar a partir de espectros de dispersão de energia (EED). As composições químicas do Ni em todas as amostras são superiores a 45% em peso, o que está em inteira concordância com a faixa de valores da composição química para o domínio de estabilidade da superestrutura $L1_0$ -FeNi reportada para meteoritos naturais.

Os resultados obtidos a partir da difração de raios X (DRX) das amostras tratadas a temperaturas inferiores a 700°C indicam a formação de fases de FeNi desordenadas e outras fases impuras. As medidas de difração de raios-x síncrotron (DRXS) mostraram a presença da reflexão (100) própria da superestrutura da fase ordenada de FeNi ($L1_0$ -FeNi) nas amostras tratadas a 800°C, 900°C e 1000°C. A intensidade desta reflexão é muito fraca, devido à pequena diferença entre os fatores de espalhamento atômico de Fe e Ni. O DRXS revelou a coexistência da fase ordenada com a fase da magnetita. Um valor S de 0,81 foi estimado, o que é maior do que o calculado para a Tetrataenita. A amostra recozida a 700°C não mostrou essa reflexão da superestrutura. Imagens de

microscopia eletrônica de transmissão de alta resolução confirmaram os resultados de DRXS, mostrando claramente a coexistência das fases de magnetita e de $L1_0$ -FeNi ordenado. Por outro lado, um pico endotérmico em $\sim 331.5^\circ\text{C}$ foi determinado por medidas de DSC que foi atribuído ao início da formação da fase desordenada de FeNi. Isto foi confirmado por DRX da amostra recozida a 300°C . Espectroscopia Mössbauer mostrou a presença de um sexteto magnético com deslocamento quadrupolar (QS) devido à simetria tetragonal em torno do átomo de Mössbauer, confirmando a presença da fase ordenada de FeNi. Outro sexteto com QS nulo, indicou a presença da fase desordenada do FeNi. DRX não detectou a presença de ambas as fases. Um comportamento diferente do relatado na literatura para o Q.S da fase ordenada em função do parâmetro de ordenamento químico foi encontrado. As medidas de magnetização indicaram que os valores da magnetização de saturação encontrados nas amostras estudadas são valores próximos ou superiores aos relacionados com a Tetrataenite. Embora o campo coercitivo das amostras não corresponda a uma fase ordenada, o campo mostra uma tendência decrescente com o aumento do tamanho das partículas, comportamento típico dos ímãs permanentes. Além disso, o campo coercitivo está mais relacionado à anisotropia da forma do que à anisotropia magnetocristalina, uma vez que é mostrada uma forma circular para as nanopartículas recozidas a 700°C e uma forma retangular para nanopartículas recozidas a 1000°C . O valor da anisotropia magnetocristalina para a amostra tratada a 1000°C corresponde ao encontrado na fase natural. As temperaturas de bloqueio e de Curie foram calculados para serem consistentes com o reportado na literatura.

Palavras-chave: material magnético duro, $L1_0$ -FeNi ordenado, parâmetro de ordem, DRXS.

Abstract

The aim of this thesis is the synthesis and structural, morphological, chemical and magnetic characterization of FeNi nanoparticles. A special phase of FeNi ($L1_0$ -FeNi ordered phase), technologically searched for its very interesting magnetic and structural properties is synthesized. These properties are related to the chemical ordering parameter (S). This phase naturally formed (Tetrataenite) is only found in meteorites formed over billions of years. For this purpose, the synthesis of the FeNi alloy was performed by adapting the sol-gel method. The product was annealed in a tubular furnace under reducing atmosphere at different temperatures from 400°C to 1150°C. In order to identify the amount of Fe and Ni in all samples, their elemental compositions were investigated by x-ray fluorescence (XRF) and elemental mapping from energy dispersive spectra (EDS) experiments. The chemical compositions of the Ni in all samples are greater than 45wt.%, which is in a whole agreement with the range of values of the chemical composition to the stability domain of the $L1_0$ -FeNi superstructure reported for natural meteorites. The results obtained from X-ray diffraction (XRD) of the samples treated at temperatures below 700°C indicate the formation of disorderd FeNi phase and other impure phases.. Measurements of synchrotron x-ray diffraction (SXRD) showed the the presence of the (100) superlattice reflection of the ordered phase of FeNi ($L1_0$ -FeNi) in the samples treated at 800°C, 900°C and 1000°C. The intensity of this reflection is very weak which is due to the very small difference between the atomic scattering factors of Fe and Ni. SXRD revealed the coexistence of the ordered phase with the magnetite phase. A S value of 0.81 was estimated, which is greater than that calculated for the Tetrataenite. The sample annealed at 700°C did not show that superstructure reflection. High resolution transmission electron microscopy images confirmed the results of SXRD, showing

clearly the coexistence of magnetite and the $L1_0$ -FeNi ordered phases. On the other hand, an endothermic peak at $\sim 331.5^\circ\text{C}$ determined by DSC measurements was attributed to the start of the formation of the disordered phase of FeNi which was confirmed by XRD of the sample annealed at 300°C . Spectroscopy Mossbauer showed the presence of a magnetic sextet with quadrupole shift (QS) due to the tetragonal symmetry surrounding the Mossbauer atom, confirming the presence of the ordered phase of FeNi. Another sextet with QS null indicates the presence of the disordered phase of FeNi. XRD did not detect the presence of both phases. A different behavior from that reported in the literature for the Q.S of the ordered phase as a function of the ordering parameter was found. Magnetization measurements indicated that the values of the saturation magnetization found in the studied samples are values close to or greater than that reported for the Tetraenaite. Although the coercive field of the samples does not correspond to an ordered phase, it shows a decreasing tendency with the particle size, typical behavior of permanent magnets. Also, the coercive field is more related to the shape anisotropy than to the magneto-crystalline anisotropy as it is shown a circular form for nanoparticles at annealed at 700°C and a rectangular form for nanoparticles at annealed at 1000°C . The value of the magneto-crystalline anisotropy for the sample treated at 1000°C corresponds to that found in the natural phase. The blocking and Curie temperature were calculated to be consistent with that reported in the literature.

Keywords: hard magnetic material, $L1_0$ ordered FeNi, order parameter, SXR.D.

Summary

Resumo	5
Abstract	7
CHAPTER I	
1.1 Introduction	11
1.2 General objectives	14
1.3 Specific objectives	14
CHAPTER II: REVIEW OF THE SCIENTIFIC LITERATURE	
2.1 Properties of the L1 ₀ -ordered FeNi phase	15
2.1.1 Definitions and structural properties	15
2.1.2 Hyperfine properties	21
2.2 Theoretical aspects	23
2.2.1 Hyperfine properties with Mössbauer Spectroscopy	23
2.2.2 Definitions and magnetic properties	29
2.2.3 Brief meteorological history, properties of the natural ordered phase of FeNi (Tetratenite) and attempts to synthesize the ordered phase in laboratory	35
CHAPTER III: MATERIALS, SYNTHESIS OF SAMPLES AND CHARACTERIZATION TECHNIQUES	
3.1 Materials	39
3.2 Procedure of FeNi nanoparticles synthesis	39
3.2.1 Modified sol-gel method	39
3.3 Characterization techniques	41
3.3.1 X-ray diffraction	41
3.3.2 Magnetic characterization	42
3.3.3 Transmission Electron Microscopy	43
3.3.4 Fourier Transform Infrared absorption spectrometry	43
3.3.5 Differential scanning calorimetry	44
3.3.6 Energy dispersive X-ray spectroscopy	45
3.3.7 X-ray fluorescence spectrometry	46
3.3.8 Mossbauer spectroscopy	47

3.3.9 X-ray photoelectron spectroscopy	49
--	----

CHAPTER IV: RESULTS AND DISCUSSIONS

4.1 DETERMINATION OF THE L ₁₀ -ORDERED PHASE IN FENI NANOPARTICLES	50
---	----

4.1.1 Chemical, structural and morphological properties	50
---	----

4.1.2 Hyperfine Properties	74
----------------------------	----

4.1.3 Magnetic Properties	84
---------------------------	----

CONCLUSIONS	97
--------------------	----

FUTURE WORKS	99
---------------------	----

REFERENCES	100
-------------------	-----

Chapter I

1.1 Introduction

Meteorites are pieces of stone, iron or stony-iron conglomerates from outer space which had entered the earth's atmosphere during our history. Within major types of meteorites [1], we have iron meteorites and stony meteorites with iron-nickel alloys and silicates as the major components, respectively. Since 1977, it has been known that an alloy of Fe and Ni compounds is formed by an ordered crystalline structure in slow-cooled meteorites that contain taenite (fcc iron-nickel alloy). Some years later, this naturally occurring compound was named Tetrataenite [2] due to the tetragonal structure and its close connection to taenite. In many meteorites, it is a common accessory mineral and in some it is more abundant than taenite. Tetrataenite is a natural $L1_0$ -FeNi ordered phase mainly found in meteorites and its existence was first evidenced via Mossbauer spectroscopy experiments [3-5]. Tetrataenite forms in a nominal equiatomic composition of Fe and Ni with a tetragonal crystal structure ($L1_0$) or AuCu I structure type with a space group $P4/mmm$. Tetrataenite is a ferromagnetic compound with a high coercivity (500-4000Oe) and magnetic anisotropy ($1.3 \times 10^6 \text{J/m}^3$). It is entirely larger value compared to common FeNi alloys, that is to say disordered FeNi phases such as face-centered cubic (fcc) and body-centered cubic (bcc) phases [6-8], namely $L1_0$ -FeNi is characterized as a hard ferromagnet [9] with a strong anisotropy despite the fact that common FeNi alloys are classified as a soft magnet [10]. Magnetic anisotropy energy (MAE) is commonly explained as an extra anisotropy energy caused by a symmetry breaking in the lattice [11-13]. $L1_0$ -FeNi is described as an ordered alloy of Fe and Ni with a face-centered tetragonal (fct) superstructure, in which Fe and Ni single atomic layers are alternately parallel in the c-axis direction [14]. Naturally, MAE arises from

spin-orbit interaction, which causes the presence of anisotropic orbital moment with respect to the crystal axes, and it consequently leads to the alignment of the spin moment along the orbital moment [11].

For the continuous technological development, the fabrication of functional magnetic materials free of rare earth elements is strongly investigated. Ferromagnets with ordered crystalline structures ($L1_0$) are excellent candidates to be used as magnetic memories or permanent (hard) magnets because of their strong magnetic anisotropy and large coercivity [15].

The known hard ferromagnets such as NdFeB (neodymium magnet) [16] and SmCo (samarium–cobalt *magnet*)[17] use large quantities of rare earth metals and from viewpoints of ecology, resource depletion and expensive prices, a rare-earth metal-free $L1_0$ -ferromagnet consisting of Fe and Ni has recently been attracting much attention [18] because of both metals are abundant and inexpensive in the nature. The production of synthetic ordered (Tetrataenite) phase in the laboratory is considered very difficult because of its low order-disorder phase transition temperature (around 320°C), in comparison to the order-disorder phase transition temperature of, for instance, CoPt nanoparticles which form in the $L1_0$ -ordered phase at around 500–650 °C [19]. The transition temperature of Tetrataenite provokes extremely low atomic mobilities of Fe and Ni. The atomic diffusivity is expected to be around one atomic jump per 1000 years at 300°C [20] what means that the diffusion of the metallic atom is too slow. This is the reason why Tetrataenite takes hundreds of millions of years to form in its ordered phase inside meteorites.

For decades until now, many attempts were made to obtain artificially this $L1_0$ -ordered FeNi phase. Some attempts using non-equilibrium method such as neutron

bombardment under the influence of a magnetic field [21], alternate monatomic layer deposition using molecular beam epitaxy [22], mechanical alloying [23], high pressure torsion [24], thin film grown on different types of buffer layers [25,26], the transformation from an amorphous to stable crystalline phase [27] and through a new method that consists in nitrogen insertion and topotactic extraction [28] were reported in the literature. A high atomic diffusivity is possible to reach at low temperatures via crystalline ordering stages passing from an initial crystalline phase to the disordered phase and finally achieving the ordered phase by means of heat treatments in each stage of the crystallization process [27].

In this work, we successfully synthesized the $L1_0$ -FeNi phase using a sol-gel method and a specific annealing process. This is a simple and cheap method, which does not need a complicated experimental assembly or consume large amounts of energy. We determined the formation of Bragg's reflections corresponding to the $L1_0$ -ordered FeNi phase, which coexists with the magnetite phase. The stoichiometric range of Fe and Ni to obtain $L1_0$ -ordered FeNi is discussed. The degree of atomic ordering is estimated for the samples and its correlation with the thermal annealing process was studied. The magnetic and hyperfine properties of this $L1_0$ -FeNi phase are also discussed. It is good mentioning that the hyperfine properties are hardly discussed in the literature for the ordered phase synthesized in the laboratory.

1.2 General Objective

Artificially reproduce the ordered phase of FeNi and study the properties that guarantee its stability and those that describe a permanent magnet.

1.3 Specific Objectives

- ✓ To synthesize FeNi nanoparticles by the sol-gel method to obtain samples of good quality and reliable reproducibility.
- ✓ To study the structural properties of FeNi nanoparticles by conventional X-ray diffraction and synchrotron light.
- ✓ To study the magnetic and hyperfine properties of FeNi particles.
- ✓ Through clear evidence show the formation of the ordered phase of FeNi and be able to differentiate it from any impure phase of similar diffractogram with this ordered phase.
- ✓ Apply other characterization techniques that help to verify the presence of this ordered phase or to complement information of the formation of this phase.

Chapter II

REVIEW OF THE SCIENTIFIC LITERATURE

2.1 Properties of the L1₀-ordered FeNi phase

2.1.1 Definitions and structural properties

For a concrete and adequate explanation, we will take as a basic example, solid substitutional solutions formed by 2 kinds of atoms. The two kinds of atoms A and B are arranged at random on the atomic sites of the lattice. (A could be Fe atoms and B could be Ni atoms or vice versa). When this solution is cooled below a certain critical temperature T_c , the atoms A arrange themselves in an orderly, periodic manner at one set of atomic sites, and the atoms B at the other set. The solution is then said to be ordered or to possess a superlattice. When this periodic arrangement of atoms A and B persists over very large distances in the crystal, it is known as long-range order (LRO). If the ordered solution is heated above T_c , the atomic arrangement becomes random again and the solution is said to be disordered. This T_c is also called the order-disorder transformation temperature.

When the atomic arrangement becomes ordered, changes are produced in the physical and chemical properties of the substance that will be related with this new ordered structure. However, one of the main evidences for a disorder-order transformation is a particular kind of changes in the x-ray diffraction pattern of the substance.

As already mentioned, we consider a binary element and call the two kinds of atoms A and B. In the ordered structure, we have two kinds of positions that are named as α - and β -sites. When the α -sites are all occupied by A-atoms and the β -sites by B-atoms, we are talking about an ideal stoichiometric composition and perfect LRO. The

composition of the sample is represented by the atom fractions x_A and x_B , where $x_A + x_B = 1$. The number of atoms in the sample will be named N , such as $N_A = x_A N$ and $N_B = x_B N$. Now, y_α and y_β will be the fractions of α -sites and β -sites, where $y_\alpha + y_\beta = 1$. These are simple fractions that will be defined by the type of ordered structure. The number of each kind of site is given by $N_\alpha = y_\alpha N$ and $N_\beta = y_\beta N$.

We will use four very useful parameters:

r_α : fraction of α -sites occupied by the right atom (A-atom)

w_α : fraction of α -sites occupied by the wrong atom (B-atom)

r_β : fraction of β -sites occupied by the right atom (B-atom)

w_β : fraction of β -sites occupied by the wrong atom (A-atom)

As it is obvious, we can form two relations with those parameters:

$$r_\alpha + w_\alpha = 1 \ ; \ r_\beta + w_\beta = 1 \quad (2.1)$$

We have to include the conditions that the fraction of the sites occupied by A-atoms must be equal the fraction of A-atoms, and the same way by B-atoms, the fraction of the sites occupied by B-atoms must equal the fraction of B-atoms. Both conditions are expressed by:

$$y_\alpha r_\alpha + y_\beta w_\beta = x_A \ ; \ y_\beta r_\beta + y_\alpha w_\alpha = x_B \quad (2.2)$$

We will calculate the LRO parameter S for nonstoichiometric compositions. This parameter is defined as being linearly proportional to $(r_\alpha + r_\beta)$, with $S = 0$ for a completely random arrangement and $S = 1$ when the composition is stoichiometric and $r_\alpha = r_\beta = 1$. Mathematically, this linear dependence is expressed by $S = a + b(r_\alpha + r_\beta)$, and using the two values for S as already said, the LRO parameter S is given by:

$$S = r_\alpha + r_\beta - 1 \quad (2.3)$$

and using Equation (2.1), we also have:

$$S = r_\alpha - w_\beta = r_\beta - w_\alpha \quad (2.4)$$

Substituting, the value of w_β of equation (2.2), in equation (2.4), we have that:

$$S = r_\alpha - \left(\frac{x_A - y_\alpha r_\alpha}{y_\beta}\right) \rightarrow S = \frac{r_\alpha(y_\beta + y_\alpha) - x_A}{y_\beta} \quad \text{and finally,}$$

$$S = \frac{r_\alpha - x_A}{y_\beta} \quad (2.5)$$

For a stoichiometric composition, the S -value will be of unity which is its maximum value and for a nonstoichiometric composition, the parameter value will be less than unity. With this definition of S , the structure factors for the super-structure reflections turn out to be proportional to S . As it is well known, the structure factor involves a sum over all the atomic positions in the unit cell. As we have two positions in our initial structure, this structure factor contains two terms, a sum over the α -positions and a sum over the β -positions using the average scattering factor for each kind of site, we have:

$$F = \sum_{\alpha} (r_\alpha f_A + w_\alpha f_B) e^{2\pi i(hx_n + ky_n + lz_n)} + \sum_{\beta} (r_\beta f_B + w_\beta f_A) e^{2\pi i(hx_n + ky_n + lz_n)} \quad (2.6)$$

For the case of partial LRO, we now apply Eq. (2.6) to the ordered (to be a crystal cell) structure shown by Fig.2.1a that is to say for a body centered tetragonal (bct) structure, but without assuming stoichiometric compositions.

The positions (x_n, y_n, z_n) of the α -sites and β -sites and the fractions of both sites (y_α, y_β) are:

$$\alpha = (0,0,0) - (Ni); \quad y_\alpha = \frac{1}{2}$$

$$\beta = \left(\frac{1}{2}, \frac{1}{2}, \frac{1}{2}\right) - (Fe); \quad y_\beta = \frac{1}{2}$$

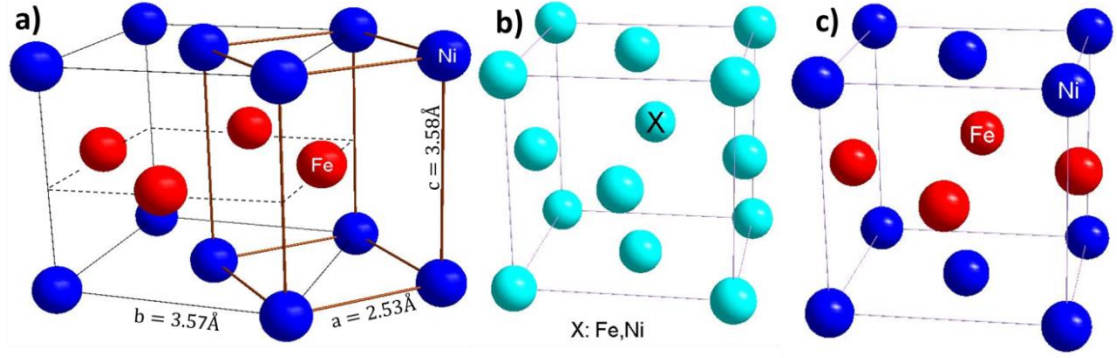


Figure 2.1 a) Unit cells based on fcc and bct with lattice parameters for L1₀-ordered FeNi. b) Unit cell based on fcc of disordered FeNi. c) Unit cell based on fcc of ordered FeNi.

Substituting in Eq. (2.6):

$$F = (r_{\alpha}f_A + w_{\alpha}f_B) + (r_{\beta}f_B + w_{\beta}f_A)e^{\pi i(h+k+l)}$$

If $h + k + l = \text{even}$, we obtain:

$$F = (r_{\alpha}f_A + w_{\alpha}f_B) + (r_{\beta}f_B + w_{\beta}f_A) \quad (2.7)$$

Now, using the Eq. (2.1), we have the following:

$$F = r_{\alpha}f_A + r_{\beta}f_B + (1 - r_{\alpha})f_B + (1 - r_{\beta})f_A$$

Factoring f_A and f_B :

$$F = f_A(r_{\alpha} + 1 - r_{\beta}) + f_B(r_{\beta} + 1 - r_{\alpha}); \text{ and remembering that } r_{\alpha} + r_{\beta} = 1, \text{ we have}$$

$$F = f_A(2r_{\alpha}) + f_B(2r_{\beta}); \text{ and as } x_A = r_{\alpha}; x_B = r_{\beta}, \text{ finally we get:}$$

$$F = 2(x_A f_A + x_B f_B), \quad (2.8)$$

for the Fundamental peak.

If $h + k + l = \text{odd}$, we obtain:

$$F = (r_{\alpha}f_A + w_{\alpha}f_B) - (r_{\beta}f_B + w_{\beta}f_A)$$

Using Eqs. (2.2), (2.4) and (2.5):

$$F = (w_{\alpha}f_B - r_{\beta}f_B) + r_{\alpha}f_A - w_{\beta}f_A$$

$$F = f_B(w_{\alpha} - r_{\beta}) + r_{\alpha}f_A - \frac{(x_A - y_{\alpha}r_{\alpha})}{y_{\beta}} f_A$$

$$F = f_B(-S) - \frac{(x_A f_A - r_\alpha f_A (y_\alpha + y_\beta))}{y_\beta}$$

$$F = f_B(-S) - \frac{f_A(x_A - r_\alpha)}{y_\beta}$$

$$F = f_B(-S) + f_A(S)$$

$$F = S(f_A - f_B) \quad (2.9)$$

for the Superstructure peak.

With all this information, in X-ray diffractograms can be expected some fundamental peaks and superstructure peaks for tetragonal crystal structure (see Fig. 2.1a) with the following Miller indices as shown in Table 2.1.:

Table 2.1 Miller indices for peaks of the L1₀-ordered FeNi phase.

Fundamental peak ($h + k + l = \text{even}$)	(110), (101), (002), (200), (112), (202), (220)
Superstructure peak ($h + k + l = \text{odd}$)	(100), (001), (210), (102), (111), (201), (003)

Reflections which are independent of the degree of order are called fundamental reflections, and reflections which vanish if the order vanishes are called superstructure reflections.

The diffraction peaks are called fundamental peaks, since they occur at the same positions and with the same intensities in the patterns of both ordered and disordered alloys. The extra lines which appear in the pattern of an ordered alloy are called superlattice peaks, and their presence is a direct evidence that ordering has taken place. The physical reason for the formation of superlattice lines can be inferred from Figure 2.1 b and c.

Let's consider in more details and let's suppose reflection from the (100) planes of the disordered structure, and that this incident beam of wavelength (λ) make such an angle of incidence θ that the path difference between rays scattered by adjacent (100) planes

is proportional to λ . But there is another plane halfway between these two, containing, on the average, exactly the same distribution of iron and nickel atoms. This plane scatters a wave which is therefore $\lambda/2$ out of phase with the wave scattered by either adjacent (100) plane and of exactly the same amplitude. Complete cancellation results and there is no (100) reflection. In the ordered structure, on the other hand, adjacent (100) planes contain only nickel atoms, but the halfway plane between them contains only iron atoms. The rays scattered by the (100) planes and those scattered by the halfway planes are still exactly out of phase, but they now differ in amplitude because of the difference in scattering power of the iron and nickel atoms. Therefore, the ordered structure produces a weak 100 reflection.

Before showing the formula for calculating the S parameter, we need to know how to calculate the theoretical integrated intensity of a diffraction peak. The integrated intensity of a diffraction peak is given by the following formula [29]:

$$I = |F|^2 p \left(\frac{1 + \cos^2 2\theta}{\sin^2 \theta \cos \theta} \right) \quad (2.10)$$

Where I is the relative integrated intensity (arbitrary units), F is the structure factor, p is the multiplicity factor, and θ is the Bragg angle. To get to this equation, we have omitted factors which are constant for all diffraction lines of the pattern. The term $\left(\frac{1 + \cos^2 2\theta}{\sin^2 \theta \cos \theta} \right)$ is the Lorentz polarization (LP) when a conventional x-ray source is used.

With synchrotron radiation source, the LP is $\left(\frac{\cos^2 2\theta}{\sin^2 \theta \cos \theta} \right)$ considering an ideal polarization (polarization constant equal to 1). The average scattering factor f is composed of the sum of three terms: f_0 is a normal scattering factor, f' and f'' are real and imaginary parts of an anomalous scattering factor. Here, we have omitted the temperature and absorption factors and it is valid only for the Debye-Scherrer method.

Finally, the S value is estimated using the following formula:

$$S = \sqrt{\frac{[I_S/I_f]^{obs}}{[I_S/I_f]_{S=1}^{calc}}} \quad (2.11)$$

Where I_S and I_f are peak intensities of the superlattice and the fundamental peaks, respectively, and superscripts of *obs* and *calc* indicate experimentally observed values and theoretically calculated values.

2.1.2 Hyperfine properties

Tetrataenite has been found in meteorite samples with other phases such as silicates, troelite, taenite, kamacite, martensite, phases rich in Fe or Ni, disordered FeNi alloys, etc. The most appropriate technique used in research to detect Tetrataenite with mixed phases is through Mossbauer spectroscopy (MS) based on the fact that the ordered phase exhibits an asymmetric six-line spectrum due to a quadrupole splitting arising from the non-cubic environment of the Fe atoms in this structure. For a better understanding of the results presented in this thesis work, we will provide a review that summarizes the general hyperfine properties of this ordered phase of FeNi using Mossbauer spectroscopy. This summary is based on the results obtained by Scorzelli et al. [30] and Danon et al. [31]

Scorzelli et al. [30] reported the presence of tetrataenite in metal particles of the meteorite called Antarctic L6 chondrite ALHA 76009 [32]. It was investigated by MS, XRD, scanning electron microscopy and magnetic measurements. The transmission ^{57}Fe Mossbauer spectra were obtained at room temperature (RT) and at 4.2 K using a Co/Rh source in a conventional Mossbauer spectrometer. The Mossbauer spectrum at RT of the metal-enriched sample shows the coexistence of Fe-Ni phases with different compositions with an overlap of: (a) a magnetic phase with a quadrupole splitting,

corresponding to the ordered $\text{Fe}_{50} - \text{Ni}_{50}$ (tetrataenite); (b) a magnetic phase without quadrupole splitting, corresponding to a ferromagnetic disordered taenite $\text{Fe}_{50} - \text{Ni}_{50}$; (c) a paramagnetic γ -phase due to the Ni-poor taenite with less than 30% Ni. The hyperfine parameters (see Table 1 in Ref. 30) such as the hyperfine field (28.8T) and the quadrupolar splitting (0.18mm/s) are similar to those already observed for the ordered phases in irradiated iron nickel alloys and in metal particles of LL and L non-Antarctic chondrites (meteorites). The presence of a considerable proportion of the $\text{Fe}_{50}-\text{Ni}_{50}$ disordered phase coexisting with the superstructure is remarkable.

Danon et al. [31] has shown using MS, XRD and scanning electron microscopy measurements that the metal particles of the eight analyzed meteorites contain different proportions of the $L1_0$ -ordered FeNi phase. In all the samples, the presence of this ordered phase is detected by a magnetic sextet with a negative isomer shift (relative to α -Fe) and values for the quadrupolar splitting between +0.13 and +0.24 and with values of 297 to 302 kOe for the hyperfine magnetic field. Here, it is important to mention, that $L1_0$ -ordered FeNi phase has been found together with the disordered FeNi phase (paramagnetic taenite). The hyperfine parameters of the meteorites samples are shown (see Table 1 in Ref. 31) with the proportions of FeNi alloy phases in each sample. Although the ordered phase has not been detected by Mossbauer technique in one of the samples (Nadiabondi meteorite), its X-ray pattern exhibited a weak (100) superstructure line. In the sample with the larger amount of ordered FeNi phase, the composition of each element was found to be Fe (60%) and Ni (40%), in the domain of stability of the $L1_0$ superstructure [33]. Comparing meteorites with evidence and with little evidence of a shock event, it suggests that the shock event, either from pressure effects [34] or by impact heating, tends to disorder the Fe-Ni superstructure ($T_c = 320^\circ\text{C}$), as indicated by the decrease in the value of the quadrupole splitting [4].

2.2 Theoretical aspects

2.2.1 Hyperfine properties with Mössbauer Spectroscopy

Mössbauer spectroscopy provides unique characterization of electronic, magnetic, and structural properties of materials. Mössbauer spectroscopy looks at materials from the “inside out,” where “inside” refers to the resonant nucleus. For one nucleus to emit a γ -ray and a second nucleus to absorb it with efficiency, both nuclei must be embedded in solids, a phenomenon known as the “Mössbauer effect.” Mössbauer spectra give quantitative information on “hyperfine interactions,” which are small energies from the interaction between the nucleus and its neighboring electrons. The three important hyperfine interactions are: the isomer shift (IS) related with the electron density at the Mössbauer nucleus; the nuclear quadrupole splitting (QS) related to gradient of the electric field applied at the Mössbauer nucleus by neighboring electrons to this, and the hyperfine magnetic field (B_H) ascribed to the unpaired electron density at the nucleus.

2.2.1.1 Isomer Shift

The peaks in a Mössbauer spectrum undergo observable shifts in energy when the Mössbauer atom is in different materials (isomer effect) as shown in Fig. 2.2a-b. These shifts originate from a hyperfine interaction involving the nucleus and the inner electrons of the atom. This concept of IS is in proportion to the electron density at the nucleus. Two possibly unfamiliar definitions underlie the origin of the isomer shift. First, some atomic electron wavefunctions are actually present inside the nucleus. Second, the nuclear radius is different in the nuclear ground and excited states.

In solving the Schrödinger equation for radial wavefunctions of electrons around a point nucleus, it is found that when the nuclear radius tends to zero (i.e., toward the nucleus) the electron wave functions go as r^l , where l is the angular momentum quantum number

of the electron. For s electrons (1s, 2s, 3s, 4s, etc.) the value of l is zero, then the electron wavefunction is quite large at $r = 0$. This allows us to infer that the presence of wavefunctions of s electrons is strong inside the nucleus. For this reason, the s electrons are actually present inside the nucleus. Furthermore, the electron density is essentially constant across the small size of the nucleus.

The overlap of the s-electron wavefunction with the finite nucleus provides a Coulomb perturbation that lowers the nuclear energy levels. If the excited state and groundstate energy levels were lowered equally, however, the energy of the nuclear transition would be unaffected, and the emitted (or absorbed) γ ray would have the same energy. It is well known that the radius of an atom changes when an electron enters an excited state. The same type of effect occurs for nuclei—the nuclear radius is different for the nuclear ground and excited states. For ^{57}Fe , the effective radius of the nuclear excited state, R_{ex} , is smaller than the radius of the ground state, R_g . For the overlap of a finite nucleus with a constant charge density, the total electrostatic attraction is stronger when the nucleus is smaller. This leads to a difference in energy between the nuclear excited state and ground state in the presence of a constant electron density $|\psi(0)|^2$. This shift in transition energy will usually be different for nuclei in the radiation source and nuclei in the sample, giving the following shift in position of the absorption peak in the measured spectrum.

$$\Delta E_{IS} = CZe^2(R_{ex}^2 - R_g^2)(|\psi_{sample}(0)|^2 - |\psi_{source}(0)|^2) \quad (2.12)$$

The factor C depends on the shape of the nuclear charge distribution, which need not be uniform or spherical. The sign of Equation (2.12) for ^{57}Fe is such that with an increasing s-electron density at the nucleus, the Mössbauer peaks will be shifted to more negative velocity.

However, there is another way of interpreting the information given by IS. In the case of Fe, the 3d electrons are expected to partly screen the nuclear charge from the 4s electrons. An increase in the number of 3d electrons at an ^{57}Fe atom will therefore increase this screening, reducing the s-electron density at the ^{57}Fe nucleus and causing a more positive isomer shift. The s-electron density at the nucleus is therefore not simply proportional to the number of valence s electrons at the ion. The effect of this 3d electron screening is large for ionic compounds [35]. In these compounds there is a series of trend lines for how the isomer shift depends on the 4s electron density, where the different trends correspond to the different number of 3d electrons at the ^{57}Fe atom [36]. With more 3d electrons, the isomer shift is more positive, but also the isomer shift becomes less sensitive to the number of 4s electrons at the atom. Determining the valence state of Fe atoms from IS is generally used in the scientific experiments. For metals it has been more recently learned that the isomer shifts do not depend on the 3d electron density [37]. In Fe alloys, the isomer shift corresponds nicely to the 4s charge transfer, in spite of changes in the 3d electrons at the Fe atoms.

2.2.1.2 Electric Quadrupole Splitting

The IS already mentioned, is an electric monopole interaction. There is no static dipole moment of the nucleus. The nucleus has an electric quadrupole moment that originates with its asymmetrical shape. The asymmetry of the nucleus depends on its spin, which differs for the ground and excited states of the nucleus. In a uniform electric field, the shape of the nuclear charge distribution has no effect on the Coulomb energy. In an electric field gradient (EFG), however, there will be different interaction energies for different alignments of the electric quadrupole moment of the nucleus. An EFG generally involves a variation with position of the x, y, and z components of the electric field vector.

In specifying an EFG, it is necessary to know, for example, how the x component of the electric field, $V_x = \partial V / \partial x$ varies along the y direction, $V_{yx} = \partial^2 V / \partial y \partial x$ [$V(x, y, z)$ is the electric potential]. The EFG involves all such partial derivatives, and is a tensor quantity. In the absence of competing hyperfine interactions, it is possible to choose freely a set of principal axes so that the off-diagonal elements of the EFG tensor are zero. By convention, we label the principal axes such that $|V_{zz}| > |V_{yy}| > |V_{xx}|$. Furthermore, because the Laplacian of the potential vanishes, $V_{xx} + V_{yy} + V_{zz} = 0$, there are only two parameters required to specify the EFG. These are chosen to be V_{zz} and an asymmetry parameter $\eta = (V_{xx} - V_{yy}) / V_{zz}$ where by definition, $\eta < 1$.

The isotope ^{57}Fe has an excited-state spin of $I = 3/2$ and a ground-state spin of $1/2$. The shape of the excited nucleus is that of a prolate spheroid. This prolate spheroid will be oriented with its long axis pointing along the z axis of the EFG when $I_z = \pm 3/2$. There is no effect from the sign of I_z , since inverting a prolate spheroid does not change its charge distribution. For the excited state, the $I_z = \pm 3/2$ states have a low energy compared to the $I_z = \pm 1/2$ orientations. In the presence of an EFG, the excited state energy is split into two levels. Since $I_z = \pm 1/2$ for the ground state, however, the ground state energy is not split by the EFG. With an electric quadrupole moment for the excited state defined as Q , for ^{57}Fe the quadrupole splitting of energy levels is

$$\Delta E_q = \frac{\pm 1}{4} eQV_{zz} \left(1 + \frac{\eta^2}{3}\right)^2 \quad (2.13)$$

where often there is the additional definition $-eq = V_{zz}$. The energy level diagram is shown in Figure 2.2c.

The EFG is zero when the electronic environment of the Mössbauer isotope has cubic symmetry. When the electronic symmetry is reduced, a single line in the Mössbauer spectrum appears as two lines separated in energy as described by Equation (2.13) (as

shown in Fig. 2.2c). When the ^{57}Fe atom has a 3d electronic structure with orbital angular momentum, V_{zz} is large. High- and low spin Fe complexes can be identified by differences in their electric QS. The electric QS is also sensitive to the local atomic arrangements, such as ligand charge and coordination, but this sensitivity is not possible to interpret by simple calculations. The ligand field gives an enhanced effect on the EFG at the nucleus because the electronic structure at the Mössbauer atom is itself distorted by the ligand. This effect is termed “Sternheimer antishielding,” and enhances the EFG from the ligands by a factor of about 7 for ^{57}Fe [38].

2.2.1.3 Hyperfine Magnetic Field Splitting

The nuclear states have spin, and associated magnetic dipole moments. The spins can be oriented with different projections along a magnetic field. The energies of nuclear transitions are therefore modified when the nucleus is in a magnetic field. The energy perturbations caused by this HMF are sometimes called the “nuclear Zeeman effect,” in analogy with the more familiar splitting of energy levels of atomic electrons when there is a magnetic field at the atom.

A hyperfine magnetic field lifts all degeneracies of the spin states of the nucleus, resulting in separate transitions identifiable in a Mössbauer spectrum by the formation of 6 peaks (Fig. 2.2d) separated symmetrically from each other and with a ratio of intensities of 1: 2: 3. The I_z range from $-I$ to $+I$ in increments of 1, being $\{-3/2, -1/2, +1/2, +3/2\}$ for the excited state of ^{57}Fe and $\{-1/2, +1/2\}$ for the ground state. The allowed transitions between ground and excited states are set by selection rules. For the magnetic dipole radiation for ^{57}Fe , six transitions are allowed: $\{(-1/2 \rightarrow -3/2), (-1/2 \rightarrow -1/2), (-1/2 \rightarrow +1/2), (+1/2 \rightarrow -1/2), (+1/2 \rightarrow +1/2), (+1/2 \rightarrow +3/2)\}$. The allowed

transitions are shown in Figure 2.2d. Notice the inversion in energy levels of the nuclear ground state.

In ferromagnetic iron metal, the magnetic field at the ^{57}Fe nucleus, the HMF, is 33.0 T at 300 K. The enormity of this HMF suggests immediately that it does not originate from the traditional mechanisms of solid-state magnetism.

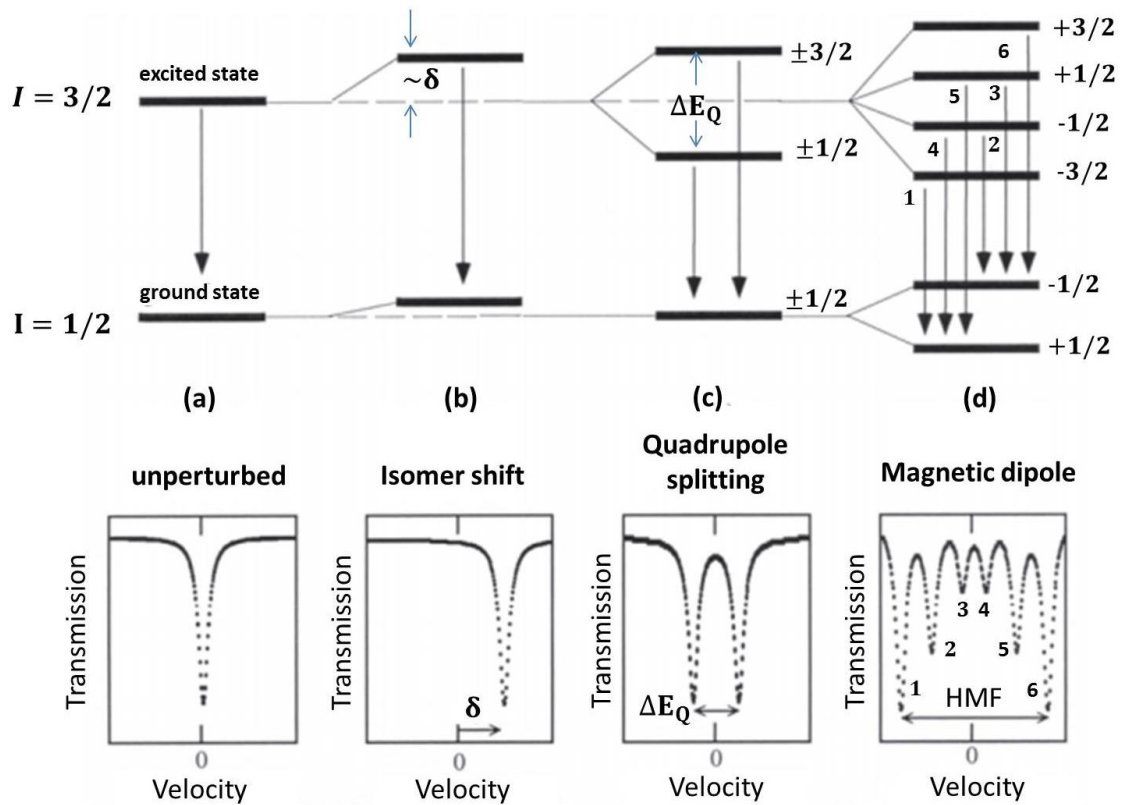


Figure 2.2 Hyperfine interactions for ^{57}Fe nuclei, showing the nuclear energy level diagram for (a) an unperturbed nucleus; (b) electric monopole interaction (isomer shift); (c) electric quadrupole interaction (quadrupole splitting); and (d) magnetic dipole interaction (hyperfine magnetic splitting). Each interaction is shown individually, accompanied by the resulting Mössbauer spectrum.

Furthermore, when an external magnetic field is applied to a sample of Fe metal, there is a decrease in magnetic splitting of the measured Mössbauer peaks. Many times, for this last reason is considered the HMF at the ^{57}Fe nucleus with a sign opposite to that of the lattice magnetization of Fe metal, so the HMF is given as -33.0 T.

2.2.2 Definitions and magnetic properties

2.2.2.1 Ferromagnetism

A ferromagnetic material unlike a paramagnetic material where the atoms have permanent magnetic moments, but with the difference that these moments are not randomly oriented, but they are strongly aligned to the crystallographic axes. Within a single crystal, there exist domains, within which all the magnetic moments are parallel and are aligned with a particular axis. In an adjacent domain, again all the moments are parallel to each other, but they may be aligned with a different axis, perhaps at right angles to the first domain, or perhaps aligned with the same axis but pointing in the opposite direction. Thus we have a number of domains, each highly magnetized, but with some domains magnetized in one direction and some in another. The domains are separated by domain boundaries, or “Bloch walls”, perhaps a few hundred atoms thick, within which the orientation of the magnetic moments gradually changes from one domain to the next. Figure 2.3 shows a simple magnetic representation of a crystal divided into four domains, with the magnetization in a different direction in each and a magnetic field of variable intensity will be applied in this crystal. In Figure 2.4 is shown the magnetization process of the crystal as a whole, this process is called hysteresis loop.

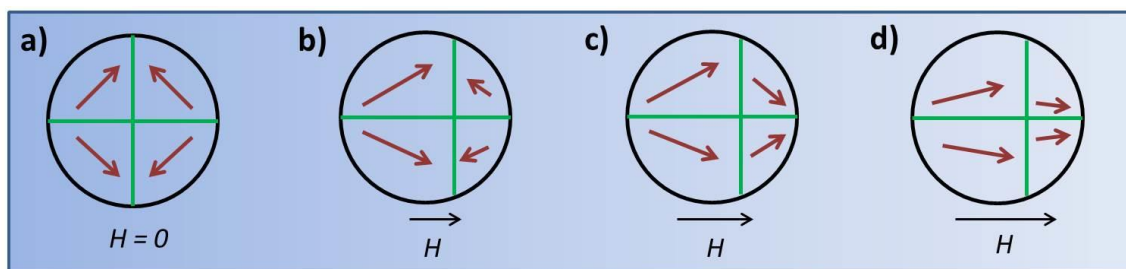


Figure 2.3 Basic design of the magnetization process of a crystal in the presence of an external magnetic field.

When we first apply a weak field (Fig.2.3a and 2.4a), the Bloch walls (domain boundaries) move so that the favorably-oriented domains grow at the expense of the opposing domains, and the magnetization slowly increases. With stronger fields (Fig. 2.3b), suddenly all the magnetic moments (due to unpaired spins) within a single domain change direction almost in unison; so that, an opposing domain suddenly becomes a favorable domain; this happens to one domain after another, until all domains are oriented favorably, and the magnetization of the specimen rapidly increases (Fig. 2.4b). For yet stronger fields (Fig. 2.3c), the magnetic moments, usually oriented parallel to a crystal axis, bend so that they are in the direction of the magnetizing field. When all of that is achieved, no further magnetization is possible (Fig. 2.3d), and the specimen is saturated (Fig. 2.4c).

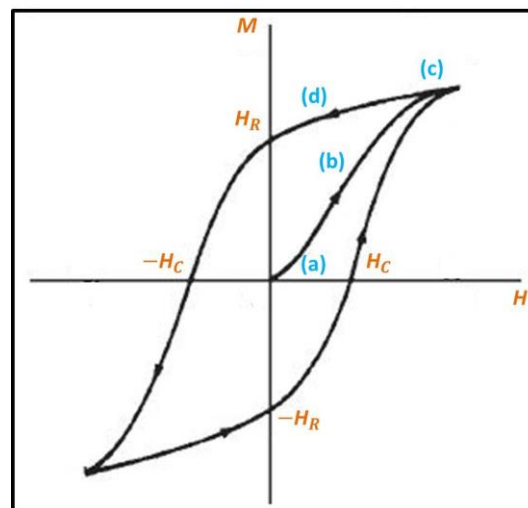


Figure 2.4 Hysteresis loop of a ferromagnetic material. a) Start of the magnetization process. b) Increase of the magnetization with the applied magnetic field. c) Magnetic saturation. d) Irreversible magnetization curve.

Now, if the field is reduced, the magnetic moments relax and take up their normal positions parallel to a crystallographic axis. But, as the field is further reduced, there is no reason for the domains to reverse their polarity as happened at stage (Fig.2.3b). That is, when this stage originally happened, this was an irreversible process (Fig.2.3d). The

demagnetization curve does not follow the magnetization curve in reverse. Consequently, when the magnetizing field has been reduced to zero, the specimen retains a remanent magnetization (indicated by H_R in Figure 2.4), with all domains still favorably oriented. In order to reduce the magnetization to zero, you have to apply a field in the reverse direction. The reverse field needed to reduce the magnetization to zero is called the coercive field (indicated by H_C in Figure 2.4).

As you repeatedly magnetize the specimen first on one direction and then the other, the graph of magnetization versus magnetizing field describes the hysteresis loop indicated in Figure 2.4. Because of the irreversible process (Fig, 2.4d), magnetic energy is dissipated as heat during a complete cycle, the amount of energy loss being proportional to the area of the hysteresis loop. The amount of the hysteresis depends on how freely the domain walls can move, which in turn depends on the physical and chemical constitution of the magnetic materials, particularly on the number of impurities present that can inhibit Bloch wall movement. For a permanent magnet, you need a material with a fat hysteresis loop, with a large remanent magnetization as well as a large coercive force, so that it cannot be demagnetized easily. For a transformer core, you need a material with a narrow hysteresis loop.

The susceptibilities of ferromagnetic materials are typically of order 10^3 or 10^4 or even greater. However, the ferromagnetic susceptibility of a material is quite temperature sensitive, and, above a temperature known as the Curie temperature, the material ceases to become ferromagnetic, and it becomes merely paramagnetic. Among the elements, only cobalt, iron and nickel are strongly ferromagnetic, their Curie temperatures (T_C) being about 1400, 1040 and 630 K respectively. Gadolinium is ferromagnetic at low temperatures; its Curie temperature is about 289 K (16 °C). Dysprosium is

ferromagnetic below its Curie temperature of about 105 K (-168 °C). There are many artificial alloys and ceramic materials which are ferromagnetic.

2.2.2.2 Magnetic anisotropy

Anisotropy is what makes the difference between spin and magnetism. A free atom, regardless of its electronic structure, is always perfectly spherical. Although it may possess a finite amount of spin (as a result of some electron orbitals being half-filled), the lack of anisotropy makes the orientation of the spinning axis intrinsically undetermined and therefore it will never exhibit magnetism.

The tendency to align the angular momentum in a certain direction and the ability to maintain the resulting magnetization over an extended amount of time is governed entirely by the atom's immediate environment.

Generally, the tendency for magnetization to lie along an easy axis is represented by the energy density term: $E_a = K_1 \sin^2 \theta$, where θ is the angle between magnetization (M) as it is shown in Fig.2.5 and the anisotropy axis. K_1 has units $J m^{-3}$.

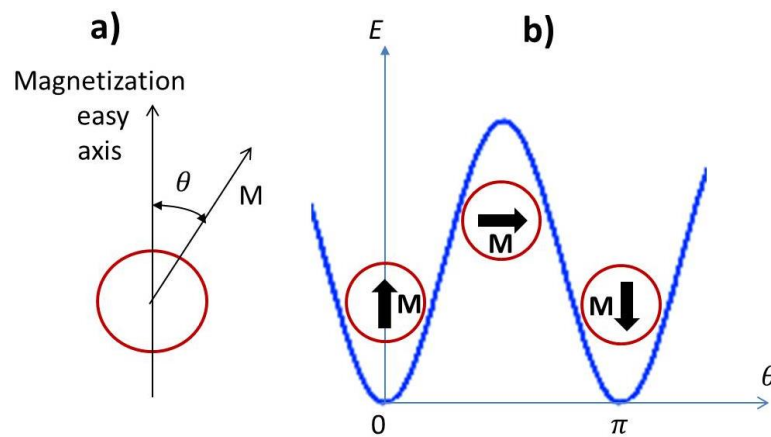


Figure 2.5 a) Vector representation of the easy axis and the magnetization b) The schematic of variation of anisotropy energy as a function of magnetization vector directions.

The anisotropy depends on temperature, and must tend to zero at T_C if there is no applied field. Three main sources of anisotropy are related to sample shape, crystal structure and atomic or micro-scale texture.

✓ **Shape anisotropy**

If the sample's shape is not circularly symmetric then it will experience shape anisotropy. This anisotropy attempts to minimize the energy of the magnetic field applying to the sample. The magnetization would prefer to lie along the long side of the shape (Fig. 2.6a).

✓ **Magnetocrystalline anisotropy**

An anisotropy caused by the crystalline structure of the material is called the magnetocrystalline anisotropy. Depending on the material, it either lies along planes where lattice sites are closest or furthest away. This phenomenon can be understood as the interaction strength of neighboring lattice sites are different along the crystal planes (Fig. 2.6b).

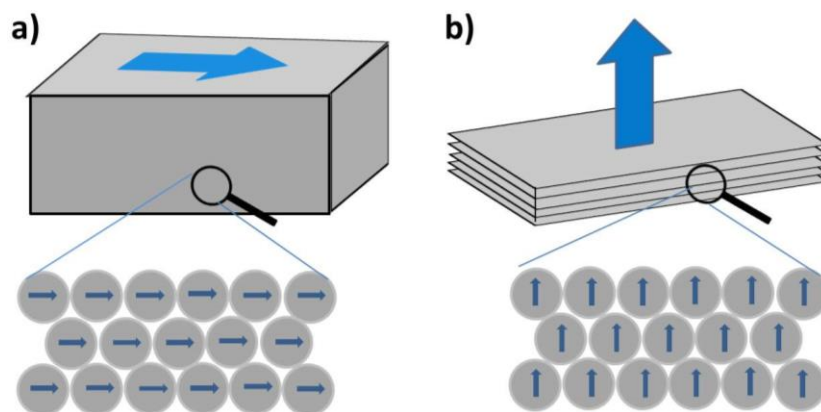


Figure.2.6 a) Magnetostatic shape anisotropy dominates (in-plane magnetic anisotropy)
b) Magnetocrystalline anisotropy dominates (perpendicular magnetic anisotropy).

✓ Magnetoelastic anisotropy

This is an anisotropy caused by stress in thin magnetic films where, for example, the substrate elongates the crystal along one direction. While stretching a film uniaxially, the average bond length between atoms change along one direction and consequently, the inter-atomic interaction length changes anisotropically.

2.2.2.3 Law of approach to saturation magnetization

The law of approach to ferromagnetic saturation is very used for the study of magnetic hysteresis loops of polycrystalline soft magnetic materials [39]. Generally, the law of approach to saturation magnetization is expressed as follows: [40,41]

$$M = M_s \left(1 - \frac{a}{H} - \frac{b}{H^2} \right) + c\sqrt{H} \quad (2.14)$$

where M is the magnetization, M_s the saturation magnetization, and H the magnetic field. a , b and c are constants. The above equation is written in the form of differential susceptibility as follows:

$$\chi = \frac{dM}{dH} = \frac{A}{H^2} + \frac{B}{H^3} + \frac{P}{\sqrt{H}} \quad (2.15)$$

where $A = aM_s$, $B = 2bM_s$ and $P = c/2$. The value of A is a measure of the structural inhomogeneity within magnetic substances, which causes fluctuations of the local interal stress fields, B is a function of the magnetic anisotropy energy and P arises from the paraeffect through which the spontaneous magnetization is increased in an external field. A strong magnetic field suppresses the thermally excited spin waves so as to increase the spontaneous magnetization. If these parameters can be determined experimentally, they will be very helpful in understanding the mechanism of magnetization in nanocrystalline alloys. Especially, if the H^{-3} term in equation (2.15) is

dominant, then the magnetization process is indeed controlled by the magnetic anisotropy, and the magnetic anisotropy can accordingly be determined.

In the case of a ferromagnet with the cubic crystal structure, the constant b in equation

(2.14) is given by: $b = \frac{8}{105} \frac{K_1^2}{M_s^2}$ where K_1 is the cubic anisotropy constant of first order

[42]. From the analysis of the magnetization curve using equations (2.14) and (2.15), the value of K_1 can be estimated as well as that of M_s .

The anisotropy energy for a tetragonal compound is described by:

$$E_a = K_1 \sin^2 \theta + K_2 \sin^4 \theta + K_3 \sin^4 \theta \cos^4 \varphi \quad (2.16)$$

where θ is the angle between the tetragonal axis and the magnetization and φ the angle between the component of the magnetization in the c-plane and one of a-axes. If the higher order terms of K_2 and K_3 in Eq. (2.16) are negligibly small compared with the K_1

term, the constant b is given by [43]: $b = \frac{4}{15} \frac{K_1^2}{M_s^2}$ where K_1 is the tetragonal anisotropy

constant and it is given by

$$K_1 = \frac{\rho}{10} \sqrt{\frac{15}{4} b M_s^2} \quad \left(\frac{\text{J}}{\text{m}^3} \right) \quad (2.17)$$

Where, ρ is the volumetric density of the material in g/cm^3 .

2.2.3 Brief meteorological history, properties of the natural ordered phase of FeNi (Tetratenite) and attempts to synthesize the ordered phase in laboratory

Meteorites are pieces of stone, iron or stony-iron conglomerates, and they range in mass from fractions of gram to hundreds of kilograms. Generally, meteorites are divided into 4 major types [1]: iron meteorites, stony-iron meteorites and stony meteorites (achondrites and chondrites). The major components in iron meteorites are iron-nickel alloys and in stony meteorites are silicates. Among the meteorites actually seen to fall, the chondrites make up the vast majority, whereas the iron meteorites are rather rare [2].

However, relatively more iron meteorites have been found due to the fact that iron meteorites are rather heavy, and thus, it is much easier to distinguish iron meteorites from terrestrial rocks. Further analysis of iron meteorites reveals that their composition also differs from the composition of metallic iron found on earth.

The macrostructure of the iron meteorites (etched section) is due to the presence of the two iron-nickel alloys, kamacite and taenite, which have different etching properties. In this way it is possible to obtain taenite in the form of lamellae of some tens of microns. The first Mossbauer investigation of taenite lamellae has confirmed the suggestions of Gooley et al. [45]. Thus, the spectra have revealed the presence of an iron-nickel phase in meteorites, which have never been observed in terrestrial samples, and which has been produced in the laboratory exclusively by intense neutron or electron irradiation of iron-nickel alloys. This has been done in Grenoble by Néel et al. in 1962 [46].

They put in evidence the existence of an ordered $L1_0$ superstructure phase (Fe-Ni 50-50) in the Fe-Ni system. The order-disorder transition temperature of the ordered phase is 320°C [47,48]. This explains why it has not been possible to obtain this phase by annealing, since at this temperature the diffusion of metallic atom is practically stopped. To complete the entire equilibrium reaction, extremely slow cooling (4.6 billion years) is necessary due to the extremely slow Ni diffusion [2, 3, 6]. The formation process of the natural $L1_0$ -FeNi has been discussed by planetary scientists based on the metallurgy of the FeNi system [49,50].

As it was first shown by Néel et al. [51], the technique that allows a relatively easy identification of the ordered phase is the Mossbauer spectroscopy. The tetragonal distortion of the superstructure $L1_0$ has its origin in an electric field gradient at the level of the iron atoms of the alloy. This gives rise to Mossbauer spectra that is singular

within the Fe-Ni alloys, because it presents a typical asymmetry that results from a relatively small quadrupolar interaction superimposed to a large magnetic interaction of the ferromagnetic alloy. Since the "discovery" of the ordered Fe-Ni phase in meteorites many taenite lamellae have been investigated, and they have shown the presence of the same Fe-Ni phases [52]. However the hyperfine parameters of the ordered phase differ for lamellae from different meteorites. The ordered Fe-Ni 50-50 phase has been identified in many meteorites, as well in iron meteorites as in stony and stony-iron meteorites. This phase has been named Tetrataenite [2] due to the tetragonal structure and its close connection to taenite.

L₁₀-type ferromagnet has been of great promise as a material for magnetic memories or permanent magnets because of its strong magnetic anisotropy and large coercivity [15]. Meanwhile, typical L₁₀ phases such as CoPt or FePt have used large quantities of rare metals to obtain strong magnetic anisotropy. From the viewpoint of resource depletion and spiraling prices, there is a need for the introduction of a substitutable material. Here, we are looking into an L₁₀-type ordered alloy consisting of Fe and Ni, which are both abundant and inexpensive. L₁₀-FeNi is known to have high coercivity (500–4000 Oe) and magnetic anisotropy (1.3×10^7 erg cm⁻³), and its magnetic properties are comparable to those of CoPt [7,53]. Common disordered FeNi alloys, which usually have small coercivity and weak magnetic anisotropy, are classified as soft magnetic materials [10]. On the other hand, L₁₀-FeNi has high coercivity and strong magnetic anisotropy, and it is classified as a hard magnetic material; therefore, shedding light on this phenomenon is a matter of great interest in the field of magnetic materials science. As examples, we will just mention 3 stony meteorites from the more than 80 whose magnetic properties have been analyzed where considerable amounts of Tetrataenite were found. The name of the meteorites is the place where they were found. They are

Yaato-74160 and ALH-77260 with H_C (magnetic coercive force) = 255Oe and H_C = 185Oe respectively, T_C (Curie temperature) = 560°C and T_C = 580°C respectively, and natural remanent magnetization contains a hard component of more than 1/5 that cannot be demagnetized by an AF-demagnetizing field larger than 1000Oe peak. For St. Séverin meteorite, H_C = 500Oe and T_C = 550°C.

In a previous study on the synthesis of $L1_0$ -FeNi, it was reported by Néel et al in the 1960s that the $L1_0$ -FeNi ordered structure could be constructed by neutron irradiation at high temperature [7]. However, this approach is probably not an ideal choice for device applications. Recently, Shima et al demonstrated successful production of the synthesis of single-crystalline $L1_0$ -FeNi by alternate monatomic layer deposition using molecular beam epitaxy [22]. Kojima et al reported that, for alternate monatomically deposited FeNi, the magnetic anisotropy and degree of order are proportional, and they reported a magnetic anisotropy of 7.0×10^6 erg cm^{-3} with degree of order of 0.48 [25, 26, 54, 55]. Kotsugi et al analyzed the origin of the magnetic anisotropy of their sample using synchrotron radiation [56–59], and reported that the magnetic anisotropy arises from spin–orbit interaction in the 3d electrons of Fe [60]. Theoretical approaches were taken by Miura et al and Mitsumata et al, who reported on the relationship between magnetic anisotropy and lattice structure [61,62].

Chapter III

MATERIALS, SYNTHESIS OF SAMPLES AND CHARACTERIZATION TECHNIQUES

This chapter describes the materials used in the synthesis, the synthesis process of the nanoparticles and the techniques and equipments that were used in the different characterizations of the samples. Synthesis process was used to obtain the FeNi nanoparticles.

3.1 Materials

The following materials were used for the synthesis of the materials: ferric nitrate nonahydrate ($\text{Fe}(\text{NO}_3)_3 \cdot 9\text{H}_2\text{O}$), nickel nitrate hexahydrate ($\text{Ni}(\text{NO}_3)_2 \cdot 6\text{H}_2\text{O}$), ferrous chloride tetrahydrate ($\text{FeCl}_2 \cdot 4\text{H}_2\text{O}$), 1,2-hexadecanethiol, oleylamine, sodium oleate and oleic acid, were acquired from Sigma Aldrich. Ethanol, hexane (C_6H_{14}), 1-octadecene and ultrapure water were used as solvents.

3.2 Procedure of FeNi nanoparticles synthesis

The synthesis of the FeNi alloy was performed using a synthesis method with acquired practical-experimental domain being this the sol-gel method.

3.2.1 Modified sol-gel method

Samples were prepared by adapting a sol-gel method for the synthesis of $\alpha\text{-Fe}_2\text{O}_3$ sub-micron spheres, as described in the Ref. [65] and schematized in Figure 3.1 In a typical preparation, 7.1 g of ferric nitrate nonahydrate ($\text{Fe}(\text{NO}_3)_3 \cdot 9\text{H}_2\text{O}$) and 5.1 g of nickel nitrate hexahydrate ($\text{Ni}(\text{NO}_3)_2 \cdot 6\text{H}_2\text{O}$) ($\text{Fe}^{3+}:\text{Ni}^{2+}$ molar ratio = 1:1) are dissolved in 50 mL of ultrapure water to form the sol. Thus, 3.2 g of a colorless commercial gelatin was

used to jellify the medium and the system was maintained under magnetic stirring at 50°C until the evaporation of the residual water and the formation of the gel for approximately 5 hours. Subsequently, the resultant gel was dried for ~20 hours at 70°C in a muffle. The dried sample (as-prepared) was crushed and annealed in a tubular furnace under reducing atmosphere (hydrogen/argon mixture) during 4 hours. The annealing temperatures were 500°C (sample FeNi500), 600 °C (sample FeNi600), 700 °C (sample FeNi700), 800 °C (sample FeNi800), 900 °C (sample FeNi900) and 1000 °C (sample FeNi1000) and the heating rate was ~4.5°C/min. The reducing gas flow was maintained constant (~5 bubbles/min) for all synthesized samples. At the end of the process, the samples were cooled to room temperature in the reducing atmosphere. For the ordered synthesized samples, the value of S depends on the annealing temperature as shown in the schematic and it will be showed below.

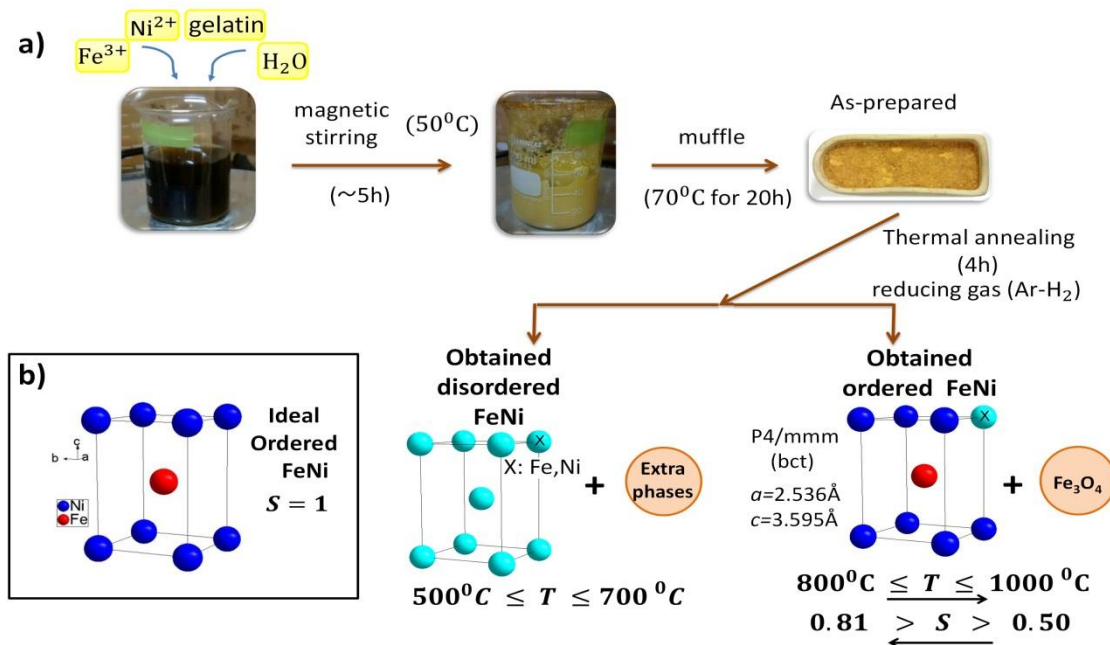


Figure 3.1 a) Schematic representation of the sol-gel method and specific annealing processes used to synthesize the ordered FeNi phase. Ordered phases are formed depending on the annealing temperature and the ordering parameter (S). b) Ideal atomic formation when S = 1.

3.3 Characterization techniques

3.3.1 X-ray diffraction

X-ray diffraction (XRD) was used to identify the crystal structure and other crystallographic parameters such as the parameters of the crystal lattice, mass composition of the components of the alloy, crystalline diameter, integrated intensity of the crystallographic peaks, etc. When electromagnetic waves of X rays strike on the crystalline plans of the sample, a diffraction of these rays takes place in all directions where only the constructive interferences governed by the Bragg condition form the diffraction peaks.

To calculate the mean particule size (crystallite) was used the formula of Scherrer [64] expressed as:

$$D = \frac{0.916\lambda}{\beta_{hkl} \cos \theta_{hkl}}$$

where, λ is the wavelenght of the radiation , β_{hkl} is the line width measured at half height and θ_{hkl} is Bragg's angle [29]. The line widths of the diffraction peaks were obtained from the quantitative analysis of the diffraction pattern made by the Rietveld method.

The structural properties have been determined using a conventional commercial diffractometer (Rigaku, Mini-Flex 600) with a Cu-K α radiation($\lambda = 1,5418\text{\AA}$). The diffractograms were recorded in the 2θ range from 20° to 90° and a step size of 0.01° .

The conventional XRD measurements were developed in the Laboratório de Nanotecnologia Verde da Faculdade de Ceilândia da UnB.

To examine the crystal structure with a high accuracy and determine the presence of the $L1_0$ -FeNi phase, we also used synchrotron x-ray diffraction (SXRD), since the synchrotron radiation based XRD has a high energy, high flux, and a sharp beam to

achieve signal-to-noise ratios much higher than conventional XRD. Then, we will be able to thoroughly investigate very weak diffraction peaks and so determine the presence of the Tetrataenite phase. The x-ray energy was set to 12 keV ($\lambda = 1,0333\text{\AA}$) and the scanning 2θ range was from 20° to 100° with a step size of 0.004° . The SXRD measurements were carried out in the Laboratorio Nacional de Luz Síncroton (LNLS) that is located in Campinas.

The diffraction patterns of the samples were compared with the standard database (JCPDS) and other accredited crystallographic sources. The integrated intensity of the peaks was calculated from the fitting made to the diffraction peak using a pseudo voigt function using the software Origin for that purpose.

3.3.2 Magnetic characterization

The magnetic characterization was carried out using a magnetometer of high sensitivity for magnetic detection. The basic functioning is based on the oscillatory movement to which the sample is subjected, producing a variation of the magnetic flux that is detected by the superconducting detection coils, generating a potential difference and inducing an electrical current in the coils. These coils are part of a superconducting quantum interference device that, through the quantification of the magnetic flux, measures the magnetic signal of the sample. The magnetic properties of the samples were measured using a SQUID type magnetometer, model MPMS3 (from Quantum Design, Inc. San Diego, CA). The ZFC and FC curves were measured at a temperature of 300K applying field of 20 Oe. The magnetization curves against the magnetic field were measured at temperatures of 5 and 380K. All measurements were made with powder samples. All the magnetic measurements were carried out in the Laboratório de

Síntese e Nanomateriais e Caracterização Magnética do NFA do Instituto de Física da Universidade de Brasília.

3.3.3 Transmission Electron Microscopy

Transmission electron microscopy (TEM) and high resolution was applied in order to obtain information on the morphology and particle size distribution, qualitative and quantitative chemical composition as well as structural information of our samples. To perform the histograms of size distribution of the nanoparticles, the images obtained by TEM and the Sturges method were used. The ImageJ 1.5 software was used to obtain the different particle sizes from images. The microscopic characterization of Fe-Ni nanoparticles was carried out using a high-resolution transmission electron microscopic (HR-TEM). The images were obtained using a commercial microscope (FEI Tecnai F30) operated at an acceleration voltage of 300 kV. Lattice fringes were determined from the fast-Fourier transform of the HRTEM images, using the Image J (version 1.5.0) software. The morphological analysis was performed using a scanning electron microscope (JEOL 7100F). Due to the high resolution of the images, interplanar distances were also calculated visually.

The measures were carried out in the Instituto de Nanociencia de Aragon de la Universidad de Zaragoza and in the Centro de Investigación Cooperativa en Biomateriales CIC biomaGUNE in Spain.

3.3.4 Fourier Transform Infrared absorption spectrometry

FT-IR (Fourier Transform Infrared) absorption spectrometry is widely used in organic synthesis. This method is based on determining the structures of molecules with the characteristic absorption of the molecules of infrared radiation, so that the infrared

spectrum is called of molecular vibrational spectrum. When exposed to infrared radiation, sample molecules selectively absorb radiation of specific wavelengths which causes the change of dipole moment of sample molecules. Consequently, the vibrational energy levels of sample molecules transfer from ground state to excited state. The frequency of the absorption peak is determined by the vibrational energy gap. The number of absorption peaks is related to the number of vibrational freedom of the molecule. The intensity of absorption peaks is related to the change of dipole moment and the possibility of the transition of energy levels. This technique was used in our samples to detect metal ions, oxides and remains of organic components, product of the synthesis. For this purpose, it was determined using a Fourier transform infrared (FT-IR) spectrometer (Bruker, VERTEX 70). These measurements were performed in the wavenumber interval of $4000 - 400 \text{ cm}^{-1}$ with a resolution of 0.4 cm^{-1} .

The measurements were carried out in the Laboratório de materiais semicondutores do CNANO do Instituto de Física.

3.3.5 Differential scanning calorimetry

Differential scanning calorimetry (DSC) is a thermo-analytical technique in which the difference in the amount of heat required to increase the temperature of a sample and reference are measured using a calorimeter as function of temperature as shown in Figure 3.2. Both the sample and reference are maintained at nearly the same temperature throughout the experiment. Generally, the temperature program for a DSC analysis is designed such that the sample holder temperature increases linearly as a function of time. Only a few mg of material are required to run the analysis. DSC is the most often used thermal analysis method, primarily because of its speed, simplicity, and availability. The utility of this technique was to calculate the temperature of

crystallization of the as-prepared sample synthesized after the annealing treatment in a reducing atmosphere. The samples with a mass of 4.7 mg was annealed at a rate of 10°C /min from 35°C to 600°C with nitrogen gas flux at a rate of 50ml / min. The DSC measurements were developed in the Laboratório de Nanotecnologia Verde da Faculdade de Ceilândia da UnB.

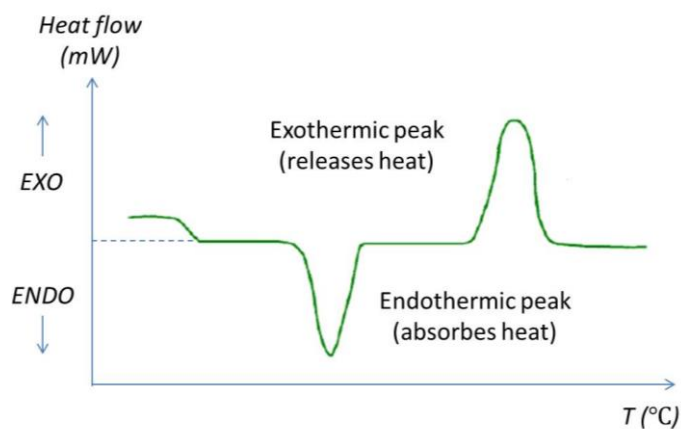


Figure 3.2 DSC curve showing endo and exothermic reactions.

3.3.6 Energy dispersive X-ray spectroscopy

Energy Dispersive X-ray Spectroscopy (EDS or EDX) is a qualitative and quantitative X-ray microanalytical technique that can provide information on the chemical composition of a sample for elements with atomic number (Z) greater than 3.

The X-rays are detected by an Energy Dispersive detector which displays the signal as a spectrum, or histogram, of intensity (number of X-rays or X-ray count rate) versus X-ray energy. The energies of the Characteristic X-rays allow the elements making up the sample to be identified, while the intensities of the Characteristic X-ray peaks allow the concentrations of the elements to be quantified. The spatial resolution of EDS analysis in the TEM is on the order of nanometers while the depth resolution is governed by the thickness of the sample. EDS is considered a non-destructive analytical

technique, that is, the sample can be re-analysed many times. This technique was used to calculate the percentages in mass of the components of our samples.

The EDS spectra were performed using a scanning electron microscope (JEOL 7100F) of the Laboratório da Faculdade da Engenharia Mecânica da Universidade de Brasília.

3.3.7 X-ray fluorescence spectrometry

X-ray fluorescence (XRF) spectrometry is an elemental analysis technique with broad application in science and industry. XRF is based on the principle that individual atoms, when excited by an external energy source, emit X-ray photons of a characteristic energy or wavelength. By counting the number of photons of each energy emitted from a sample, the elements present may be identified and quantitated. When an electron beam of high energy strikes a material, one of the results of the interaction is the emission of photons which have a broad continuum of energies. This radiation, called *bremstrahlung*, or “braking radiation”, is the result of the deceleration of the electrons inside the material. Another result of the interaction between the electron beam and the material is the ejection of photoelectrons from the inner shells of the atoms making up the material. These photoelectrons leave with a kinetic energy ($E - \phi$) which is the difference in energy between that of the incident particle (E) and the binding energy (ϕ) of the atomic electron. This ejected electron leaves a “hole” in the electronic structure of the atom, and after a brief period, the atomic electrons rearrange, with an electron from a higher energy shell filling the vacancy. By way of this relaxation the atom undergoes fluorescence, or the emission of an X-ray photon whose energy is equal to the difference in energies of the initial and final states. Detecting this photon and measuring its energy allows us to determine the element and specific electronic transition from which it originated. Herein lies the basis for XRF

spectrometry, where elements may be quantitated based on the rate of emission of their characteristic X-rays from a sample that is being excited.

To perform these measurements, a commercial spectrometer (Shimadzu EDX-720) of the Instituto de Química da Faculdade de Química da Universidade de Brasília was used. The results were used to quantify the elements present in our samples.

3.3.8 Mossbauer spectroscopy

The Mössbauer spectroscopy measurements were performed at the Laboratório de Mössbauer do Instituto de Física da Universidade de Brasília (UnB), which has the spectrometer for measurements at 77K and at room temperature. In Figure 3.3 is shown a small scheme of how the mosbbauer spectrum of a sample is formed.

The radioactive source of ^{57}Co is stuck to a rod and connected to a transducer that can perform periodic movements in the horizontal direction. This movement is controlled by a Mössbauer driving unit that transmits the information received from a function generator to the transducer (a triangular wave was used for this work). The periodic motion is an accelerated and linear movement with motion amplitude chosen according to the needs of the measurement of its sample. Observing a Mössbauer spectrum requires a comparison between the intensity transmitted through the absorber, inside and outside the resonance. To achieve this purpose, relative movement between the source and the absorber is required.

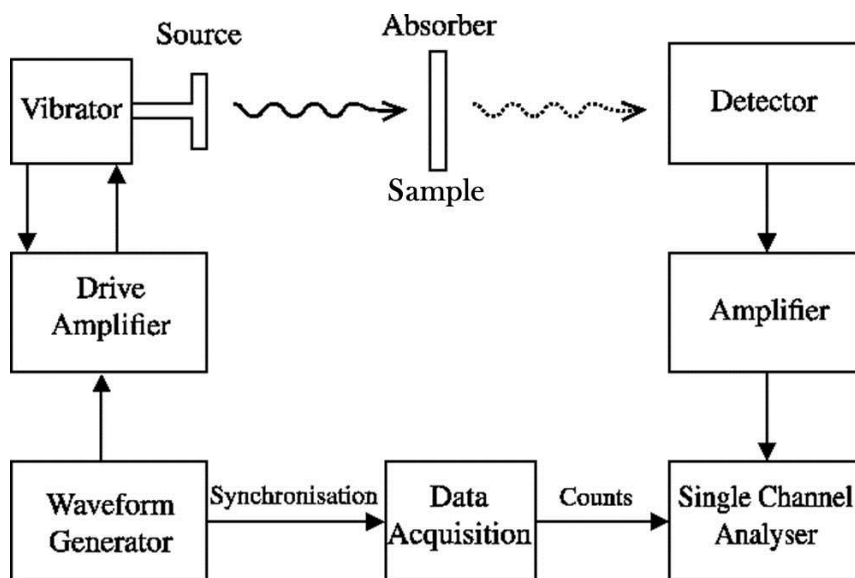


Figure 3.3 Schematic representation of a Mossbauer spectroscopy experiment.

One way is to move the radioactive source with constant acceleration in synchronization with scanning of the channels of a multichannel unit, so that each channel can be associated essentially with a speed. The absorber can be placed inside a cryostat or in a furnace to vary the temperature, since the temperature variation can influence the important physical processes, such as magnetic transitions, structural transitions, etc. The detection of the radiation, which is not absorbed by the sample, is detected with a proportional counter powered by a high voltage source of approximately 1.8 kV. The signal collected by the counter is taken to a preamplifier and then to an amplifier. The amplified total signal is discriminated at energies around 14.37 keV by means of a single-channel analyzer (SCA). The selected power window that is connected to the SCA analyzer is stored in 512 channels through the multichannel analyzer (MCA) board. The acquisition of the data is carried out via specific software. In the Mössbauer spectroscopy measurements, it is necessary to carry out a calibration measurement with a standard sample at room temperature. This sample consists of a very thin sheet of metallic iron whose hyperfine parameters are well known. This is done to determine the

maximum speed that is directly related to the value of the hyperfine magnetic field of the metallic iron.

3.3.9 X-ray photoelectron spectroscopy

X-ray photoelectron spectroscopy (XPS) is also known as ESCA (electron spectroscopy for chemical analysis) is a surface analysis technique which provides both elemental and chemical state information virtually without restriction on the type of material which can be analysed. The sample is illuminated with x-rays - monochromatic or unfiltered Al K α or Mg K α - and photoelectrons are emitted from the surface. The kinetic energy of these emitted electrons is characteristic of the element from which the photoelectron originated. The position and intensity of the peaks in an energy spectrum provide the desired chemical state and quantitative information.

The chemical state of an atom alters the binding energy (BE) of a photoelectron which results in a change in the measured kinetic energy (KE). The BE is related to the measured photoelectron KE by the simple equation; $BE = hv - KE$ where hv is the photon (x-ray) energy. The chemical or bonding information of the element is derived from these chemical shifts.

Chapter IV

RESULTS AND DISCUSSIONS

4.1 DETERMINATION OF THE L1₀-ORDERED PHASE IN FENI NANOPARTICLES

4.1.1 Chemical, structural and morphological properties

In order to identify and confirm the amount of Fe and Ni in all samples, the elemental composition of the samples were investigated by x-ray fluorescence and elemental mapping from EDS spectra experiments. In Table 4.1 are listed the values of the elemental compositions obtained from XRF and EDS measurements for all samples. The fluorescence spectra of the samples FeNi700 and FeNi800 are shown in the Figure 4.1. As observed, the chemical compositions of the Ni determined from XRF measurements in all samples are greater than 45wt.%, which is in a whole agreement with the range of values of the chemical composition to the stability domain of the L1₀-FeNi superstructure reported for natural meteorites[6,33,66].

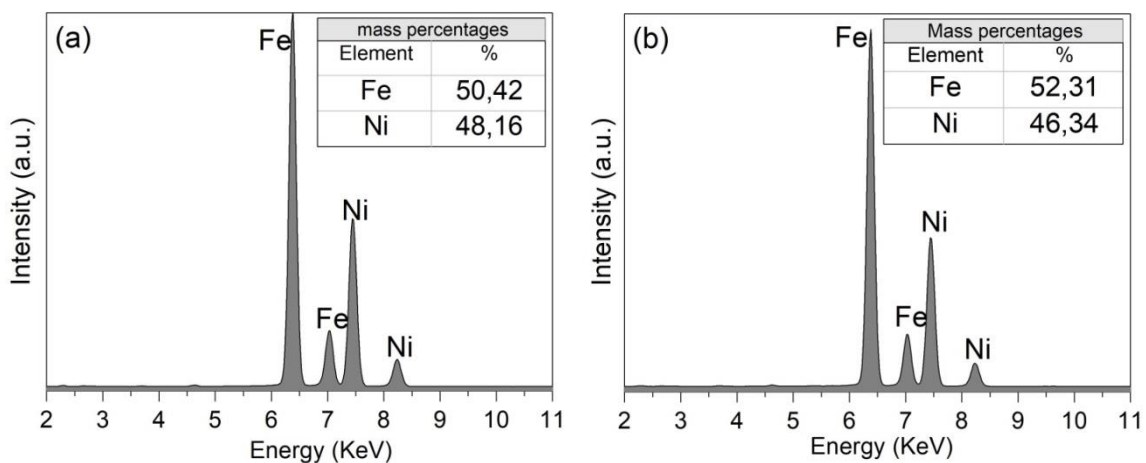


Figure 4.1 XRF measurements for a) FeNi700 and b) FeNi800 with their values of mass percentages for each of the compounds.

The difference between the results obtained by XRF and EDS observed in Table 4.1 is possibly due to the fact that in XRF usually a much larger irradiated surface area information on the sample is obtained at once than that in EDS and if the inhomogeneities are micro-ones, EDS will give quantitative differences of the amount of each compound of the sample in chosen discrete points. In Figure 4.2 are displayed the SEM images, the elemental mappings and the EDS spectra for the samples as-prepared (without annealing), FeNi900 and FeNi1000. In these spectra, the presence of various well-defined peaks of Fe and Ni was found, confirming the formation of these compounds. The mass percentages of elements of all samples are indicated in Table 4.1.

Table 4.1. Data of all samples referred to their quantitative chemical composition.

Sample	L1 ₀ -ordered FeNi phase	EDS		XRF	
		Fe (wt.%)	Ni (wt.%)	Fe (wt.%)	Ni (wt.%)
as-prepared	-	51.4	48.6	50.3	49.7
FeNi500	-	-	-	-	-
FeNi600	-	-	-	-	-
FeNi700	x	54.83	45.17	50.42	48.16
FeNi800	x	54.92	45.08	52.31	46.34
FeNi900	x	57.05	42.95	51.4	47.7
FeNi1000	x	55.93	44.07	50.3	48.9

To confirm the distribution of Fe and Ni onto the lattice surface, elemental mappings of SEM images were carried out (see Fig. 4.2), and the analysis showed that the Fe and Ni elements are homogeneously distributed in the whole material. Similar results were observed in the samples FeNi700 and FeNi800. These results are in agreement with SXRD measurements as will be discussed below. From these results, we can summarize that the stability domain of the ordered phase (according to the Ni concentration) was obtained for samples annealed from 700 °C to up 1000°C. Samples annealed at temperatures above 1000°C did not show the formation of the ordered phase. This was

corroborated by conventional XRD of the sample FeNi1150 (as shown below in Fig. 4.10). This suggests the thermal dependence of the ordered phase in the aforementioned temperature interval.

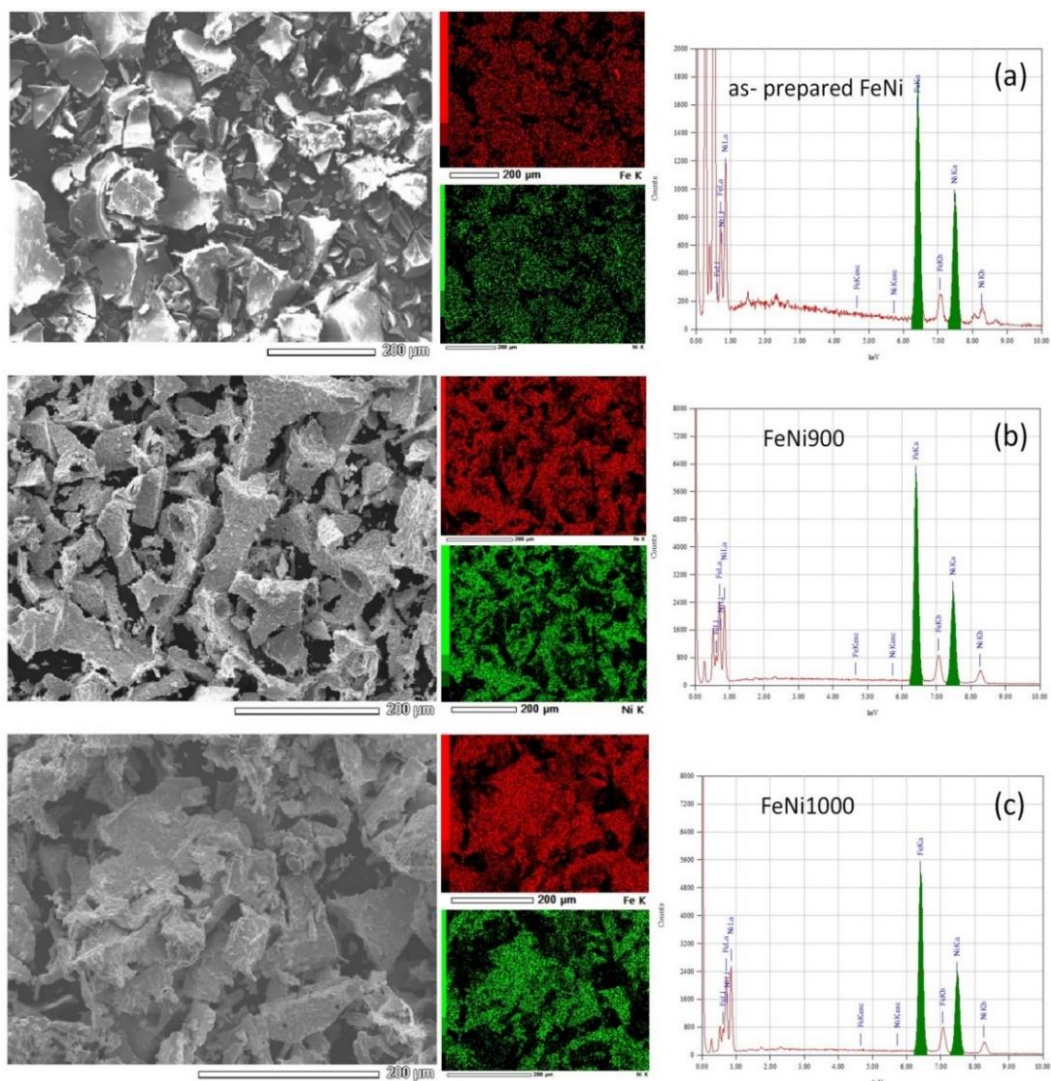


Figure 4.2 SEM images for samples a) as-prepared, b) FeNi900 and c) FeNi1000 each with their EDS element mappings and analysis, respectively. The presence of the components of Fe and Ni are represented in red and in green respectively.

The FT-IR spectra of the as-prepared sample and annealed samples at 600 °C, 700 °C, 800 °C and 1000 °C are shown in Fig. 4.3. A broadband at $\sim 3407\text{ cm}^{-1}$ and a band at $\sim 1633\text{ cm}^{-1}$ revealed the H-O-H stretching and an OH bending vibration of water, respectively [67,68], which were attributed to the atmospheric absorption of water. The amount of water in the as-prepared sample is visibly higher than in the other annealed

samples probably because the drying time (20h) in the muffle (see Fig. 3.1) was not sufficient to evaporate a greater amount of water residues in the as-prepared sample, product of the synthesis. The bands at $\sim 2960\text{ cm}^{-1}$ was assigned to CH_3 asymmetrical stretching and the bands at $\sim 2920\text{ cm}^{-1}$ together with bands at $\sim 2853\text{ cm}^{-1}$ were assigned to the stretching vibration of the CH_2 groups, attributed to the remaining organic components used during the synthesis process. The bands at $\sim 2426\text{ cm}^{-1}$, $\sim 2399\text{ cm}^{-1}$, $\sim 2349\text{ cm}^{-1}$ and $\sim 1384\text{ cm}^{-1}$ were assigned to the CO_2 absorbed from the atmosphere [67,69]. The stretching vibration peak attributed to the Fe–O bond is expected in the range $500\text{-}750\text{ cm}^{-1}$. For the as-prepared sample (without annealing), it was observed no peak in this region; then, the FT-IR results exclude the formation of oxide phases in the as-prepared sample. Therefore, we can conclude that the small amounts of oxide phase detected from XRD data analysis was formed during the annealing process at temperatures above 700°C , which accompanies the formation of the ordered phase (see Table 4.2). An interesting zone called the fingerprint region ($500\text{-}1500\text{ cm}^{-1}$) can provide important information about the FeNi phase formation.

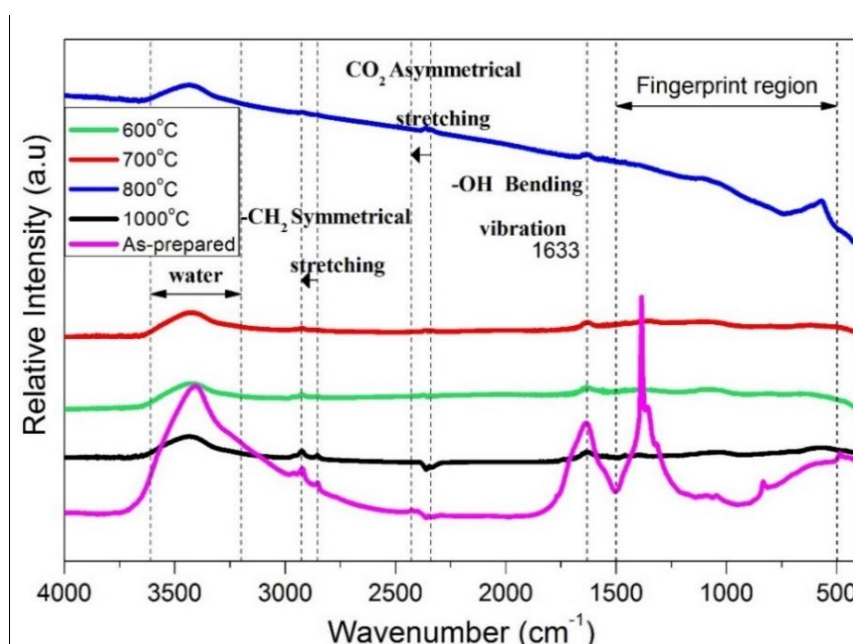


Figure 4.3 Fourier transform infrared spectra of the as prepared, FeNi600, FeNi700, FeNi800 and FeNi1000 samples.

If we compare the fingerprint regions of the as-prepared sample with the annealed ones (see Fig. 4.3), we can note different features, which suggest that the as-prepared sample does not show any vestiges of ordered or disordered FeNi phases. Similar FT-IR results were reported for disordered FeNi compound [70]. This result is in agreement with those obtained from XRD data analysis of the as-prepared sample (see Figure 4.4).

Table 4.2. Structural parameters obtained by the XRD data analysis for all samples. Long-range order parameter (*S*) and mean particle sizes determined from TEM images are also included.

Sample	Disordered FeNi phase		Ordered FeNi phase		Ordered FeNi phase by SXRD (wt.%)		Extras phases	<i>S</i> (± 0.1)	Size (nm) (± 0.5)	Poly-dispersity
	wt.%	Lattice parameters	wt.%	Lattice parameters	Fe	Ni				
As-prepared	-	-	-	-	-	-	-	-	-	-
500°C	86%	a = 2.537 c = 3.604	-	-	-	-	-Ni (12%); a = 3.526 -Fe _y (2%); a = 3.441	-	-	-
600°C	100%	a = 2.541 c = 3.574	-	-	-	-	-	-	7.3	0.35
700°C	100%	a = 2.544 c = 3.577	-	-	51.8	47.9	-	-	7.0	0.35
800°C	-	-	96% (100)	a = 2.536 c = 3.595	52.4	47.3	Fe ₃ O ₄ (4%); a = 8.389	0.81	11.4	0.32
900°C	-	-	97% (100)	a = 2.535 c = 3.588	52.4	47.3	Fe ₃ O ₄ (3%); a = 8.357	0.52	11.8	0.25
1000°C	-	-	84.5% (100)	a = 2.535 c = 3.588	50.7	49.2	-Fe ₃ O ₄ (6.5%); a = 8.394 -Fe ₂ O ₃ (9%); a = 5.035, c = 13.747	0.50	12.4	0.36

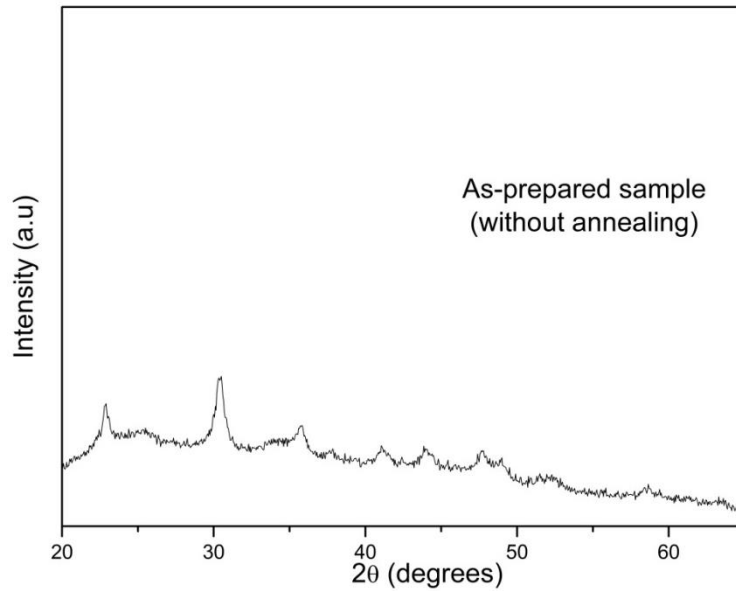


Figure 4.4 X-ray diffractogram of the as-prepared sample.

In order to assess to the $L1_0$ ordered FeNi phase (tetraetaenite) in our samples, firstly the conventional X-ray diffraction measurements were carried out.

In Figure 4.4 is shown the XRD lines of the as-prepared sample. The diffractogram was compared with the crystallographic source of the JCPDS and other reliable sources of softwares such as Search-Match, for instance. The identification of the peaks was not achieved. It is well know that the sol-gel method is used to produce Fe or Ni oxides where the formed gel in this synthesis goes through a calcination process between temperatures ranging from 400°C to 600°C [27,71-73] to obtain a crystalline phase (Fe_2O_3 and NiO for instance). In the case of our as-prepared sample, it was not annealed and was just dried at 70°C in a muffle for 20 hours (see Figure 3.1). We think that this drying process started a very short-range incomplete crystallization. Therefore, those few peaks observed in this diffractogram are not characteristic of some crystalline phase but of an amorphous phase.

The as-prepared sample was subjected to annealing treatments at temperatures of 300°C, 400°C, 500°C and 600°C in a reducing atmosphere. The diffractograms of each

of the samples are shown in Figure 4.5. Using the Rietveld method, the weight percentage of the disordered FeNi alloy was calculated in each of the samples.

It is observed that the amount of the disordered phase of FeNi is greater in the samples, as the treatment temperature is increased. The formation of a pure phase of the disordered FeNi alloy is given at 600°C. It is worth mentioning the crystallographic process followed depending on the annealing temperature. From an amorphous phase of FeNi without annealing treatment, passing through of the formation of the disordered phase of FeNi with impure phases in the range of annealing temperature between 300°C and 600°C and achieving the formation of the ordered phase of FeNi for annealing temperatures between 700°C and 1000°C. This will be shown and discussed in the following lines.

In Figure 4.6 is shown the XRD pattern of the sample FeNi900. Herein, the peak positions (represented by small vertical solid lines) correspond to the Bragg reflections of the ordered FeNi phase and some other peaks to a secondary phase identified as the magnetite. The Rietveld analysis of the XRD pattern was carried out confirming the presence of the two phases. A detailed analysis of the XRD pattern reveals the presence of superstructure reflections which is evidence for the orderig and is ascribed to the ordered L1₀-phase of FeNi as depicted in the inset of Figure 4.6 The lattice parameters of L1₀-FeNi were estimated as $a = 2.535 \text{ \AA}$ and $c = 3.588 \text{ \AA}$ in agreement with those reported in the literature for this ordered FeNi phase [2] as shown in Table 4.2.

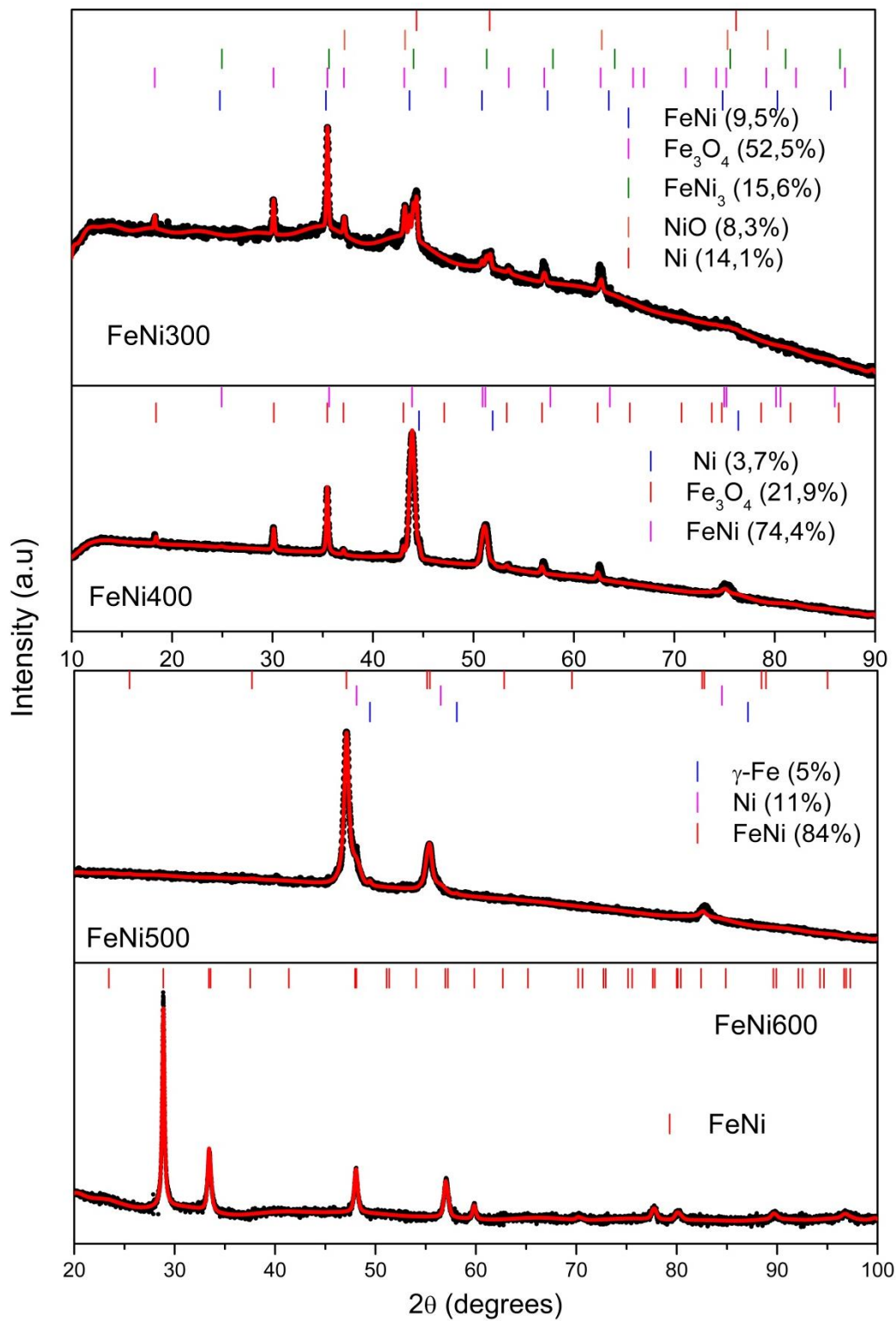


Figure 4.5 Conventional XRD patterns of the samples FeNi300, FeNi400 and FeNi500. SXRD pattern of the sample FeNi600. Crystallographic evolution with the annealing temperature of the disordered FeNi alloy.

The superposition of the (100) superstructure peak (located at $2\theta \sim 35.6^\circ$) and the (311) reflection peak of magnetite phase (at $2\theta \sim 35.8^\circ$) is observed in the inset of Figure 4.6. It is interesting to mention that the intensity of the (100) superlattice reflection is very weak, which is due to the very small difference between the atomic scattering factors of Fe and Ni. This is the reason why the peak intensity of the (311) reflection of magnetite is much more intense than the peak intensity of the (100) superlattice reflection. As shown, the (100) superlattice peak is clearly observed, confirming the $L1_0$ -FeNi phase. The fact that the presence of both phases can be determined using conventional XRD measurements reflects the good crystallinity of our sample.

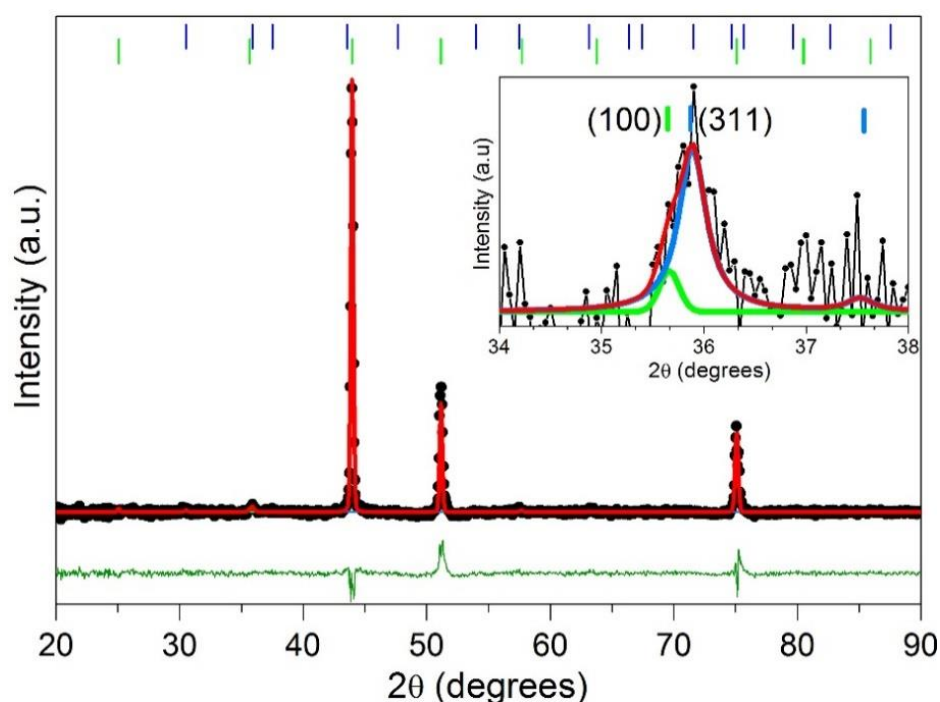


Figure 4.6 Conventional XRD pattern of sample FeNi900. The inset is a magnified graph in the region corresponding to the (100) superstructure peak (green solid line). Blue solid line represents Magnetite peak and red solid line represents the superposition of both peaks.

On the other hand, Figures 4.7 and 4.8 show the synchrotron radiation X-ray diffraction (SXRD) patterns obtained for samples FeNi700 and FeNi800, respectively. As observed, the pattern of sample FeNi700 is consistent with the disordered phase (body-

centered tetragonal, bct). The Rietveld refinement of the SXRD pattern provides lattice parameters a and c with values of 2.544 and 3.577Å, respectively.

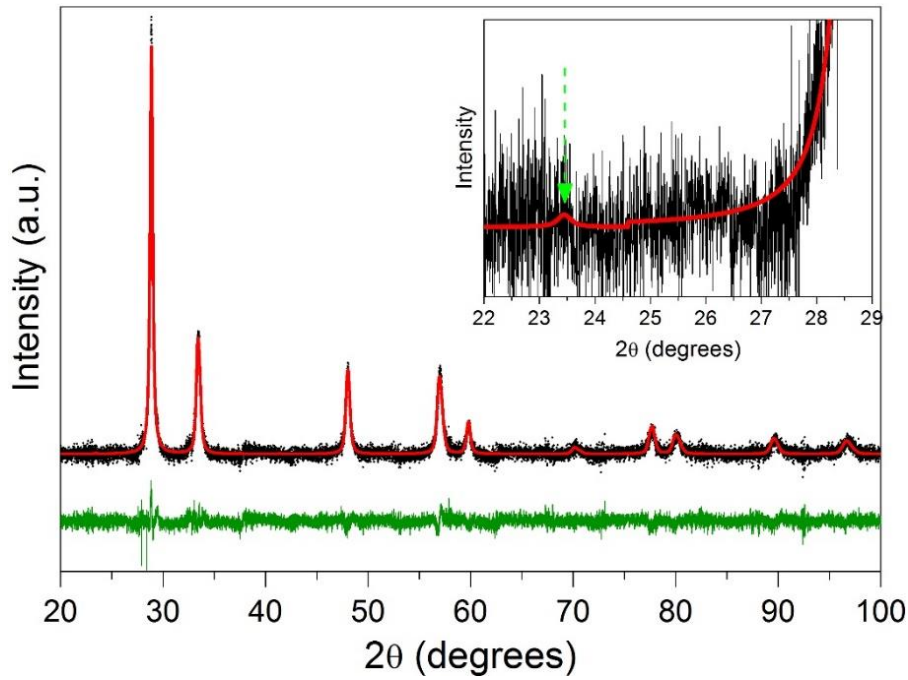


Figure 4.7 SXRD pattern of sample FeNi700. The inset is a magnified graph in the region corresponding to the possible (100) superstructure peak. This peak is indicated with a light green arrow.

The percentage of each metallic component is estimated as 47.9% (Ni) and 51.8% (Fe). Those percentages of metallic components are in agreement with those percentages found from XRF data for all samples. The percentages of the metallic components obtained from the structural data analysis for the studied samples are listed in Table 4.2. No evidence for the presence of superstructure reflections of the the $L1_0$ ordered phase was determined for this sample as depicted in the inset of Figure 4.7, in agreement with results obtained from conventional XRD data analysis.

However, a different result was determined for the sample FeNi800 as shown in Figure 4.8. According to the extinction rule, the (100) reflection is only originated from the ordered $L1_0$ phase of FeNi [24]. As observed in the inset of Figure 4.8, this (100) superstructure reflection is clearly resolved in the SXRD pattern of sample FeNi800.

The data analysis provides super lattice parameters of $a=2.536\text{\AA}$ and $c=3.595\text{\AA}$ for sample FeNi800, and similar super lattice parameters were determined for samples FeNi900 and FeNi1000, as listed in Table 4.2.

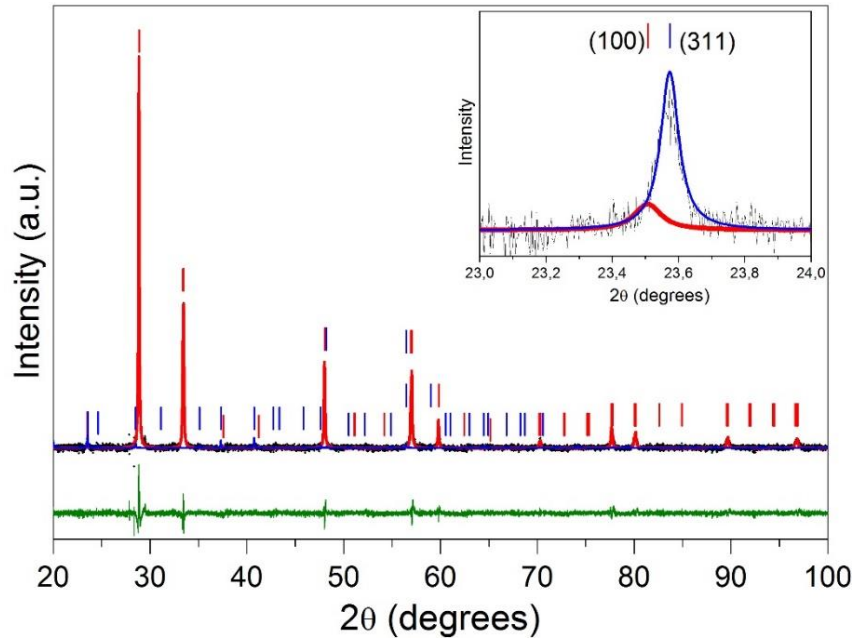


Figure 4.8 SXR D pattern of sample FeNi800. The inset is a magnified graph from 23 to 24 degrees showing the (100) superstructure diffraction (red line) and the (311) reflection of magnetite (blue line).

Those lattice parameters are in good agreement with the values reported for a natural meteorite [2]. From the Rietveld refinement analysis, the percentage of each metallic component is estimated as 47.4% (Ni) and 52.6% (Fe) for sample FeNi800. Those percentages of metallic components are in agreement with those percentages found from XRF data for all samples. Also, the values that we found are in good agreement with the range of values reported in the literature for the stability domain of the $L1_0$ -FeNi superstructure [6,33,66].

In Figure 4.9 is displayed the SXR D pattern of sample FeNi1000 where in the inset of this Figure is depicted the fitting for this region of the diffractogram formed for three peaks that represent to $L1_0$ -FeNi (100), magnetite (311) and hematite (110) phases with

mass percentages listed in Table 4.2. This notoriously observed superstructure line of the L1₀-FeNi phase reconfirms the similar favorable results obtained in the samples with presence of this ordered phase.

We also detected the presence of magnetite (Fe₃O₄) in a very small amount (3-6.5%) together with the formation of L1₀-FeNi phase in all samples. Reports in the literature of the L1₀-FeNi phase synthesized in laboratory [20-22,24,25,27,74] and in meteorites [75] indicated the presence of small amounts of Fe₃O₄ but not detailed analysis was carried out, perhaps related to the superposition of the main peaks of both phases (the (100) of L1₀-FeNi and (311) of Fe₃O₄).

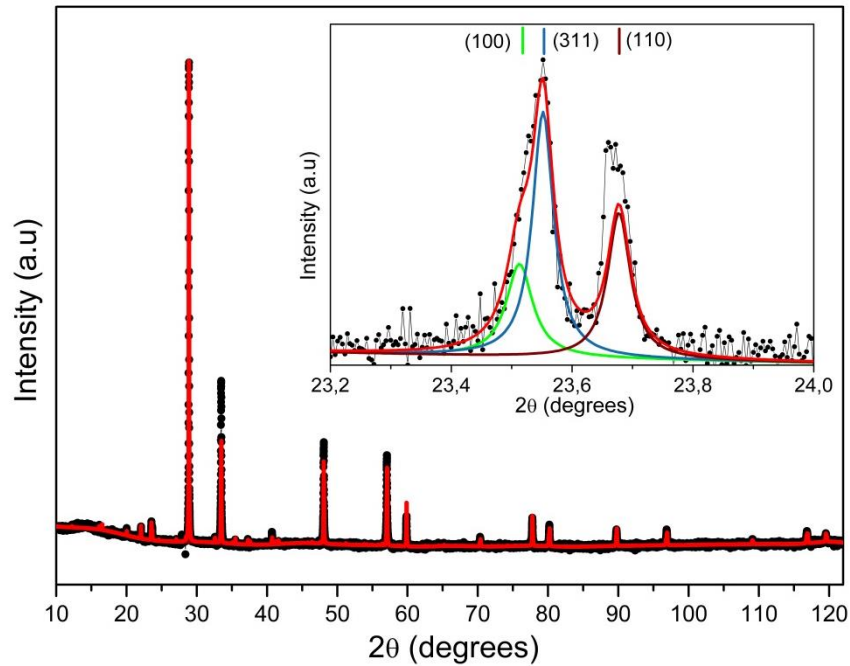


Figure 4.9 SXR D pattern of sample FeNi1000. The inset is a magnified graph in the region corresponding to the (100) superstructure peak (green solid line). Blue and brown solid lines represent magnetite (311) and hematite (110) peaks respectively. Red solid line represents the superposition of the three peaks.

The diffractogram of the sample FeNi1150 is shown in Figure 4.10a. The diffraction pattern was adjusted with the ordered FeNi (98 wt%) and with magnetite (2 wt%) phases. The superstructure peak (100) was not found for the FeNi alloy (see Fig 4.10b). However, at position $2\theta = 57.64^\circ$, the superstructure peak (111) of the ordered phase FeNi (see Table 2.1) is observed (see Fig 4.10c). The observed intensity in this position

indicates the existence of another phase due to the weak intensity of a superstructure peak. This other phase was not possible to identify, so we do not have the certainty if the observed intensity can only be of this unknown phase or if it can be deconvoluted in 2 peaks belonging to this unknown phase and to the ordered phase Unlike the clear demonstration of the co-existence of the superstructure line (100) and the magnetite line (311), we can not corroborate the presence of the ordered phase in this sample, for the non-recognition of a phase. Due to the measurement resolution of a conventional x-ray diffractometer, it was not possible to determinate clearly the difference between the adjustment with the Fe₃O₄ and NiFe₂O₄ phases. Therefore, a clear presence of the magnetite and the ordered phase can not be confirmed in this sample, but of being a disordered FeNi phase for these evidences.

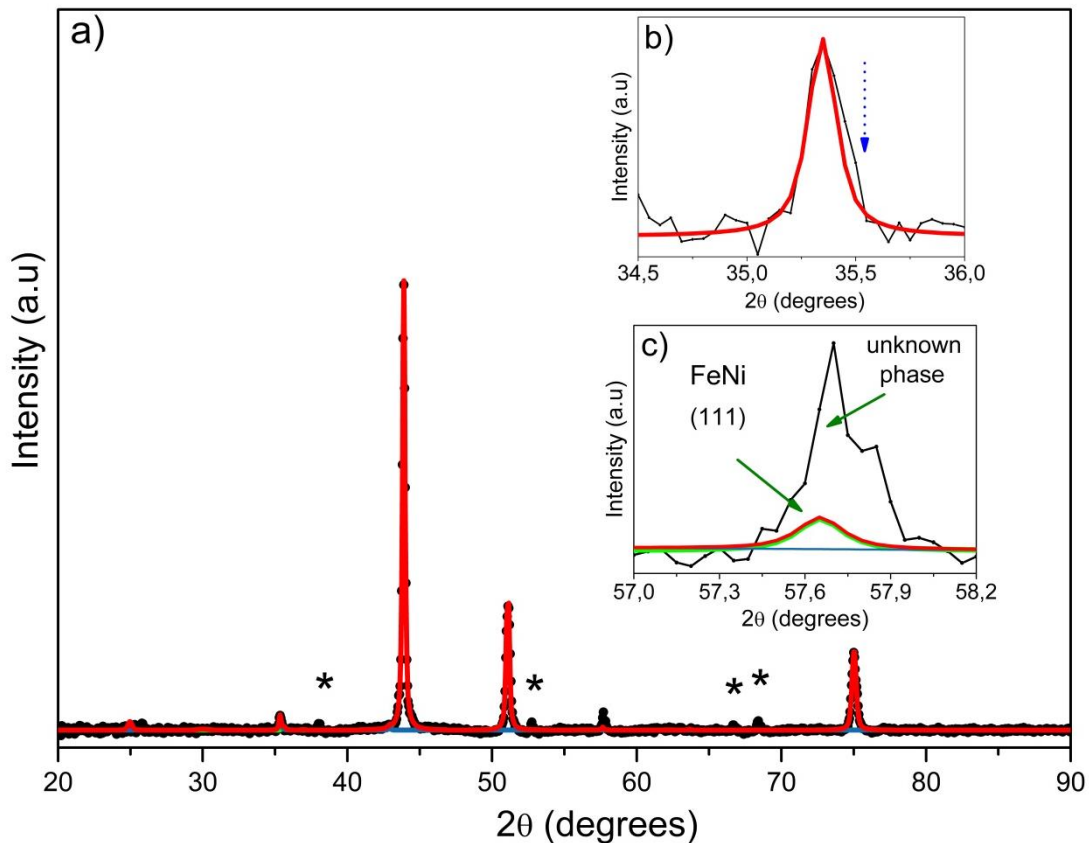


Figure 4.10 a) XRD pattern of the sample FeNi150 where the asterisks above each peak indicate those that were not identified. b) The blue arrow indicates the position of a possible superstructure peak (100). c) The peak of the unknown phase and a possible superstructure peak (111) of FeNi alloy are shown.

As already mentioned, clear evidences of the formation of the ordered L1₀-FeNi phase were achieved between annealing temperatures of 700°C and 1000°C.

In order to estimate the long-range order parameter (S), we used the integrated peak area of the (200) fundamental and (100) superstructure peaks. According to the

literature [28], the S is given by $S = \sqrt{\frac{[I_S/I_f]^{obs}}{[I_S/I_f]_{S=1}^{calc}}}$, where, I_S and I_f are peak intensities of

the superlattice and the fundamental peaks, respectively, and superscripts of *obs* and *calc* indicate experimentally observed values and theoretically calculated values. The estimated values are listed in Table 4.1. As observed, the value of S is larger for the sample annealed at T = 800°C and it decreases for larger annealing temperatures. It is worth mentioning that the obtained S-values are larger than that reported in the literature for synthesized L1₀-FeNi (S = 0.48, 0.71) [28,76], and for natural meteorites (S = 0.608)[76].

As example, we are going to calculate S for the sample FeNi900. For this purpose, we have to find out the theoretical intensities of the superlattice and the fundamental peaks. From equation (2.10), the structure factor (F), the multiplicity factor (p) and the Bragg angle (θ) are needed for this.

✓ **Fundamental peak (200)**

From equation (2.8), we calculate F^2 :

$$F^2 = 4[(x_B(f_0 + f')_B + x_A(f_0 + f')_A)^2 + (x_B f''_B + x_A f''_A)^2] \quad (4.1)$$

where : $A = Ni$; $B = Fe$; $x_{Fe} = 0.524$; $x_{Ni} = 0.472$; $\theta = 37.56^\circ$

For $\theta = 37.56^\circ$:

$$\begin{aligned} f_{Fe} &= 13.95 - 1.12 + i3.15 \\ f_{Ni} &= 15.68 - 3.02 + i0.51 \end{aligned}$$

Substituting all these data in equation (4.1), we have:

$$F^2 = 679.94$$

Finally, in equation (2.10), and knowing that $p = 4$, we calculated:

$$I_{200}^{cal} = 9852,191 \quad (4.2)$$

✓ *Superlattice peak*

From equation (2.9) and considering $S=1$, we calculate F^2 :

$$F^2 = [(f_0 + f')_A - (f_0 + f')_B]^2 + [f''_A - f''_B]^2 \quad (4.3)$$

For $\theta = 17.83^\circ$:

$$\begin{aligned} f_{Fe} &= 20.07 - 1.12 + i3.15 \\ f_{Ni} &= 22.17 - 3.02 + i0.51 \end{aligned}$$

Substituting these values in equation (4.3), we have:

$$F^2 = 7.012$$

In equation (2.10), and knowing that $p = 4$, we calculated:

$$I_{100}^{cal} = 523,142 \quad (4.4)$$

The observed intensities were calculated by fitting of the experimental diffraction peaks with a pseudo voigt function using the Origin software. The obtained values were:

$$I_{100}^{obs} = 13.024 \quad \text{and} \quad I_{200}^{obs} = 933.304 \quad (4.5)$$

Now, we will use the equation (2.11) with all the values found in the equations (4.2), (4.4) and (4.5), resulting that:

$$S = \sqrt{\frac{13.024/933.304}{523.142/9852,191}}$$

$$S = 0.52$$

As shown in Table 4.2, for annealing temperatures less than 700⁰C and larger than 1000⁰C, the magnetite and ordered FeNi phase were not observed, but different ones were found. This suggests that, unlike the ordered phase of natural [6] or artificial FeNi [28,76], our FeNi samples shows a larger disorder-order transition temperature (above 700 C), via the chemical method used to synthesize them. Besides, our results indicate that the parameter of atomic order (S) decreases with the increase of the annealing temperature as shown in Table 4.2. This high temperature value for the order-disorder transition has never been reported in the literature, according to our good knowledge. This is a very encouraging result in comparison to the disorder-order transition temperature for natural Tetrataenite (around 320⁰C). It means, the diffusion process of Fe and Ni atoms has been accelerated to obtain much faster the ordered phase.

In order to obtain detailed information on the crystallinity and morphology of the samples, SEM and TEM measurements were carried out. The TEM images of samples FeNi700 and FeNi800 are shown in Figure 4.11. As observed, most of the nanoparticles show circular and ellipse shapes.

In order to determine the mean particle size, we count a large number of particles sizes (N~842 and 983 for samples FeNi700 and FeNi800, respectively.) and a histogram were mounted following the Sturges criteria [77] (see Figure 4.11). The histogram distribution were modeled using the lognormal function:

$f(D) = 1/\sqrt{2\pi}\sigma D \exp \left[-\ln^2 \left(\frac{D}{D_0} \right) / 2\sigma^2 \right]$, where D_0 is the median size of the distribution and σ represents the polydispersity index.

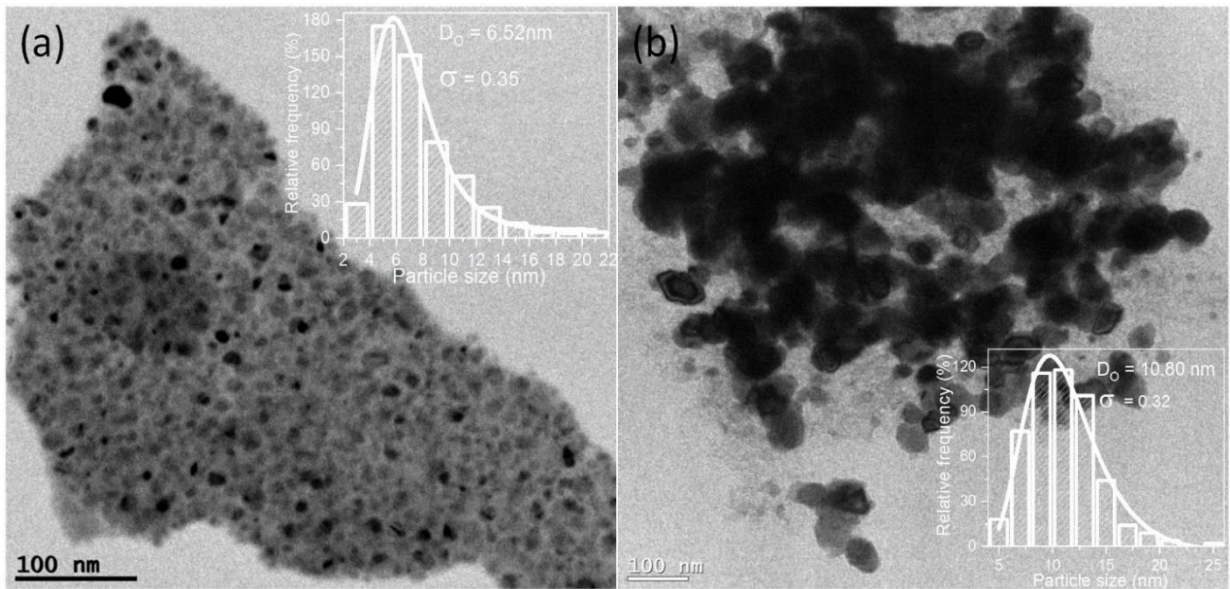


Figure 4.11 TEM images of nanoparticles of a) FeNi700 and b) FeNi800. In the inset of each image, it is shown the histogram of particle size mounted as described in the text.

The mean size is given by: $\langle D \rangle = D_o \exp(\sigma^2/2)$. The data analysis provides a mean particle size of ~ 7.0 nm and ~ 11.4 nm for samples FeNi700 and FeNi800, respectively. As observed in Table 4.2, the mean particle size becomes larger for larger annealing temperatures. This increasing tendency with the annealing temperature is assigned to the ratio between the surface and volume of the smallest particles. Because its surface area is much larger than its volume, it can absorb more heat much faster than larger particles. Because of this, the smaller particles will be melted and will join the larger particles. The larger crystals grow larger at the expense of the small crystals getting smaller or disappearing them.

High-resolution TEM (HRTEM) images were obtained for the set of samples. In spite of not having detected the presences of the ordered phase nor of the magnetite in the FeNi700 sample through SXRD measurements, the results were different with HRTEM images. HRTEM image of sample FeNi700 is shown in Figure 4.12a with 3 polygonal regions inside of this (Figs. 4.12b, 4.12c and 4.12d). In Figure 4.12e is shown the pattern after Fourier transform of Fig. 4.12b. The intensity spots of the $L1_0$ -FeNi superstructure corresponding to (1 0 0) and (1 0 1) planes related with interplanar

distances of 2.53 Å and 2.06 Å in the same order. According to the literature, the formation of the ordered FeNi phase was confirmed via electron diffraction patterns or Fourier transform, but in some cases it was not corroborated by XRD data analysis [78].

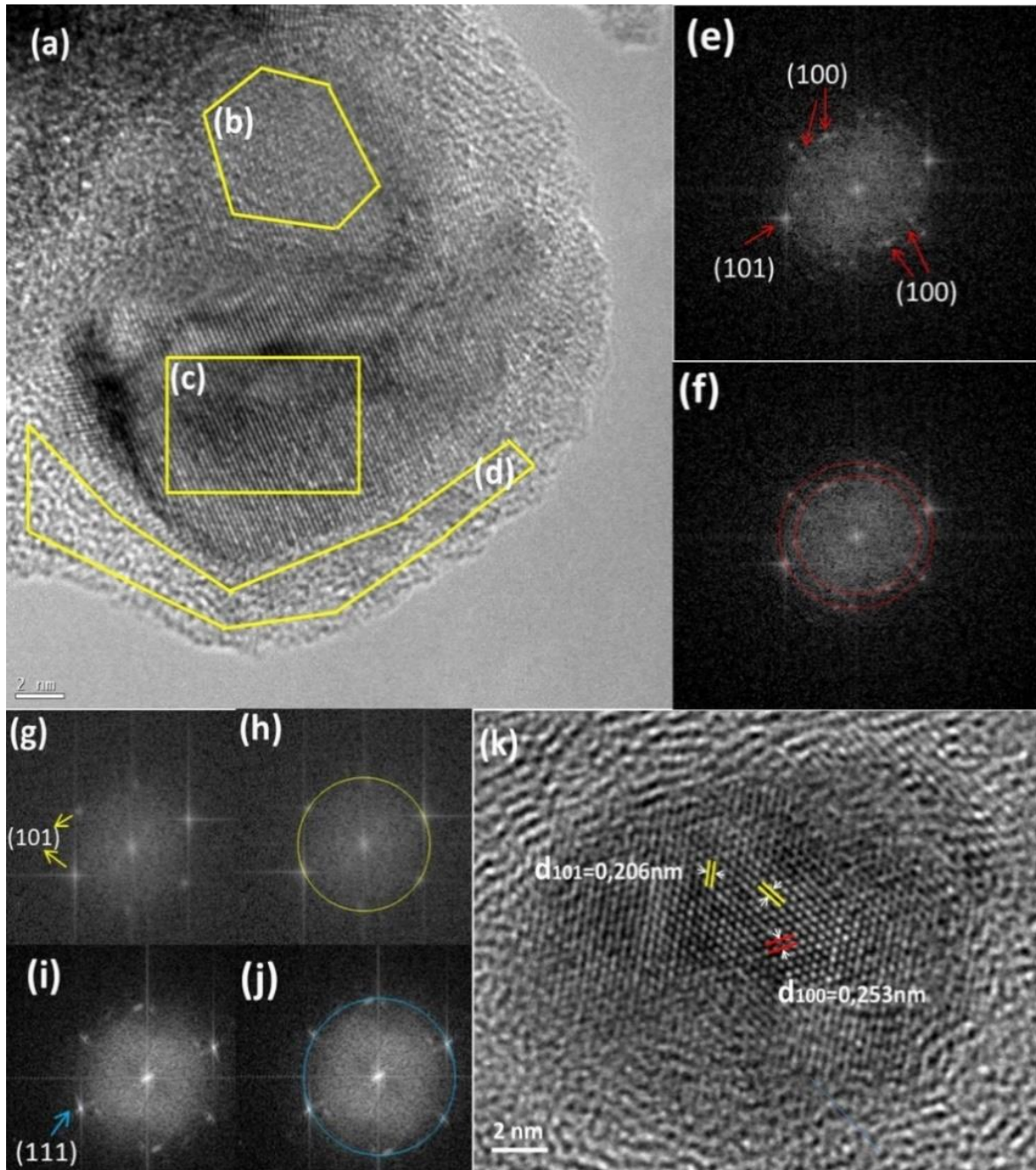


Figure 4.12 High-resolution image of FeNi700 nanopowder sample after synthesis process and annealing: a) lattice image; b)-d) regions used for Fourier transform; e),g) and i) patterns after Fourier transform of areas b)-d) respectively; f) Halo rings belonging to L1₀-FeNi (100) phase (red); h) Halo ring belonging to disordered FeNi (101) phase (yellow); j) Halo ring belonging to metallic Ni (111) phase (light blue); k) HRTEM image showing the (100)-(101) interplanar distances belong to L1₀-FeNi phase.

As shown in Figures 4.12g and 4.12i (patterns after Fourier transform of Figs. 4.12c and 4.12d), some spots are observed which indicate the presence of disordered FeNi and metallic Ni, respectively. The interplanar distances of 2.07 Å (101) and 2.04 Å (111) were determined for those latter phases. In Figure 4.12k is shown the HRTEM image showing the lattice spacing of 0.253 nm which corresponds to the (100) plane of the ordered phase and the lattice spacing of 0.206 nm related to the (101) plane of the fundamental FeNi lattice, where they can be clearly observed. Thus, the HRTEM observations confirm the existence of the L1₀-FeNi superstructure for the sample FeNi700.

In Figure 4.13a is shown the HRTEM image for sample FeNi800. In Figure 4.13d is displayed the intensity spots related to the L1₀-FeNi superstructure and Fe₃O₄ phases which are very clearly visible and they are related to the interplanar spacings of 2.53 Å and 2.06 Å for L1₀-FeNi and 2.52, 2.96 and 4.73 Å for Fe₃O₄. Such interplanar spacings are consistent with that of (1 0 0) and (1 0 1) planes of L1₀-FeNi phase and (3 1 1), (2 2 0) and (1 1 1) planes of Fe₃O₄ phase [79] determined from XRD data analysis. These results confirm the formation of the superstructure FeNi phase and the presence of magnetite phase in this sample. It is worth noting the non-superposition of (100) ring lattice of the L1₀-FeNi phase and (311) ring lattice of the Fe₃O₄ phase (see Fig. 4.13e), which is in excellent agreement with that reported for FeNi in natural meteorite by J. Zhang et al. [75]

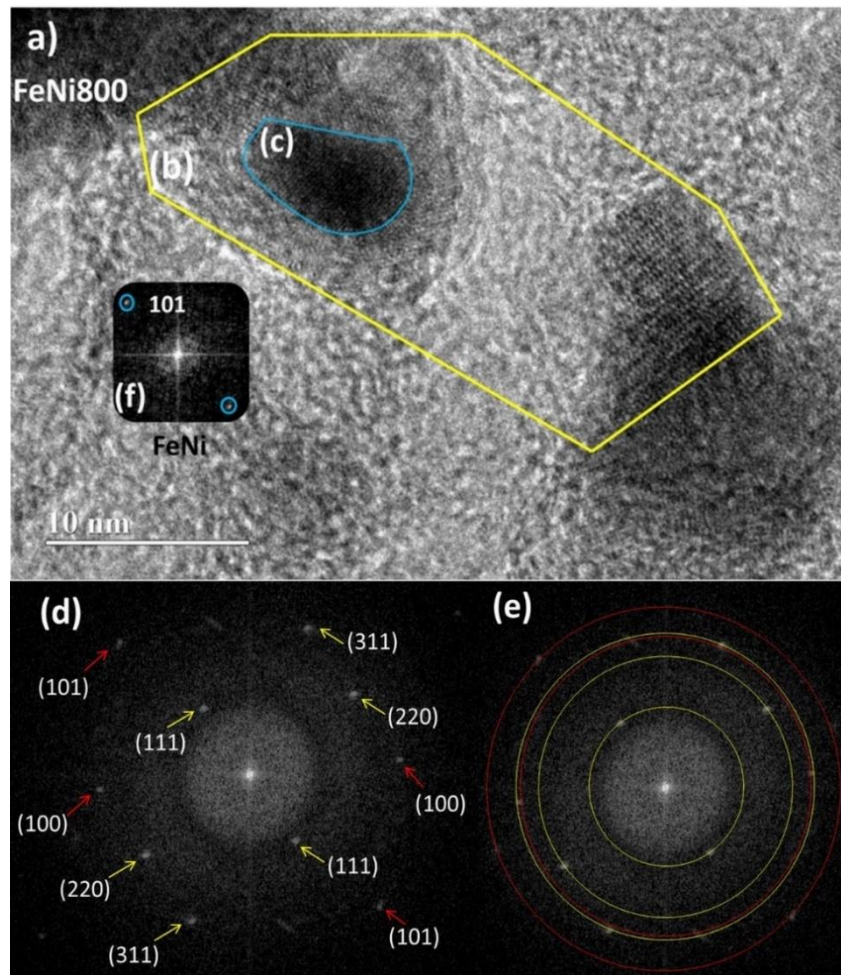


Figure 4.13 High-resolution image of FeNi800 nanopowder sample after synthesis process and annealing: a) lattice image, b) and c) regions used for Fourier transform, d) pattern after Fourier transform of area b), e) Halo rings belonging to $L1_0$ -FeNi (100) phase (red) and to Fe_3O_4 phase (yellow), f) pattern after Fourier transform of area c).

Additional information was found in most of the darker regions of the TEM images of the samples. The concentration of Fe and Ni components is slightly different from the ideal value (50%). This result was obtained via EDS measurements, placing the spot of measurement in the darkest areas. For example, applying the Fourier transform in the region shown in Fig. 4.13c, intensity spots (see Fig. 4.13f) were obtained that belong to the disordered phase (101) of FeNi, which reinforces the idea of being able to relate the darker regions with the non-stoichiometric composition of Fe and Ni.

In order to clarify any doubts regarding the formation of the ordered phase, in Figure 4.14c is shown the Fourier transform pattern of sample FeNi1000 obtained from the

chosen region in Figure 4.14b. As observed, similar features determined for samples FeNi700 and FeNi800 were found.

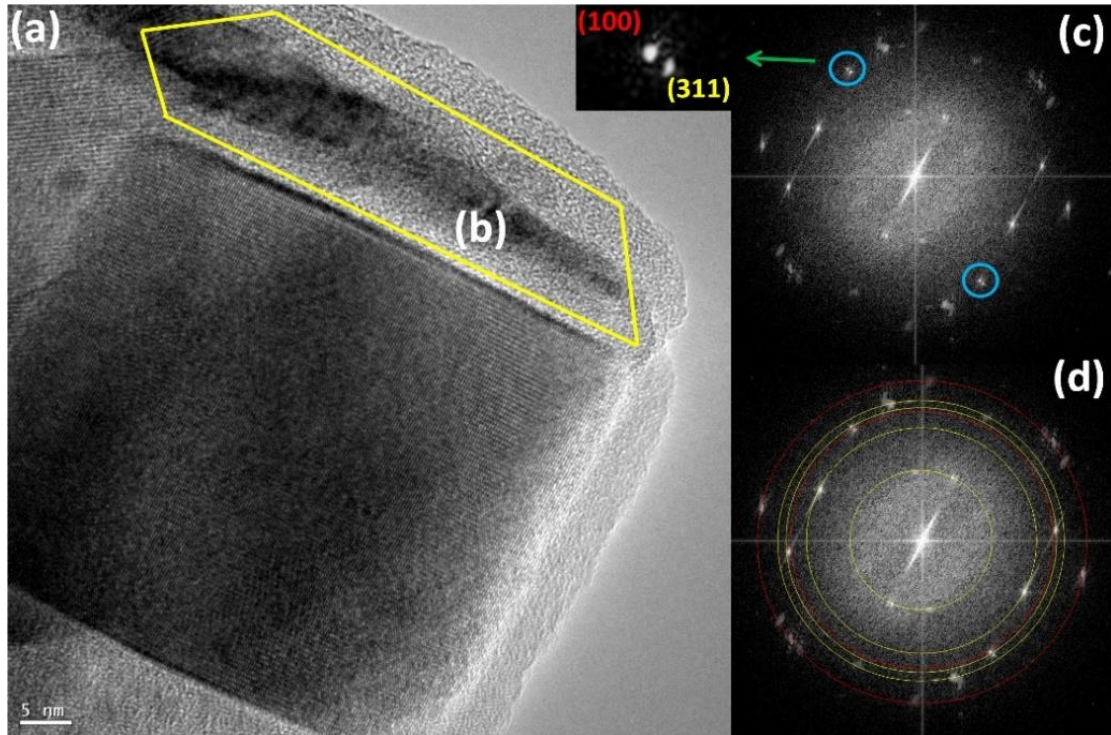


Figure 4.14 High-resolution image of sample FeNi1000: a) lattice image. b) region used for the Fourier transform. c) pattern after the Fourier transform of the selected region. In the inset is shown the amplified image of the two spots (encircled in blue) belonging to L1₀-FeNi (100) phase (in red) and magnetite (311) phase (in yellow) d) All the Halo rings belonging to L1₀-FeNi phase (red) and magnetite phase (yellow). The orientations of the planes starting from the innermost ring to the outermost ring for each phase: (100) and (101) planes of Tetrataenite phase and (111), (220), (311) and (222) planes of magnetite phase.

Moreover, as shown in the inset of Figure 4.14c, it is notoriously observed the non-superposition of the intensity spots belonging to the (1 0 0) plane of L1₀-ordered FeNi phase and (3 1 1) plane of Fe₃O₄ phase, which clearly proves the coexistence and identification of both crystalline phases (see Figure 4.14d). This strong evidence confirms the results obtained from SXRD data analysis about the coexistence of L1₀-ordered FeNi and Fe₃O₄ phases. This phase coexistence is consistent with reports in the literature for synthesized samples [81,78] and meteorites[80,75].

Moreover, X-ray photoelectron spectroscopy (XPS) technique was used to confirm the surface composition of the nanoparticles. From XPS survey spectra obtained for the samples of FeNi700, FeNi800 and FeNi900 were extracted the core level XPS spectra of Fe2p and Ni2p. All spectra were calibrated with O 1s and C 1s regions. The core level XPS spectrum of Fe2p for the sample FeNi700 is shown in Figure 4.15a. It was determined a peak located at 711.06 eV with its satellite peak at 713.34 eV. This peak is assigned to the Fe⁺³. The core level of Ni2p shows peaks located at 852.76 eV and 856.05 eV with a satellite peak at 861.63 eV as shown in Figure 4.15b. Those peaks were attributed to metallic Ni and Ni²⁺, respectively, on the surface of the nanoparticles in sample FeNi700. The presence of metallic Ni was confirmed by the analysis of the HRTEM images (see Figs.4.12i and 4.12j) for this sample.

Figure 4.15c is shown the core level XPS spectrum of Fe2p for the sample FeNi800. The peaks located at 710.5 eV and 724 eV were assigned to the Fe2p_{3/2} and Fe2p_{1/2}, respectively. A more detailed analysis indicates that the Fe2p_{3/2} peak can be deconvoluted into two peaks centered at 710.06 eV and 711.97 eV with satellite peaks located at 711.03 eV and 714.40 eV, respectively. This result corroborates the co-existence of both valence states of iron ions (Fe²⁺ and Fe³⁺), confirming the formation of Fe₃O₄ [82,83] which is in good agreement with the XRD results. The Fe³⁺/Fe²⁺ ratio was found to be 1.7:1, which is fairly close to the expected ratio of 2:1 for bulk magnetite. In Figure 4.15d is shown the core level XPS spectrum of Ni2p. The peak located at 852.45 eV suggests the existence of a metallic Ni³⁵ and the peak at 856 eV with a satellite peak at 861.78 eV has been assigned to Ni²⁺ [84]

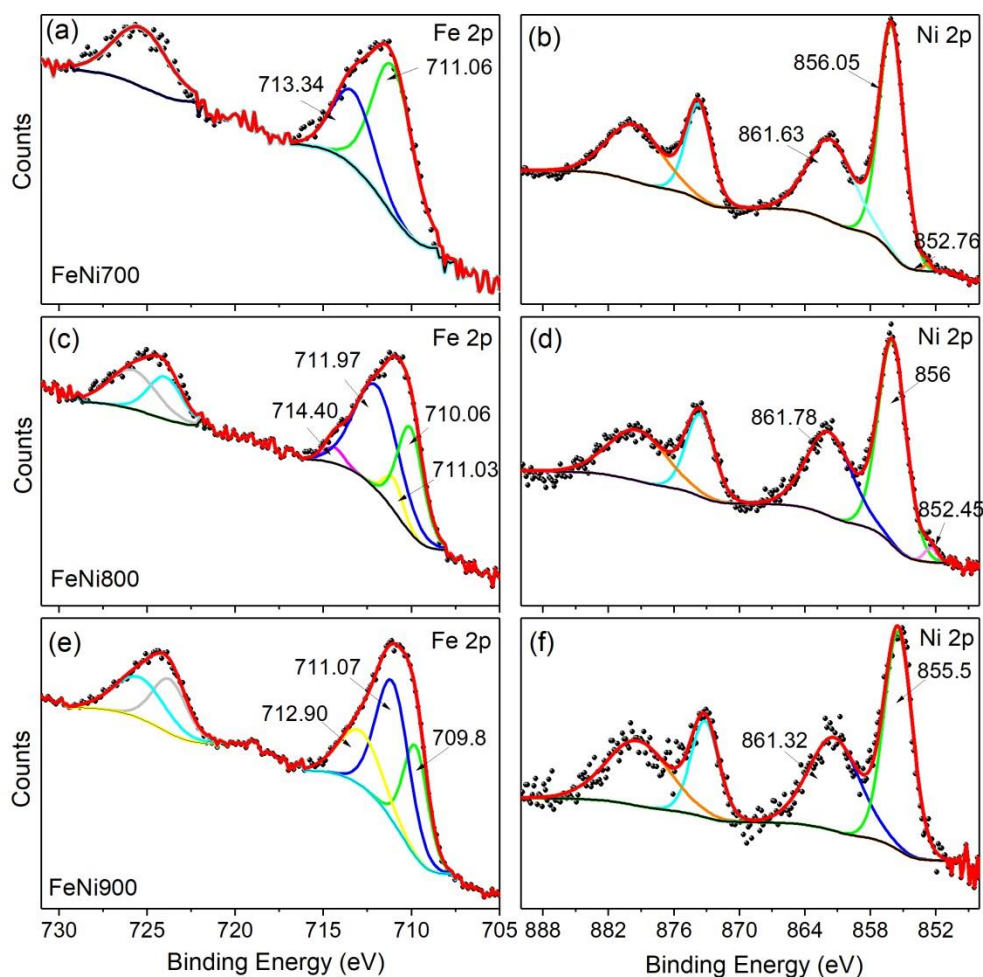


Figure 4.15 High-resolution XPS spectra of the samples FeNi700, FeNi800 and FeNi900. (a), (c) and (e) Fe 2p peaks respectively. (b), (d) and (f) Ni 2p peaks respectively.

The presence of metallic nickel and no metallic iron at the particles surface indicates the complete oxidation of metallic iron phase during the thermal annealing process, which is more active to oxidation than metallic Ni. For an annealing temperature greater than 800°C, similar results were found as in the sample FeNi800, but no metallic nickel atoms were detected in the core level XPS spectrum of Ni2p for the sample FeNi900 as shown in Figure 4.15e-f, which indicates the complete oxidation of nickel at that temperature. This oxide phase was not detected by SXRD measurements. Besides, in all samples showing the superstructure reflections, it was determined the presence of Fe^{+2} and Fe^{+3} ions, confirming the findings obtained via SXRD and HRTEM.

The differential scanning calorimetry (DSC) trace of a portion of the as-prepared sample is shown in Figure 4.16 with 3 thermal peaks. A first endothermic peak with an onset

temperature of $\sim 61.6^{\circ}\text{C}$ and a peak temperature of $\sim 112.5^{\circ}\text{C}$ is observed. According to FT-IR measurements, the presence of water and organic component residues were detected, which were evaporated during this annealing of the sample. Temperatures greater than 100°C measured for the evaporation of water are due to the mixture of this with the organic components and with particles of the sample.

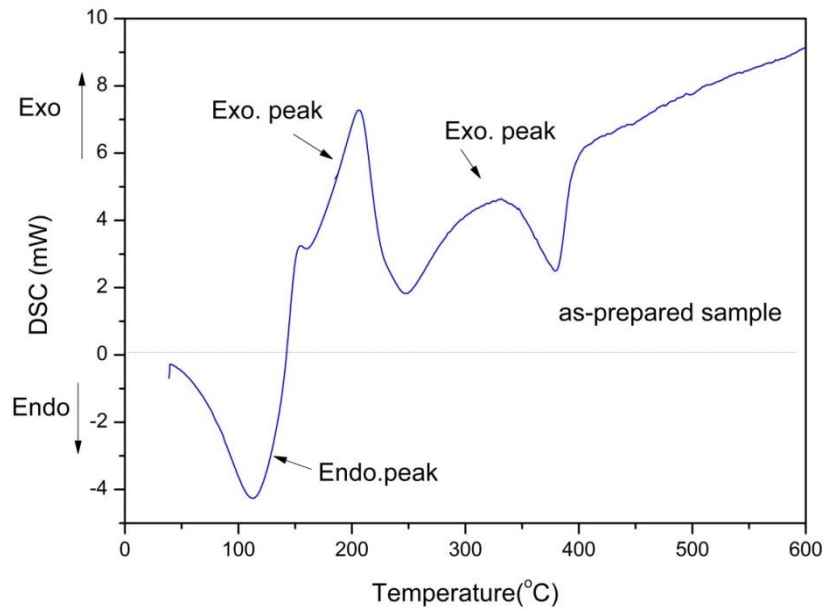


Figure 4.16 The DSC analysis of the as-prepared sample (amorphous sample) from 28°C to 600°C .

The beginning of the crystallization process of the as-prepared sample is represented by an exothermic peak with an onset temperature of $\sim 164.5^{\circ}\text{C}$ and a crystallization temperature of $\sim 205.3^{\circ}\text{C}$. A second exothermic peak is formed whose crystallization temperature is $\sim 331.5^{\circ}\text{C}$, at this temperature is precisely that the disordered FeNi phase is formed together with impure phases as shown in the X-ray diffractogram of the sample FeNi with annealing temperature at 300°C . From 380°C , the temperature increases linearly up to 600°C where the diffractogram of the sample at 600°C indicates the single phase formation of disordered FeNi. One might expect an exothermic peak to appear at 700°C due to the beginning of the formation of the ordered phase.

4.1.2 Hyperfine Properties

The Mossbauer spectroscopy measurements of the powder samples of the FeNi alloy were obtained at 300K. In Figure 4.17 is shown the spectra for sample FeNi400 and in Figure 4.18 for the samples from FeNi500 to FeNi1150. The analysis of the spectra using the Normos program revealed that best fit can be achieved using a superposition of the sub spectra depending on the sample and the obtained hyperfine parameters are listed in Table 4.3.

The spectrum of the sample FeNi400 is a superposition of the following four spectra: 3 sextets and a doublet (see details in Table 4.3). From the values of the hyperfine parameters, two sextet components are attributed to the Fe^{3+} and Fe^{2+} ions in octahedral B and Fe^{3+} ions in tetrahedral A sites of magnetite (Fe_3O_4). Due to the high value of the quadrupole splitting (Q.S.) of this doublet and the size distribution of the FeNi400 sample, which are mostly less than 7nm (see Table 4.2), this doublet may represent the superparamagnetic behavior of these nanoparticles.

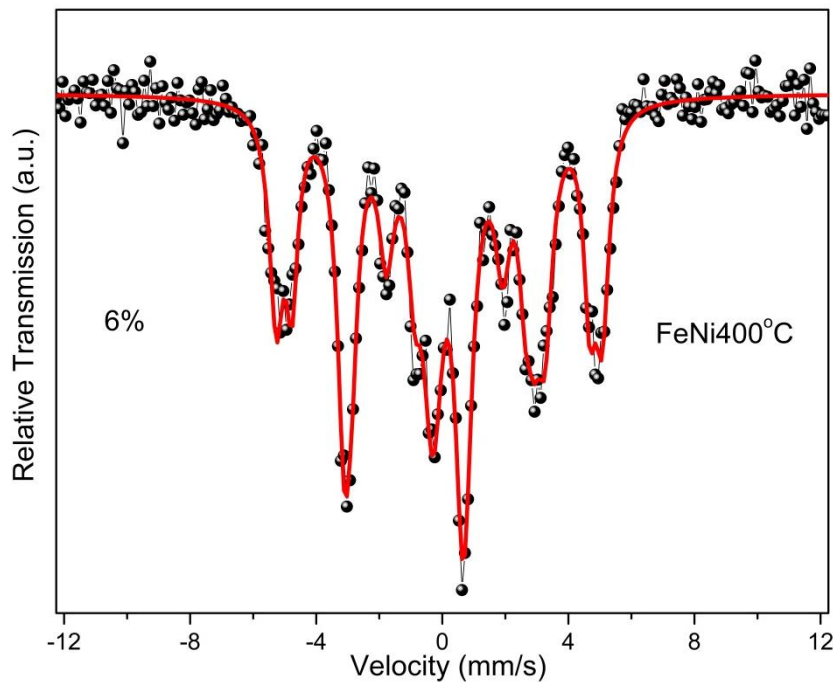


Figure 4.17 Mossbauer spectrum at room temperature of the sample FeNi400. The percentage on the left side indicates the radiation absorption.

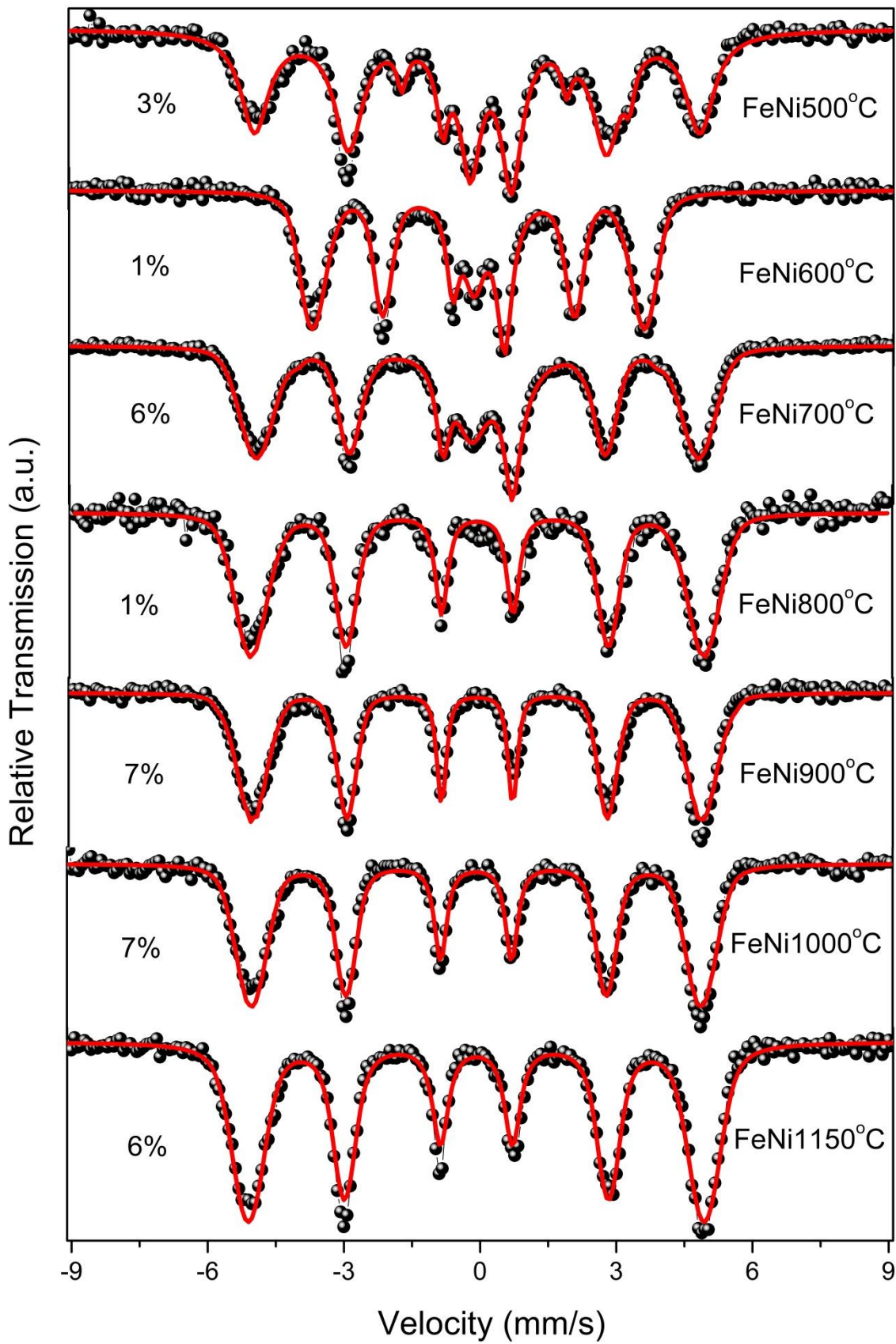


Figure 4.18 Mossbauer spectra at room temperature of the samples from FeNi500 to FeNi1150. The percentages on the left side indicate the absorption of the radiation.

Finally, a magnetic phase with null Q.S was assigned to the ferromagnetic disordered face-centered cubic (fcc) phase of FeNi [30].

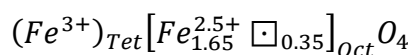
Table 4.3 Hyperfine parameters of the fitted spectra of the samples from FeNi400 to FeNi1150. W: linewidth at half height (± 0.02 mm/s); I.S: isomer shift relative to α -Fe (± 0.01 mm/s); Q.S: quadrupole splitting (± 0.01 mm/s); H: internal hyperfine magnetic field (± 0.3 T); A: relative spectra area ($\pm 4\%$). The asterisk indicates the value of the quadrupole split for the doublets.

SAMPLE	Fe-Ni phases	I.S (mm/s)	Q.S (mm/s)	H (T)	W (mm/s)	A (%)
FeNi400	DISORDERED	-0.09	0.00	32.1	0.53	28.8
	SEXTET	0.18	0.00	19.8	0.57	30.8
	(Fe ³⁺ +Fe ²⁺ in B-sites)					
	SEXTET (Fe ³⁺ in A-sites)	0.03	0.06	29.3	0.45	18.6
FeNi500	DISORDERED	0.22	-0.96*	-	0.70	21.8
	DOUBLET	-0.09	0.00	31.2	0.76	65.4
	DOUBLET	0.22	-0.92*	-	0.55	25.8
	DOUBLET	-1.32	0.92*	-	0.26	5.0
FeNi600	DOUBLET	2.63	-1.42*	-	0.26	3.8
	ORDERED	-0.07	0.20	25.8	0.43	13.5
	DISORDERED	-0.06	0.00	28.0	0.56	75.7
	Ni-poor γ -phase	-0.06	-	-	0.64	10.8
FeNi600 (77K)	ORDERED	0.03	0.20	31.6	0.43	16.4
	DISORDERED	0.04	0.00	34.3	0.83	80.3
	Ni-poor γ -phase	0.04	-	-	0.43	3.3
FeNi700	ORDERED	-0.08	0.13	29.3	0.51	33.1
	DISORDERED	-0.08	0.00	31.9	0.48	52.6
	Ni-poor γ -phase	-0.05	-	-	0.77	14.3
FeNi700 (77K)	ORDERED	0.07	0.13	32.3	0.60	37.4
	DISORDERED	0.90	0.00	34.8	0.63	58.3
	Ni-poor γ -phase	-0.02	-	-	0.49	4.3
FeNi800	ORDERED	-0.06	0.17	30.1	0.47	29.1
	DISORDERED	-0.08	0.00	32.3	0.51	70.9
FeNi900	ORDERED	-0.08	0.21	29.8	0.36	19.5
	DISORDERED	-0.07	0.00	32.0	0.55	80.5
FeNi1000	ORDERED	-0.09	0.16	29.7	0.38	31.5
	DISORDERED	-0.07	0.00	31.9	0.45	68.5
FeNi1150	ORDERED	-0.07	0.18	29.5	0.37	22.4
	DISORDERED	-0.08	0.00	31.8	0.53	77.6

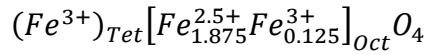
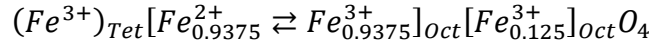
In nanoparticles is a fact that surface properties influences strongly in the magnetic properties and differ from the bulk ones. The two hyperfine magnetic field values referred to the sextets belonging to the A and B sites of magnetite detected in sample FeNi400 are lower than the known values for this oxide phase. These lower values could be due to iron ions in the surface region of the particle. As explained by Shipilin et al [85], the surface region of the spinel particle contains cations that are "depleted" with exchange bonds and considering the features of the exchange interaction of iron ions in the spinel structure, it is natural to assume that such "depletion" with exchange bonds should be shown in a decrease in the effective magnetic field values for ^{57}Fe nuclei. We also note a decrease in the isomer shift value of both sextets in comparison with the typical values for each site of magnetite. It could be due to the partial absence of neighboring ions surrounded of ^{57}Fe nuclei.

As it is well known, the area ratio of the Mossbauer lines in magnetite is a very perceptible measure of the stoichiometry of $\text{Fe}_{3-x}\text{O}_4$ [86,87]. If in the octahedral B-sites of stoichiometric magnetite, all Fe^{+2} and Fe^{+3} are participating in the electron exchange at a higher temperature than Verwey temperature, we will obtain $S_A/S_B = 0.5$. We had from the hyperfine data in Table 3 that the area ratio S_A/S_B is about 0.60 for the sample at 400°C .

As was explained by Lyubutin et al [88], this difference among both area ratio values could be understood either by the appearance of cation vacancies and/or by surface effects. In the case of cation vacancies \square in B-sites, the value $S_A/S_B=0.60$ would correspond to the nonstoichiometric magnetite with the chemical formula:



In the case of nanoparticles, we must consider surface effects and from hyperfine parameters, we have obtained the following formula:



In these cases, a possible oxygen nonstoichiometry was not considered.

For the sample FeNi500, its spectrum was fitted with 1 sextet and 3 doublets as components. This magnetic sextet with Q.S null represents the disordered face-centered cubic (fcc) phase of FeNi and the first doublet indicated in Table 3 corresponds to a superparamagnetic behavior, similarly to the sample FeNi400. While that for the two quadrupole doublets, a possible explanation could be that the component with smaller QS corresponds to internal iron sites, while the other is due to the ones on the surface of γ -Fe nanoparticles; the bigger QS of both components is explained with the higher distortion of the superficial iron sites.

For the samples from FeNi600 to FeNi1150, the fitting was well-developed with the overlap of:

- ✓ (a) a six line spectrum ascribed a ferromagnetic phase with a quadrupole shift (Q.S) arising from the non-cubic environment of the Fe atoms in this structure corresponding to the ordered L1₀-FeNi phase [3,30,31,89,90-93].
- ✓ (b) a magnetic phase without Q.S corresponding of the disordered face-centered cubic (fcc) phase of FeNi [30,89,91,92,94,95].
- ✓ Only in the case of the sample FeNi600 and FeNi700 was used a single central line corresponding to a lower absorption percentage. The line comes from a

paramagnetic γ -phase. This is a disordered iron-nickel alloy with less than 30% Ni [3,30,31,89-92,94].

It is important to note that f.c.c. iron-nickel alloys are paramagnetic at room temperature when the Ni concentration is below 30% [94]. Disordered f.c.c. iron-nickel alloys with more than 30% Ni are ferromagnetic with a hyperfine field varying with the Ni content from 0 to 29T [94,95]. The Mossbauer spectra of disordered f.c.c. iron-nickel alloys have very broad lines and show no quadrupole splitting [95]. The line broadening for the sextets can be attributed to hyperfine field distributions induced by different magnetic interactions between the intergrown domains of ordered $L1_0$ -FeNi phase and disordered fcc phase of FeNi.

The variations in the values of hyperfine magnetic field (H) and in Q.S can be ascribed to different degrees of order of the ordered $L1_0$ -FeNi phase. The higher the quadrupole shift and the lower the magnetic field (H) the higher the degree of order of the ordered FeNi phase. The variation of the degree of ordering in tetratenite is apparent in the Mossbauer spectra. In a systematic study done by Mossbauer spectroscopy in the tetrataenite of 23 iron meteorites, Albertsen et al. [96] observed that the hyperfine interactions exhibit a variation of $H = 285\text{kOe}$ to $H = 296\text{ kOe}$ and of $Q.S = 0.21\text{ mm/s}$ to $Q.S = 0.09\text{ mm/s}$. This dispersion corresponds to an increasing degree of disorder as has been shown in kinetics experiments of thermal disorder in the Cape York meteorite [97].

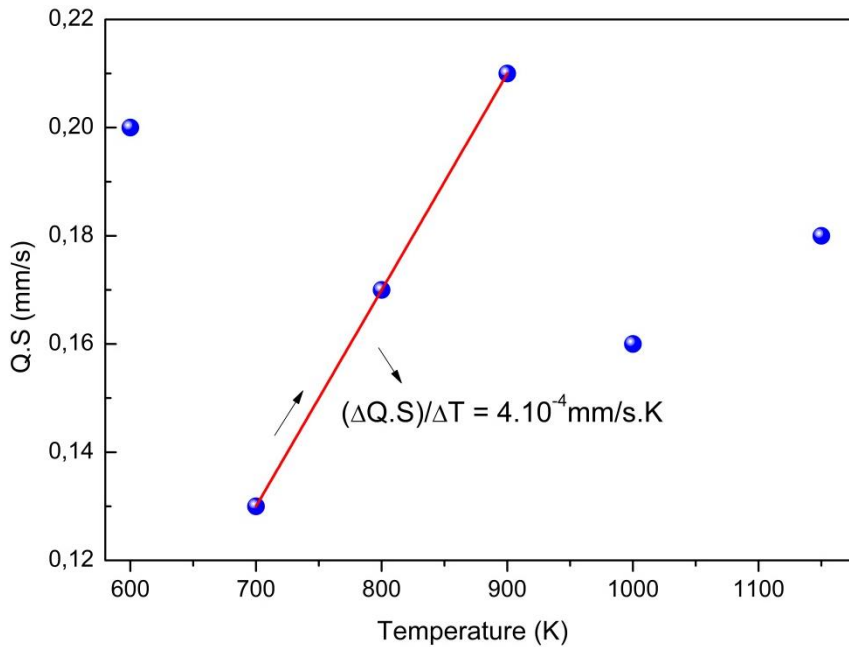


Figure 4.19 Graph of Q.S vs T, where the linear fit between the temperatures of 700°C and 900°C is shown. The rate of change between Q.S and T is indicated.

For our samples, this linear behavior between Q.S and H was not found. Linear behaviors were found for the graphs of Q.S and H versus the temperature (T) for certain ranges of T from 700°C to 900°C as shown in Figures 4.19 and 4.20. In these graphs as observed in the linear fittings, an increase in the value of T produces an increase in the value of the Q.S and a decrease in the value of H because an increase in the thermal agitation of the amorphous system (as-prepared sample) will provoke that the atomic disorder be increased and it will reach its energetic equilibrium state with a greater asymmetry around the iron atom and decreasing of the external magnetic field due to a weaker exchange interaction between the unpaired 3d-electrons of the neighboring atoms and the Mossbauer nucleus. As a consequence of this great asymmetry, the value of the order parameter S is reduced (see Table 4.2). A different behavior where an increase in the value of T produces a decrease in the value of the Q.S and H was observed experimentally by Albertsen et al [4] in the hyperfine parameters from Mossbauer spectra of a lamella from the iron meteorite Cape York. These parameters H

and Q.S were obtained at several temperatures in the temperature interval from 80 K to 732 K with values from 29.5 T and 0.21 mm/s to 23.8T and 0.14 mm/s respectively for each temperature.

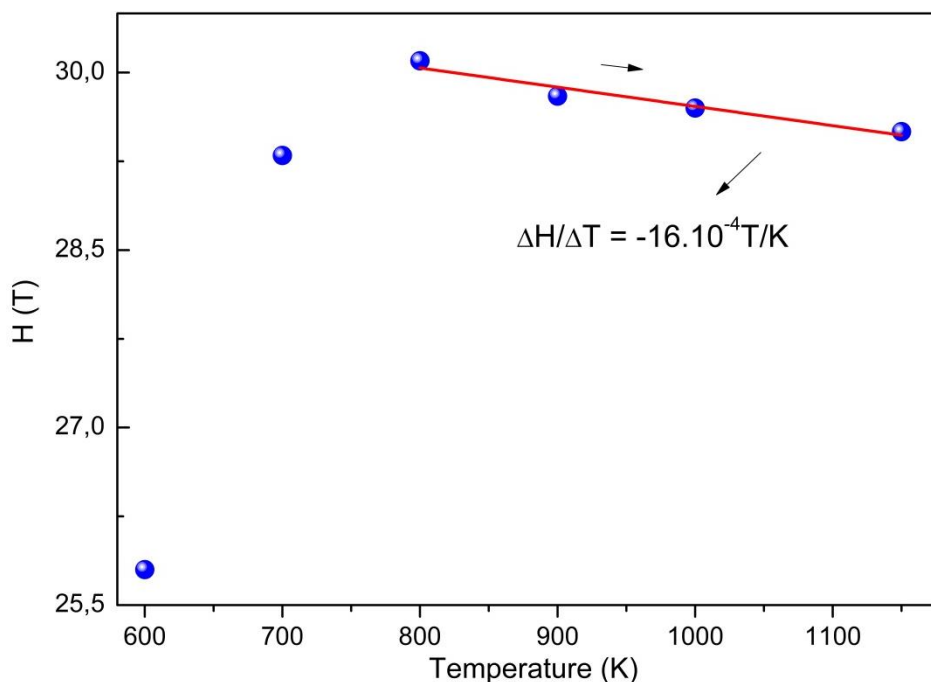


Figure 4.20 Graph of H vs T, where the linear fit between the temperatures of 800°C and 1150°C is shown. The rate of change between H and T is indicated.

The magnetic field at the nucleus is actually the vector sum of the externally applied field and the internal magnetic field. The internal magnetic field consists of the contribution basically of three components:

- The Fermi contact interaction, which is a direct coupling between the Mossbauer nucleus and its unpaired s-electron density.
- The orbital dipolar interaction, which is the interaction between the atomic orbital magnetic moment and the nuclear dipole moment.
- The spin dipolar interaction, which is the interaction of the spin moment of the electrons with the Mossbauer atomic nucleus.

This internal magnetic field is the same for all the Mossbauer atoms within the tetragonal crystalline structure of FeNi and therefore, this internal field was not taken into consideration when changing the annealing temperature.

The fact that our experimental hyperfine parameters Q.S and H do not maintain a linear behavior as reported by Albertsen et al. [96] can be due to obtaining the ordered phase at different annealing temperatures.

The disordered FeNi phase has been shown in the Mossbauer spectra of the treated samples from 800°C to 1150°C. The fit of the X-ray diffractograms with the disordered FeNi phase was not possible. This is because the diffractograms of the ordered and disordered phases of FeNi are hardly differentiated only by a superstructure peak of very weak intensity, so the percentage of each phase in this superposition will be uncertain.

The small amounts of iron oxides found in the samples through XRD and SXRD were detected by Mossbauer spectroscopy with spectral areas of less than 2%, since these sub-spectra escape the measurement resolution, it can be considered as part of the spectral noise.

The spectra of the samples FeNi600 and FeNi700 showed the presence of the ordered phase with spectral areas of 13.5% and 33.1% respectively. Measurements of SDRX for both samples did not show diffraction lines belonging to this ordered phase [74] possibly because of the atomic disorder is overlapping to the atomic order, preventing the clear appearance of the superstructure line (100) of this ordered phase.

For a better understanding about the paramagnetic singlet (see Table 4.3) shown in the Mossbauer spectra of the samples FeNi600 and FeNi700, the subspectra of these samples recorded at room temperature and 77K are shown in Figure 4.21 which were analyzed with similar subspectra obtained at room temperature.

The spectral areas of both samples undergo a drastic decrease to 77K when comparing the values at room temperature. The hyperfine parameters of both spectra at 77K are shown in Table 4.3. This drastic decrease can be explained by Rancourt et al. [96] where through only differences in its electronic structure, two minerals like disordered FeNi and FeNi with less than 30% in Ni (paramagnetic phase) can have the same

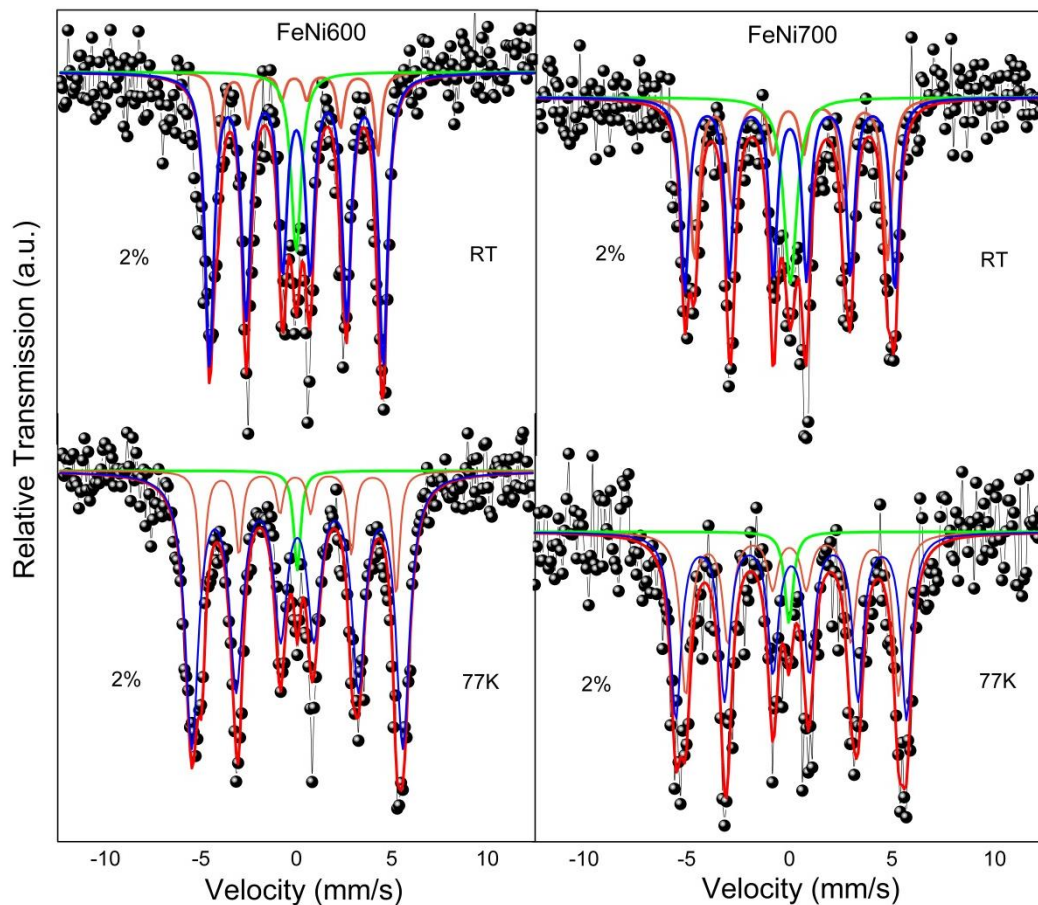


Figure 4.21 Mossbauer spectra of the samples FeNi600 and FeNi700 at room temperature and 77K. The number on the left side of each spectrum indicates the percentage of absorption.

crystalline structures and the same compositions under the consideration that this paramagnetic phase is a low moment phase. With this, when cooling the sample to 77K, this low momentum is increased by the decrease of nuclear thermal agitation and assuming that the sample is at temperatures lower than Curie temperature and maintaining the same crystalline structure that disordered FeNi, it will contribute now with the area spectral of this last phase.

The results obtained for the samples from Mossbauer spectroscopy clearly confirm the formation of this ordered phase and are in good agreement with the results obtained from SDRX, DRX and HRTEM. It is worth mentioning that only through this spectral technique, the presence of the disordered FeNi phase was detected. The spectral percentage of the ordered phase between samples FeNi600 to FeNi1000 varies between 13% and 37.5%.

4.1.3 Magnetic Properties

Figure 4.22 shows the hysteresis loops which are characteristic of ferromagnetic materials, formed in the graphs of the magnetization (M) as a function of the external magnetic field (H) obtained at temperatures of 380K and 5K for samples from FeNi600 to FeNi1000. The data extracted from these magnetic curves and the particle diameters are listed in Table 4.4. As mentioned in previous chapter, the permanent magnets or also called hard magnets are characterized by a high saturation magnetization, large coercive fields as well as a large uniaxial magneto-crystalline anisotropy.

Table 4.4 Magnetic data obtained from hysteresis loops, magneto-crystalline anisotropy constants and particle sizes of all samples.

Sample	Coercive Field (H _c) (units: Oe)		Saturation Magnetization (M _s) (units: emu/g)		Saturation Magnetization (M _s) (units: emu/cm ³)		Magneto-crystalline anisotropy constant (K) (units: J/m ³)	Size (nm) (±0.5)	Fe Concentration	Critical temperature (θ)
	5K	380K	5K	380K	5K	380K				
	FeNi 600	339.9	141.6	130.3	105.7	1072.4				
FeNi 700	415.1	171	124.3	100.2	1023	824.6	9x10 ⁴	7.0	0.98	792K
FeNi 800	116	52	169	135	1390.8	1111.1	9.1x10 ⁴	11.4	0.94	789K
FeNi 900	16.3	10.3	202.8	170.1	1669	1400	0.16x10 ⁶	11.8	0.96	719K
FeNi 1000	17	10.1	186.5	153.6	1534.9	1264.1	0.22x10 ⁶	12.4	0.90	701K
FeNi 1150	9.4	7.5	168.8	149	1389.1	1226.5	-	12.9	-	-

As it is well known in the literature, the values for the coercive field of the Tetraetaenite vary from 500 Oe to 3kOe. The results of the coercive field for the samples vary from 10.1 Oe to 171 Oe so we can apparently infer that through this magnetic characteristic, the samples could not be considered as hard magnets and that the hysteresis loops would represent characteristic curves of soft magnets. The coercive field depends on the demagnetizing field and the anisotropy field. The first contributes by decreasing the coercive field and to maintain the equilibrium; the field of anisotropy increases the coercive. For the FeNi samples from 600°C to 1000°C, the observed experimental behavior shows that the coercive field decreases with the increase of the magneto-crystalline anisotropy. This can be explained by considering nano-structured bulks where the shape anisotropy grows in the direction of the magneto-crystalline easy axis.

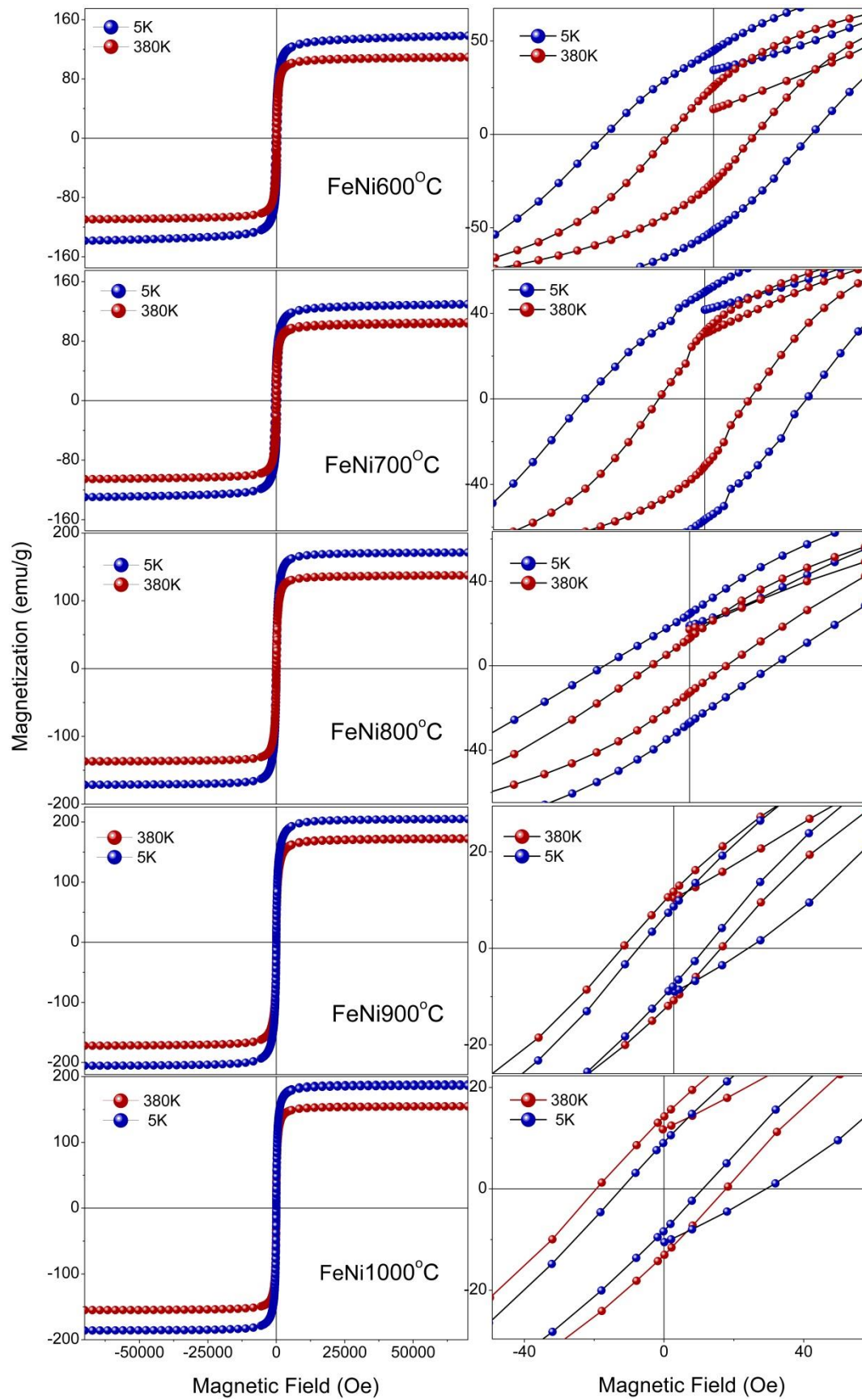


Figure 4.22 Magnetization vs. magnetic field (H) curves obtained at temperatures of 380K and 5K of the samples from FeNi600 to FeNi1000. Right side is the amplified image of coercive field for each curve.

This was demonstrated by Kovacs et al.[98] through computational calculations. Three nano-structured bulks with different shapes were chosen: equi-axed, platelet and columnar grain shapes of single grains. The average grain dimensions are 56nmx56nmx56nm,72nmx72nmx34nm, and 34nmx34nmx146nm for the equi-axed, platelet and columnar grain shape, respectively.The obtained result was that shape anisotropy increases the coercive field of the columnar model by 10% compared to the platelet model for $K = 1.3\text{MJm}^{-3}$ and by 170% for $K = 0.35\text{MJm}^{-3}$.

In Figure 4.23, the high resolution micrographs of the samples FeNi700 and FeNi1000 are observed. Here the change in the shape of the grains, of semi-spherical or elliptical surfaces to rectangular surfaces is clearly noted.

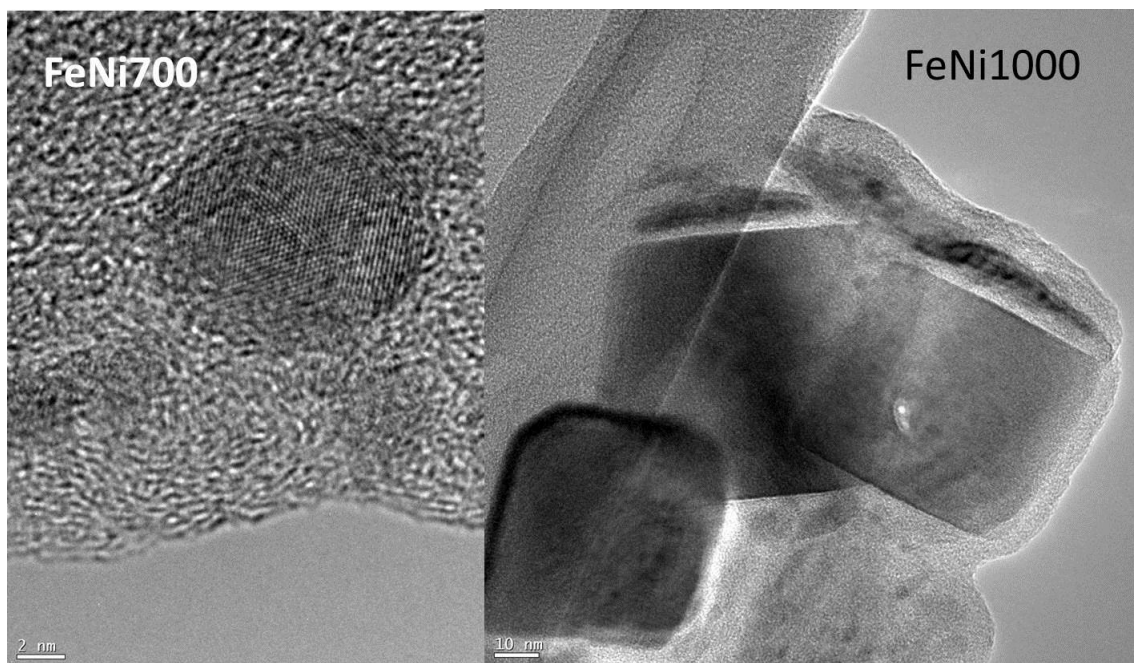


Figure 4.23 High resolution micrographs of the FeNi700 and FeNi1000 samples. The change in the shape of the grain is clearly noticeable.

If we analyze the values obtained for the saturation magnetization, the initial classification for the samples could be different. For the Tetraetaenite, a large value of 1200 emu/cm^3 was measured for the saturation magnetization. As indicated in Table 4.4, the magnetic saturation of the sample FeNi800 is very close to that of a hard

magnet, while FeNi900, FeNi1000 and FeNi1150 reached surprisingly higher values (~ 17%, ~ 5.4% and ~ 2.2%, respectively) than bulkTetrataenite. It should be noted that in the ordered samples of FeNi (FeNi700 to FeNi1150), it can be considered that the small concentration of magnetite present in the samples (less than 3%) determined from Mossbauer spectroscopy measurements may be negligible for magnetic considerations. This high magnetization of saturation could be due to the strong interaction between the magnetic domains produced possibly by the minimum magnetic energy necessary for the interaction between them through the domains walls.

Returning to discuss the values obtained from the coercive field for FeNi alloys, in Figures 4.24 and 4.25, the graphs of H_c vs D (diameter of particle) and of H_c vs T (annealing temperature) respectively are shown. In Figure 4.24, it is observed that H_c decreases with increasing grain size. This behavior would be typical of permanent magnets as explained by Bance et al [99].

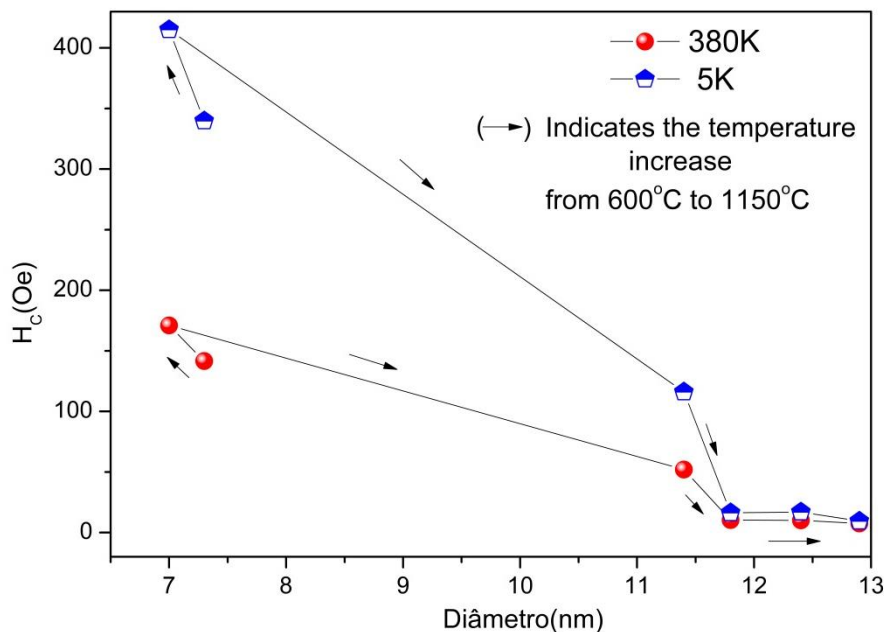


Figure 4.24 Graph of the behavior of the coercive field with the diameter of the particles at 380K and 5K.

Bance explains that the decay of coercive field (in logarithmic form) with increasing grain size results from the increase in the demagnetizing field near the edges of a grain. Here, the torque exerted by the local field onto the magnetization initiates the formation of a reversed domain.

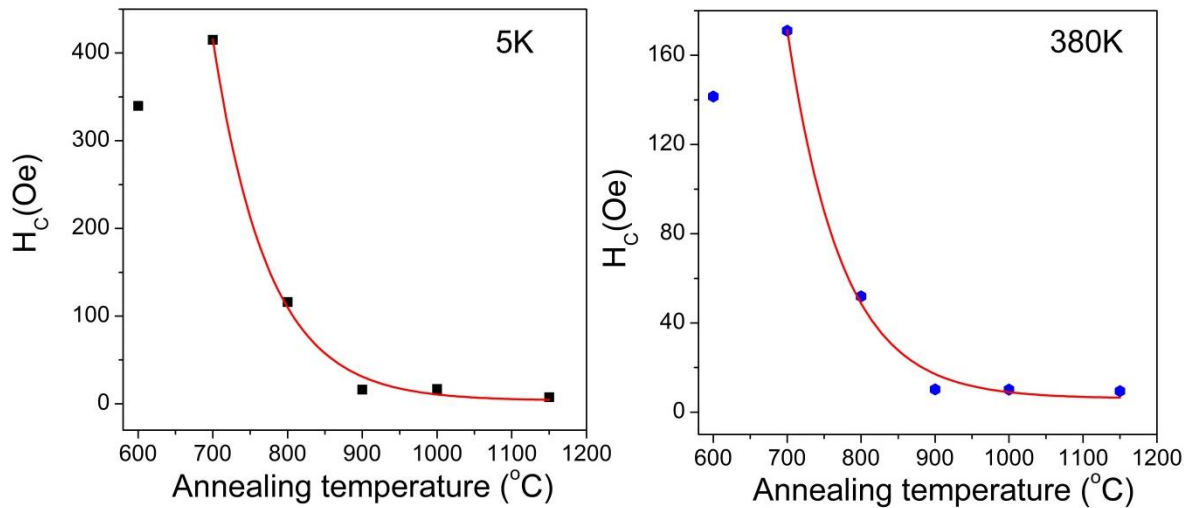


Figure 4.25 Logarithmic behavior of the coercive field with the annealing temperature at 5K and 380K.

With increasing particle size, the torque that rotates the magnetization out of the anisotropy direction becomes larger and domain formation happens at lower external fields. In the graph H_c vs T , a logarithmic decrease of the coercive field with the increase in the annealing temperature is observed. This behavior is clearly explained by understanding that with the increase in the annealing temperature, the particle size increases and it produces the decrease of the coercive field as has already been explained by Bance et al.

Magnetic measurements of the FeNi nanocrystals were conducted in both zero field cooling (ZFC) and field cooling (FC) and were analyzed. Figure 4.26 shows the low field (20 Oe) magnetization dependence with temperature (5K to 380K) in ZFC/FC modes. Maximum magnetization is detected in the ZFC process in all samples except in FeNi700. The blocking temperatures (T_B) of ordered $L1_0$ -FeNi nanoparticles for each

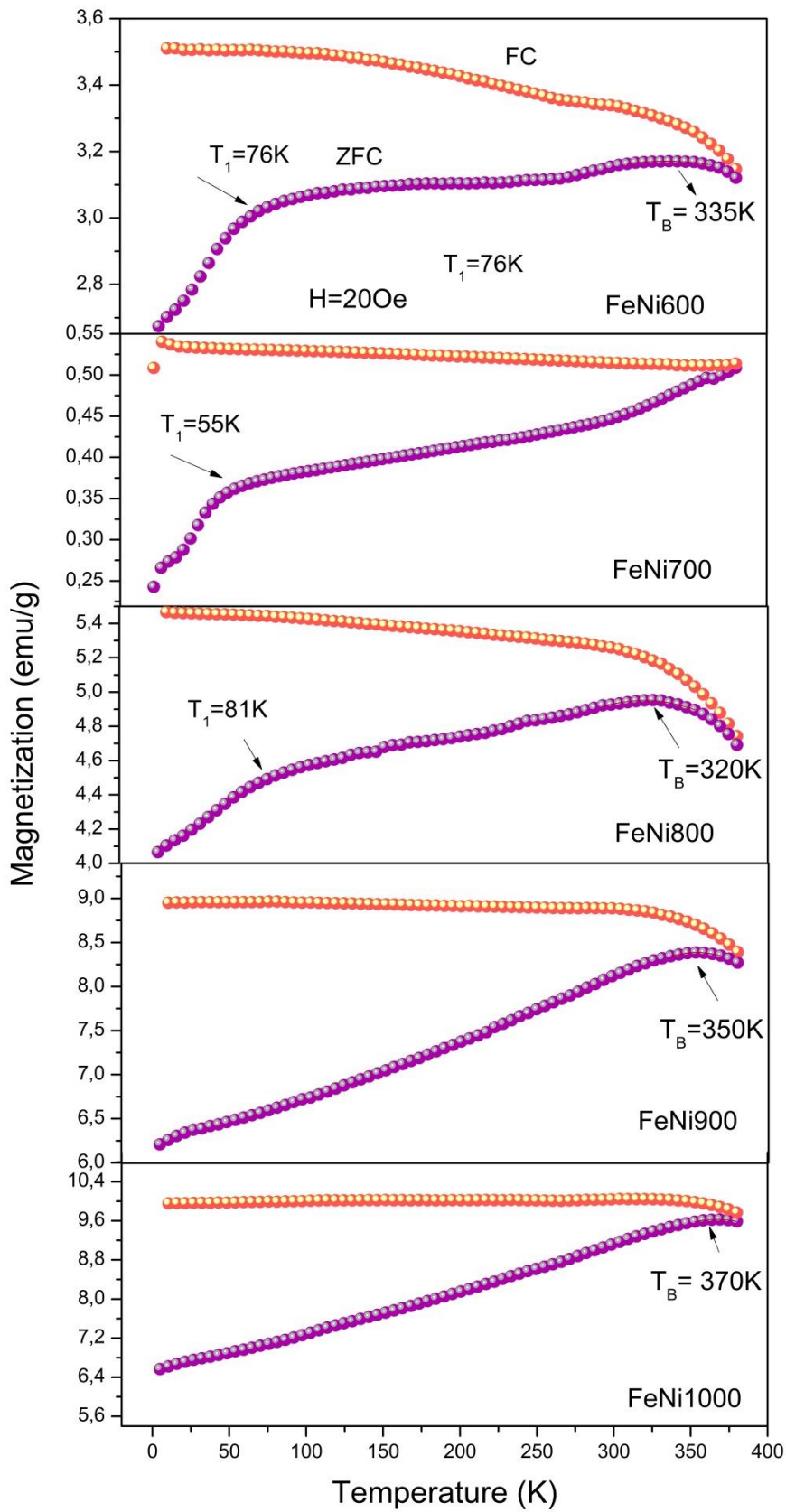


Figure 4.26 Magnetic characterization of the samples of FeNi using ZFC/FC curves under $H=20\text{ Oe}$, where T_B and T_1 is marked with an arrow.

sample are indicated in Figure 4.26. The blocking temperatures are greater than 320K, for the ordered samples from FeNi700 to FeNi1000 which means that the feature observed in hysteresis loops at 380K (and therefore at 300K below the blocking temperature) along with that in ZFC/FC curves is in good accordance with those expected for ferromagnetic particles.

.For sample FeNi700, after a ZFC process, the magnetization increases with rising temperature being that no maximum magnetization is detected in the ZFC process, indicating that the blocking temperature of these nanoparticles is above 380 K. Additionally, an irreversible magnetic behavior is indicated in all samples by the splitting between the ZFC and FC curves. The irreversibility arises from the competition between the energy required for magnetic moment reorientation against the energy barrier associated with magnetocrystalline anisotropy. The broadening of T_B peaks is attributed to the well-known influence of particle size distribution which is in good agreement with the polydispersion greater than 0.3 in all samples, as shown in Table 4.2.

Small knees appear in the ZFC curves at temperatures indicated by T_1 . Shafi et al. [100] found that magnetic susceptibility of $Fe_{40}Ni_{60}$ and $Fe_{60}Ni_{40}$ indicates blocking temperatures of 35 K with a particle size of about 6 nm. For the samples FeNi600, FeNi700 and FeNi800 were found T_1 values of 76K, 55K and 81K which could be related with their particle sizes of 7.3, 7.0 and 11.4nm (see Table 4.2) respectively. But in our case, the stoichiometry of these amorphous nanoparticles (obviously not detected by XRD) will have a higher concentration of Fe ($Fe_{60}Ni_{40}$) because it is the magnetic part that contributes more to the pseudo-ferromagnetic behavior in the blocking state [101] as demonstrated via first principles computational calculation [102]. The fact that

the values of T₁ are greater than 35K is then possibly due to the larger size of nanoparticles and higher Fe concentration.

It is important to note that the blocking temperature increases with the decrease of the chemical ordering parameter. This behavior suggests that the anisotropic energy barrier is increased by the structural defects of the crystal lattice.

The magnetization (M/M_S) versus temperature (T) graph for the samples FeNi700, FeNi800 and FeNi1000 is shown in Figure 4.27. As shown in this figure, it was only possible to adjust the curve of FeNi1000 with the Curie-Weiss law for temperatures higher than the Curie temperature (T_c).

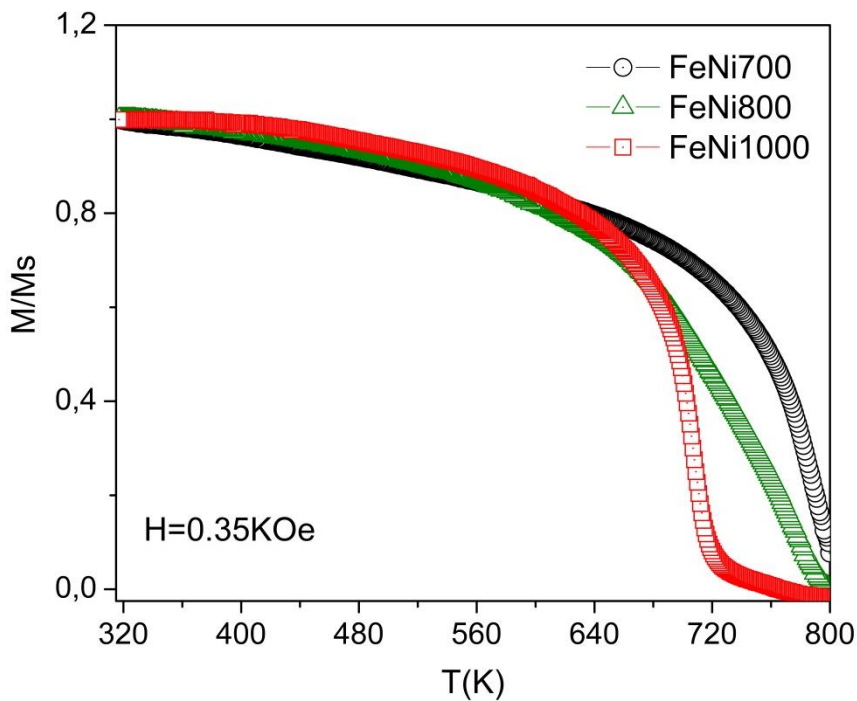


Figure 4.27 Behavior of the magnetization with the increase of the temperature under a magnetic field of 0.35K Oe.

The Curie-Weiss law is given by:

$$\chi = \chi_0 - \frac{C}{T - \theta}$$

where χ_0 represents the contributions with behavior independent of temperature, C is the Curie constant and θ is Curie temperature para o material .

Using this law to adjust the graph of magnetic susceptibility as a function of temperature in the paramagnetic region, well above the Curie temperature, which is where this law governs, we will find the experimental value of the Curie constant, unique to each compound, we can calculate the effective magnetic moment via the Curie-Weiss law. The graph of this fit, for the FeNi1000 sample, is shown in Figure 4.28.

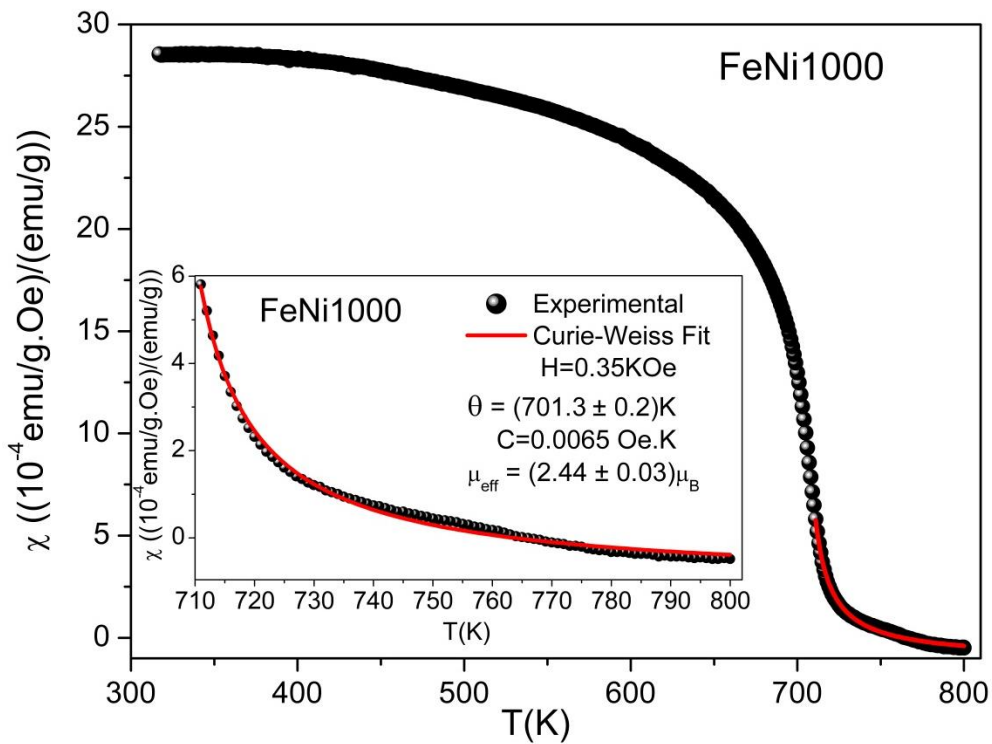


Figure 4.28 Graph of the magnetic susceptibility as a function of temperature for the sample FeNi1000. The solid line in red represents the adjustment made by the Curie-Weiss law. The inserted graph shows a zoom in the adjustment region.

By fitting the graph of χ vs T by the Curie-Weiss law, we find:

$\chi_0 = (-1.05 \pm 0.02) \times 10^{-4} \text{Oe}^{-1}$, $C = (65.5 \pm 1.54) 10^{-4} \text{K/Oe}$ and $T_c = (701.3 \pm 0.2) \text{K}$. Taking the values of the molecular weight (A) of FeNi and the Curie constant to the effective magnetic moment equation we have:

$$\mu_{eff} = 2.828\sqrt{CA} \mu_B = (2.44 \pm 0.03)\mu_B$$

As observed in Figure 4.27, the speed of decay of the magnetization increases with the annealing temperature and with the decrease of the chemical order parameter. The dependence of the Curie temperature (T_C) with the parameter of the chemical order is shown for example, via first principles calculations [102], where the ordered structure of FeNi has a Curie temperature of 1000K compared to the temperature of 800K for the disordered structure of FeNi. In the superstructure with ideal Fe and Ni estequeometry of 1: 1, the magnetic moment of Fe and Ni atoms maintain the high temperature of Curie but for being much greater the magnetic moment of the Fe atom, there is a strong magnetic interaction between Fe-Fe, responsible for this high temperature of Curie [103]. As shown by Lewis et al. [102], for each antisite occupied by either of the two atoms, the magnetic moment of the elementary crystalline structure decreases by $0.14\mu_B$. As shown in Figure 4.29, the occupation of Fe atoms (from the XRD information) increases with the annealing temperature decrease from 1000°C to 700°C.

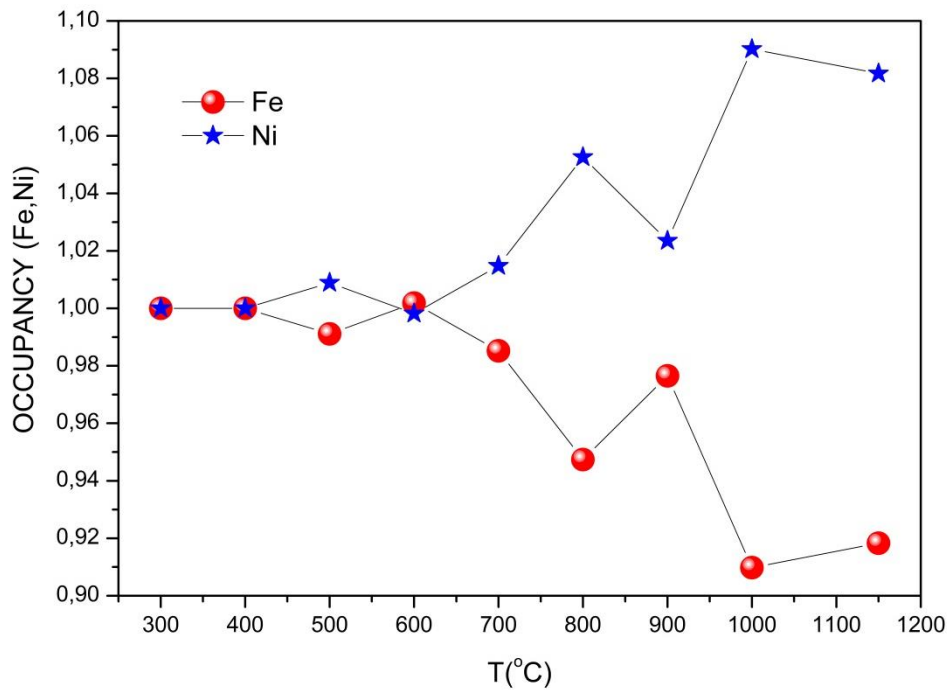


Figure 4.29 Occupancy of the Fe and Ni atoms formed in the crystalline structures between annealing temperatures from 300°C to 1150°C.

Because of this, the demagnetization rate is slower for the sample FeNi700 and the Curie temperature of this sample will be higher than the sample FeNi800 and the Curie temperatures of both will be greater than 701K (T_C of the sample FeNi1000).

As already mentioned, an $L1_0$ -type ordered FeNi alloy is an excellent candidate to be a rare-earth-free magnet due to its large saturation magnetization ($M_S = 1270 \text{ emu/cm}^3$) [8], high Curie temperature of around 550°C or higher [104,105] and for its large uniaxial magnetic anisotropy ($K=1.3 \times 10^6 \text{ J/m}^3$) [8,7].

To calculate the uniaxial magneto-crystalline anisotropy constant (K) for the FeNi600 to FeNi1000 samples, the law of approach to saturation for ferromagnetic materials was used (see eq 2.14). The values of the constants (M_s , b , p) and the value of K in J / m^3 for each sample are shown in Figure 4.30. As observed, the value of K increases with the annealing temperature and with the decrease of the chemical ordering.

All the obtained values are greater than the magneto-crystalline anisotropy for the disordered FeNi phase with a value of $2.5 \times 10^4 \text{ J/m}^3$ [106,107]. The anisotropy values for the samples FeNi900 and FeNi1000 are greater than the anisotropy values for single crystalline $L1_0$ -FeNi films [108-110] and very close to the values reported for the ordered $L1_0$ -FeNi phase.

These last two high values of anisotropy can be directly ascribed to the spin-orbit interaction. The Fe orbital moment shows strong angular dependence with a maximum value at the [001] direction corresponding to out-of-plane. The orbital anisotropy of Fe 3d electrons mainly results in the large magnetic anisotropy energy via spin-orbit coupling [60].

A possible explanation to understand the increase of the anisotropy with the decrease of the order parameter could be due to the fact that in this increase of crystalline disorder structural defects are produced causing the formation of new axes of easy magnetization.

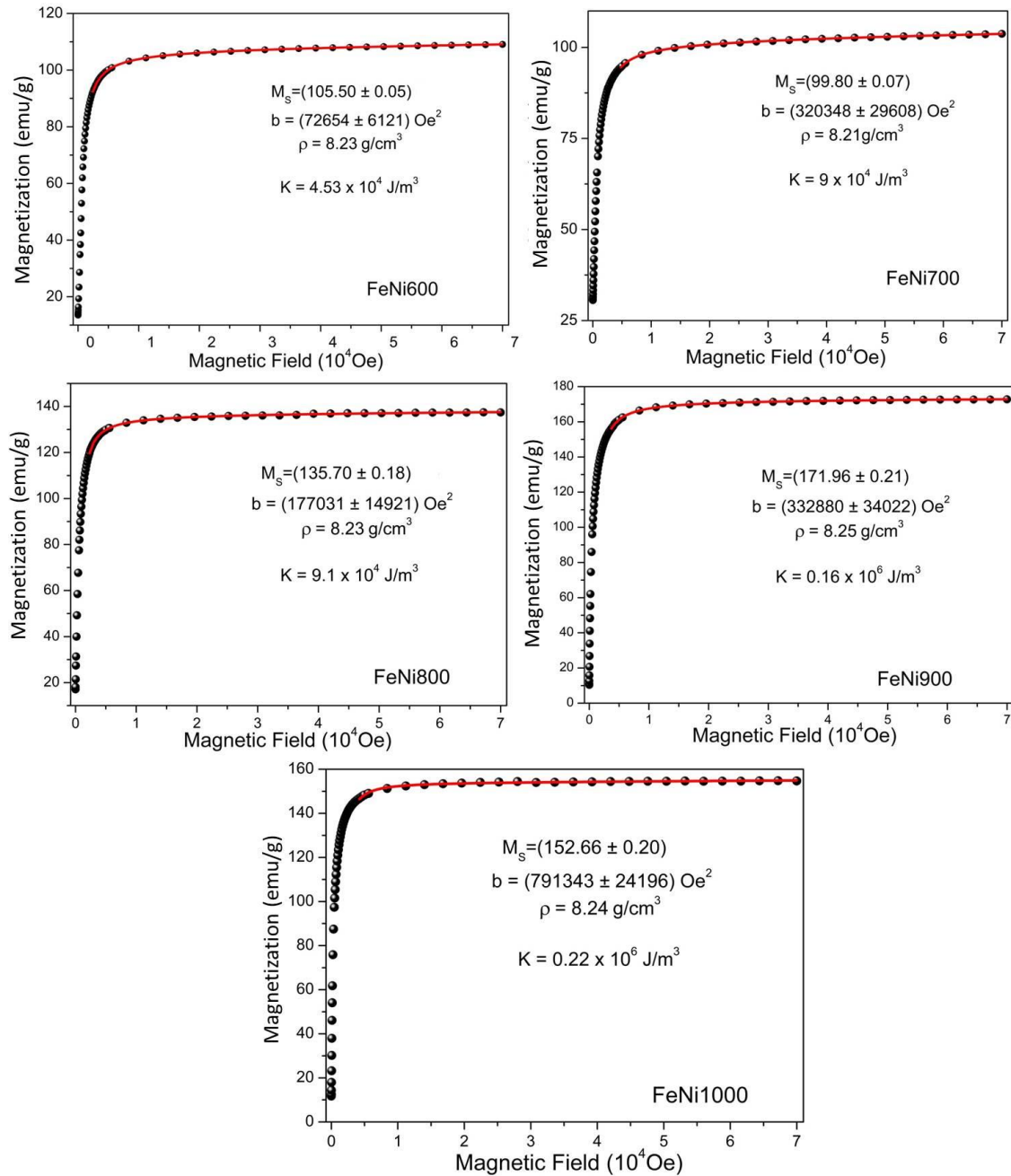


Figure 4.30 Graph of the magnetic moment as a function of magnetic field for the samples from FeNi600 to FeNi1000. The solid line in red represents the adjustment made by the law of approach to saturation.

Conclusions

SXRD measurements clearly confirm formation of the ordered L1₀- FeNi phase by the clear presence of the superstructure peak (100) in three samples analyzed by this technique. By HRTEM, the existence of the magnetite phase and the ordered phase were demonstrated. This showed the real existence of the presence of the ordered phase of FeNi in the samples. These results are confirmed by EDS and XRF measurements that showed the chemical stability of the ordered phase in the samples. The metastability of the ordered phase is discarded by these results that guarantee the formation of the ordered phase in the samples treated from 700°C to 1000°C. Outside this temperature range, the ordered phase was not detected, so there is a thermal dependence between this temperature interval and the formation of the ordered phase.

The chemical ordering parameter (*S*) decreases with the annealing temperature. The values of 0.81, 0.52 and 0.50 were calculated for *S* belonging to the samples annealed at 800°C, 900°C and 1000°C. This suggests that the crystalline system reaches a higher order (equilibrium) when the system approaches to this equilibrium with less entropy of formation that is at a lower temperature, in this case was of 800°C.

Moreover, the results obtained for the samples from Mossbauer spectroscopy clearly confirm the formation of this ordered phase and are in good agreement with the results obtained from SDRX, DRX and HRTEM. It is worth mentioning that only through this spectral technique, the presence of the disordered FeNi phase was detected. The spectral percentage of the ordered phase between samples FeNi600 to FeNi1000 varies between 13% and 37.5%.

Meanwhile, the magnetic measurements showed all the necessary characteristics of an ordered alloy of FeNi such as high magneto-crystalline anisotropy ($\sim 0.22 \times 10^6$ J /m³),

high saturation magnetization ($\sim 1264 \text{ emu/cm}^3$) and a high Curie temperature ($\sim 701\text{K}$). The strong Fe-Fe interactions of agglomerated particles are necessary to maintain the Curie temperature as well as a weak Fe-Fe interaction of separated particles to observe at blocking temperature. The coercive field is decreased by the shape anisotropy in the direction of the axis of easy magnetization.

Future works

- ✓ Determine the order and disorder temperature of each of the samples and observe if they change with the heat treatment temperature.
- ✓ To deposit the elements of Fe and Ni in films with the objective to increase the coercive field of intermetallic alloys.
- ✓ Samples treated from 1050°C will be synthesized to study the behavior of the ordered phase up to the treatment temperature of its possible destruction.

References

- [1] B. Manson, in: *Meteorites*, (John Wiley and Sons, Inc., New York and London, 1962)
- [2] R.S. Clark, Jr. and E.R.D. Scott, *Am. Miner.* **65**, 624 (1980)
- [3] J.F. Albersen, J. M. Knudsen and G. B. Jensen, *Nature* **273**, 453 (1978)
- [4] J.F. Albersen, M. Ayden, J. M. Knudsen, *Phys. Scripta* **17**, 46767 (1978)
- [5] J.F. Albersen, G. B. Jensen, , J. M. Knudsen, J. Danon, *Meteoritics* **13**, 379 (1978)
- [6] J.F. Albersen, *Physica Scripta* **23**, 301 (1981)
- [7] L. Néel, J. Pauleve, R. Pauthenet, J. Laugier, D. J. Dautreppe, *Journal of Applied Physics* **35**, 873 (1964)
- [8] J. Pauleve, A. Chamberod, K. Krebs, A. Bourret, *Journal of Applied Physics* **39**, 989 (1968)
- [9] J. Ormerod, and S. Constantinides, *Journal of Applied Physics* **81**, 4816 (1997)
- [10] S. Chikazumi, *Handbook of Magnetic Materials* 1975 (Tokyo: Asakura-shoten)
- [11] P. Bruno, *Physical Review B* **39**, 865 (1989)
- [12] R. Ramchal, A. K. Schmid, M. Farle, H. Poppa, *Physical Review B* **69**, 214401 (2004)
- [13] C. Klein, R. Ramchal, A. K. Schmid, M. Farle, *Physical Review B.* **75**, 193405 (2007)
- [14] T. Horichi, M. Igarashi, F. Abe, T. Mohri, *Calphad* **26**, 591 (2002)
- [15] Shima T, Moriguchi T, Mitani S and Takanasi K, *Appl. Phys. Letter.* **80**, 288 (2002)
- [16] L. Li, *et al. Sci. Rep.* **6**, 36212 (2016)
- [17] K.H.J. Buschow, and W.A.J.J. Velge, *Permanent magnetic materials of rare earth-cobalt compounds.* 1999.
- [18] M.Kotsugi, *et al., Applied Physics Express* **3**, 13001 (2010)
- [19] D. Alloyeau, *et al., Nature Materials* **8**, 940 (2009).

- [20] R. B. Scorzelli, *Hyperfine Interactions* **110**, 143 (1997)
- [21] J. Palevé, D. Dautreppe, J. Laugier and L. Néel, *C.R. Acad. Sci.* **254**, 965 (1962)
- [22] T. Shima, *et al.*, *Magn, Magn, Mater.* **310**, 2213 (2007)
- [23] R. B. Scorzelli, *Hyperfine Interactions* **110**, 143 (1997)
- [24] S. Lee, *et al.*, *Phil. Mag. Lett.* **94**, 639 (2014)
- [25] M. Mizuguchi, *et al.*, *Journal of the Magnetism Society of Japan* **35**, 4 (2011)
- [26] T. Kojima, *et al.*, *Japanese Journal of Applied Physics* **51**, 010204 (2012).
- [27] A. Makino, *et al.*, *Sci. Rep.* **5**, 12 (2015)
- [28] Goto, S. *et al.*, *Sci. Rep.* **7**, 13216 (2017)
- [29] B. D. Cullity, *Elements of X-ray Diffraction*, Addison-Wesley Publishing Company, Inc. (1956)
- [30] R.B. Scorzelli, I. Souza Azevedo and M. Funaki. *Hyperfine Interactions* **91**, 535 (1994).
- [31] J. Danon, *et al.*, *Nature* **281**, 469 (1979)
- [32] K. Yanai, *Catalog of Yamato Meteorites* (NIPR, Tokyo, 1979)
- [33] Marchand, A. and Chamberod, A. C.r., *hebd.Séanc.Acad.Sci., Paris* **261**, 8113 (1965)
- [34] Leslie, W. C., Stevens, D. W., and Cohen, M. in *High Strength Materials* (ed. Zackay, V. F.) Ch.12 (Wiley, New York, 1965).
- [35] Gütlich, P. 1975. *Mössbauer spectroscopy in chemistry*. (U. Gonser, ed.). Chapter 2. Springer-Verlag, New York
- [36] Walker, L. R., Wertheim, G. K., and Jaccarino, V. *Phys. Rev. Lett.* **6**, 98 (1961)
- [37] Akai, H., *et al.*, *Phys. Rev. Lett.* **56**, 2407 (1986)

- [38] Watson, R. E. and Freeman, A. J. Hartree-Fock theory of electric and magnetic hyperfine interactions in atoms and magnetic compounds. In *Hyperfine Interactions*. (A. J. Freeman and R. B. Frankel, eds.) Chapter 2. Academic Press, New York. 1967.
- [39] M Vazquez, W. Femengel, H. Kronmüller, *Phys. Stat. Sol. (a)* **15**, 547 (1989)
- [40] Kronmüller H and Grimm H, *J. Magn. Magn. Mater.* **6**, 57 (1977)
- [41] Neuweiler A, Hofmann B and Kronmüller H.J. *Magn. Magn. Mater.* **153**, 28 (1996)
- [42] N.S. Akulov, *Z. Physik* **69**, 822 (1931)
- [43] R.M. Bozorth, *Ferromagnetism*, Van Nostrand, New York, 1951
- [44] J.A. Wood, in: *Meteorites and the Origin of Planets* (McGraw-Hill, Inc., New York, 1968).
- [45] R. Gooley, R.B. Merrill and J.R. Smith, *Meteoritics* **10**, 410 (1975)
- [46] J. Paulev, *et al.*, *C.R. Acad. Sci. Paris* **254** (1962) 965; *J. Phys. Radium* **23**, 841 (1962)
- [47] Buckwald V F 1975 *Handbook of Iron Meteorites* (Berkeley, CA: University of California) p 1209
- [48] Funaki M, *et al.*, *Antarc. Meteorite Res.* **13**, 78 (2000)
- [49] Uehara M, *et al.*, *Earth Planet. Sci. Lett.* **306**, 241 (2011)
- [50] Reisener R J and Goldstein J I., *Meteorit. Planet. Sci.* **38**, 1679 (2003)
- [51] L. Néel, *et al.*, *J. Appl. Phys.* **35**, 873 (1974)
- [52] J. Danon, *et al.*, *J. Phys*, **41**, 363 (1980)
- [53] Nagata T and Funaki M. *Mem. Natl. Inst. Polar. Res.*, Spec. Issue **46**, 245 (1987)
- [54] Mizuguchi M, Sekiya S and Takanashi K, *J. Appl. Phys.* **107**, 09A716 (2010)

- [55] Kojima T, Mizuguchi M and Takanashi K, *J. Phys.: Conf. Ser.* **266**, 012119 (2011)
- [56] Kotsugi M et al., *Appl. Phys. Express* **3**, 013001 (2010)
- [57] Kotsugi M, et al., *J. Phys.: Conf. Ser.* **266**, 012095 (2011)
- [58] Kotsugi M, et al., *IBM J. Res. Dev.* **55**, 13 (2011)
- [59] Kotsugi M, et al., *Surf. Sci.* **601**, 4764 (2007)
- [60] Kotsugi M, et al., *J. Magn. Magn. Mater.* **326**,235 (2013)
- [61] Mitsumata C, et al., *J. Magn. Soc. Japan* **35**,52 (2011)
- [62] Miura Y, et al., *J. Phys.: Condens. Matter* **25**,106005 (2013)
- [63] L. León, et al., *Hyperfine Interac.* **202**,131 (2011)
- [64] Jenkins, R., Snyder, R. L. *Introduction to X-ray Powder Diffractometry*. Eds. Wiley: New York, 1996.
- [65] L. León, et al., *Hyperfine Interac.* **202**, 131 (2011)
- [66] Yang, C., Williams D. & Goldstein, J. *Geochim. Cosmochim. Acta* **61**, 2943 (1997).
- [67] Tas, A. C., Majewski, P. J. & Aldinger, F. *J. Am. Ceram. Soc.* **85**, 1421 (2002).
- [68] Li, G, et al. *Inorg. Chem.* **49**, 1449 (2010).
- [69] Zhao, Y., et al., *J. Phys. Chem. C* **112**, 3568 (2008).
- [70]. Wengong, Z. & Zhaoguo, J. *Sci. China Ser. B Chem.* **47**, 159 (2004).
- [71] Zorkipli, N., et al., *Procedia Chem.* **19**, 626 (2016).
- [72] Bagheri, S., Chandrappa K. G. & Hamid, A. B. A. *Res. J. Chem. Sci.* **3**, 62 (2013).
- [73] Teoh, L. G. & Li, K. D. *Mater. Trans.* **53**, 2135 (2012).
- [74] Lima, Jr. E. & Drago, V. *Phys. Stat. Sol. (a)* **187**, 119 (2001)
- [75] Zhang, J. et al., *Meteoritics* **25**, 167 (1990).
- [76] Kotsugi, M. et al. *J. Phys.: Condens. Matter* **26**, 064206 (2014).
- [77] Sturges, H. *J. Am. Stat. Assoc.* **21**, 65 (1926).
- [78] Kim, H. S. et al., *Met. Mater.* **2**, 15 (1996).

- [79] Lizbet, L. F. *et al. Sci. Rep.* **7**, 41732 (2017).
- [80] Reuter, K. B. *et al. Metall. Trans. A* **17**, 163 (1986).
- [81] Reuter, K. B. *et al. Metall. Trans. A* **20**, 711 (1989).
- [82] Li, G., Li, R. & Zhou, W., *Nano-Micro Lett.* **9**, 46 (2017).
- [83] Fu, C., Mahadevegowda, A. & Grant, P. S. *J. Mater. Chem. A* **3**, 14245 (2015).
- [84] Ma, T. *et al. J. Alloys Compd.* **678**, 468 (2016).
- [85] Shipilin, I.N. Zakharova, A.M. Shipilin, V.I. *Journal of Surface Investigation.* **8**, 3 (2014)
- [86] J. M. Daniels and A. Rosenswaig, *J. Phys. Chem. Solids* **30**, 1561 (1969)
- [87] F. C. Voogt. *et al. Phys. Rev. B* **60**, 11193 (1999)
- [88] I. S. Lyubutin, *et al. Journal of Applied Physics* **106**, 034311 (2009)
- [89] R.B. Scorzelli, *Hyperfine Interactions* **66**, 249 (1991)
- [90] J. Danon, *et al. Nature* **277**, (1978) 283.
- [91] J.F. Petersen, *et al. Physics Letters* **62^a**, 192 (1977)
- [92] D. G. Rancourt. *et al. Journal of Magnetism and Magnetic Materials* **191**, 255 (1999)
- [93] J.F. Albertsen. *Psica Scripta* **27**, 314 (1983)
- [94] Johnson, C. E. *et al. Proc. Phys. Soc.* **81**, 1079 (1963).
- [95] Tino, Y. and Arai, J., *J. Phys. Soc. Jpn.* **32**, 941 (1972).
- [96] J.F. Albertsen, N.O. Roy-Poulsen and L. Vistisen, *Meteoritics* **15**, 258 (1980)
- [97] J.F. Albertsen, *Thesis (Ph.D)*, H.C. Oersted Institute, University of Copenhagen.
- [98] Alexander Kovacs *et al.*, *IEEE Transactions on Magnetics* **53**, 11 (2017)
- [99] S. Bance, *et al. Journal of Applied Physics* **116**, 233903 (2014)
- [100] K. V. P. M. Shafi, *et al. J. Appl. Phys.* **81**, 10 (1997)
- [101] Brian D Plouffe, *et al. Rep. Prog. Phys.* **78**, 016601 (2015)
- [102] L H Lewis. *et al. Journal of Physics: Condensed Matter*, **26**, 6 (2014)

- [103] M. Yu. Lavrentiev. *et al. Phys.Chem.Chem.Phys.*, **16**, 16049 (2014)
- [104] Wasilewski P., *Phys. Earth Planet. Inter.* **52**, 150 (1988)
- [105] L H Lewis. *et al. IEEE Magn. Lett.* **5**, 5500104 (2014)
- [106] S. Chikazumi, *Handbook of Magnetic Materials* 1975 (Tokyo: Asakura-shoten)
- [107] S. Chikazumi, *Physics of Ferromagnetism*, vol. II, Shyokabo, Tokyo, 1984. p.21
- [108] T. Shima.*et al. Journal of Magnetism and Magnetic Materials* **310**, 2213 (2007)
- [109] Takayuki Kojima *et al. Japanese Journal of Applied Physics* **51**, 010204 (2012)
- [110] T. Kojima, M. Mizuguchi and K. Takanashi. *J. Phys. Conf. Ser.* **266**, 012119 (2011).